

AD-A259 368



2

An Airborne Millimeter-Wave FM-CW Radar for Thickness Profiling of Freshwater Ice

Norbert E. Yankielun

November 1992

DTIC
SELECTE
JAN 19 1993
S B D



DISTRIBUTION STATEMENT A
Approved for public release;
Distribution Unlimited

93-00916



97px

93 1 15 006

Abstract

The ability to profile rapidly and accurately the structure of freshwater ice down to a thickness of a few centimeters over large surfaces of frozen ponds, lakes and rivers has wide military, industrial, commercial and recreational application, including safety and trafficability surveys. A prototype broadband millimeter wave (26.5 to 40 GHz) Frequency Modulated-Continuous Wave (FM-CW) radar, employing real-time data acquisition and Digital Signal Processing (DSP) techniques, has been developed for continuously recording the thickness profile of freshwater ice. Thickness resolution is better than 3 cm \pm 10%, which improves on short-pulse and FM-CW radars operating at frequencies less than 10 GHz. These other radars have a best reported thickness resolution of approximately 10 cm with a \pm 10% accuracy; this is insufficient because a freshwater ice sheet as thin as 5 cm, floating on water, can be safely traversed by an individual of average weight. System specifications include a 15-dBm output RF (Radio Frequency) power level, a 0.066-second sweep rate and less than a 50-dB Signal-to-Noise Ratio (SNR). This radar was tested on the ground and from a helicopter at heights of up to 7 m above ice surfaces at speeds up to 40 km/hr. Pond and river ice sheets between 3 and 35 cm thick, with and without fresh snow cover, and with minimal surface roughness have been profiled. Results have shown direct correlation between radar and borehole thickness measurements. Losses from volume scattering by imbedded air bubbles did not significantly affect the system's capability to discern the air/ice and ice/water scattering boundaries.

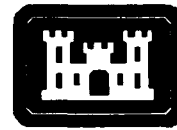
QUALITY INSPECTED 8

Accession For	
NTIS GRA&I	<input checked="" type="checkbox"/>
DTIC TAB	<input type="checkbox"/>
Unannounced	<input type="checkbox"/>
Justification	
By	
Distribution/	
Availability Codes	
Dist	Avail and/or Special
A-1	

Cover: Bell Ranger helicopter with prototype radar attached.

For conversion of SI metric units to U.S./British customary units of measurement consult ASTM Standard E380, *Metric Practice Guide*, published by the American Society for Testing and Materials, 1916 Race St., Philadelphia, Pa. 19103.

CRREL Report 92-20



**U.S. Army Corps
of Engineers**
Cold Regions Research &
Engineering Laboratory

An Airborne Millimeter-Wave FM-CW Radar for Thickness Profiling of Freshwater Ice

Norbert E. Yankielun

November 1992

PREFACE

This report was prepared by Dr. Norbert E. Yankielun, Thayer School of Engineering, Dartmouth College, Hanover, New Hampshire. The work, originally done as a Doctor of Engineering thesis, was performed with support from the U.S. Army Cold Regions Research and Engineering Laboratory. The U.S. Army Research Office (ARO) funded construction of a working model of the radar after the research was completed by providing a grant (DAAL03-91-G-0192). Technical and economic details of this implementation are given in Appendix A.

The author offers much thanks and gratitude to the following people, without whom this project would not have been a success: Dr. Steven Arcone of CRREL for his continued commitment, patience, encouragement and shared expertise; Professor Robert Crane for his guidance, assistance with the ARO grant, and tutelage on spectral analysis and radar; Professor Stuart Trembly for his guidance and insights; Professor John Walsh for his critical comments and enthusiasm; Alan Delaney of CRREL for his assistance with numerous technical and equipment-related issues, field testing and ground truth collection; Nancy Perron of CRREL for her coldroom assistance with the thin sectioning and micro- and polarized-light photography of ice core samples; and the author's family and dear friends for their generous love, understanding, encouragement and support throughout the frustrations and triumphs of this endeavor.

The contents of this report are not to be used for advertising or promotional purposes. Citation of brand names does not constitute an official endorsement or approval of the use of such commercial products.

CONTENTS

	Page
Preface	ii
Nomenclature	vii
Introduction	1
Problem statement	1
Previous work	1
Objective	2
Procedures	2
Electromagnetic propagation in ice	3
Radar range equation	3
Electromagnetic velocity	3
Dielectric permittivity of ice, water and snow	3
Transmission and reflection processes	6
Attenuation losses	7
Geometric spreading losses	7
Refraction and focusing effect	7
External random noise	9
Radar technologies	9
Impulse radar	9
Synthetic pulse radar	10
Coded radar	11
FM-CW radar	12
Selected technology	13
Specifications	13
Range and resolution	14
Signal-to-noise ratio	18
Data acquisition and recording	22
Antenna parameters	25
Physical parameters	28
Summary of specifications	28
Design and construction	29
Prototype system configuration	29
Test platforms	35
Power requirements	37
Economic considerations	37
Results	38
Skating arena profile	38
Stationary profiling of thin pond ice	39
Cart-mounted profiling of overflow pond	39
Cart-mounted profiling of Post Pond	40
Profiling of snow-covered pond ice	41
Truck-mounted profiling of pond ice	41
Cart-mounted profiling of Connecticut River ice	43
Airborne profiling of lake ice	44
Airborne profiling of river ice	45

	Page
Performance analysis	46
Theoretical measurement accuracy analysis	46
Radar pulse width analysis	50
Statistical analysis of radar pulse peak magnitude	57
System noise analysis	59
Conclusions and recommendations	59
Literature cited	60
Appendix A: Survey details	63

ILLUSTRATIONS

Figure	Page
1. ϵ_r and ϵ_i of freshwater ice as a function of frequency and temperature	4
2. ϵ_r and ϵ_i of fresh water as a function of frequency and temperature	4
3. Dielectric constant of freshwater ice with air bubbles	5
4. Measured ice thickness vs actual ice thickness	5
5. Reflection and transmission with two interfaces	6
6. Relative magnitudes of reflections from an air/ice/water multi-layered medium	7
7. Reflection and transmission with three interfaces	7
8. Representation of refractive focusing effect	8
9. Refractive focusing coefficient vs ice thickness for several selected radar ranges	8
10. Representation of impulse RF burst	9
11. Representation of a burst of pulses by a synthetic pulse radar	10
12. Time domain display of pulse magnitude on an HP 8510B MMW network analyzer	10
13. Representation of autocorrelation function of complementary codes	11
14. Representation of an FM-CW linear frequency sweep	12
15. An FM-CW radar system	13
16. Typical time series scan for an FM-CW radar	14
17. Typical Fourier-transformed scan for an FM-CW radar	14
18. Effect of bandwidth on resolution of adjacent pulses	15
19. Minimum resolution parameters	15
20. Resolution as a function of maximum radar range	16
21. Pulse-widening effect of windowing	17
22. Parameters defining sweep linearity	17
23. Computer simulation of radar reflections from a 5-cm slab of freshwater ice floating on fresh water	18
24. Example of thickness resolution simulation results	19
25. Attenuation vs ice thickness for $n_i = 0.0001$	20
26. Attenuation vs loss factor for a range of loss factors through a 5-cm-thick sheet of fresh- water ice	20
27. Noise power vs bandwidth	21
28. Sweep time and sweep rate parameters	23
29. FM-CW radar difference frequency vs sweep rate for various radar ranges	24
30. Horizontal displacement per sweep vs sweep rate for a range of typical profiling ground speeds	24
31. Geometry of beamwidth vs thickness relationship	25
32. Antenna beamwidth as a function of ice thickness for reflections from the ice/water interface and air/ice interface at beam pattern edge	25
33. Beam geometry of standard gain 9° antenna	25
34. Footprint diameter for 3-dB antenna beamwidths vs altitude	26

	Page
35. Parameters for determining antenna footprint overlap	26
36. Dimensions of area illuminated by one scan	26
37. Geometric elements for calculating percent overlap of antenna footprint on adjacent scans	26
38. Percentage of 3-dB antenna beamwidth overlap as a function of ground speed, altitude, sweep rate and duty cycle	27
39. Block diagram of the MMW FM-CW radar	29
40. Radar front end	30
41. Amplifier-synchronizer used after mixing	31
42. Record-only mode	32
43. Playback mode	32
44. Playback synchronization decoder	33
45. Typical DSP displays	34
46. Linear stacked-scan waterfall representation of reflections from an 8-cm-thick granite slab	35
47. Radan processed and wiggle-formatted display of reflections from an 8-cm-thick granite slab	35
48. Boom-mounted profiling arrangement	36
49. Pre-prototype mounted on the cart	36
50. Cart-mounted device profiling pond ice	36
51. Cart-mounted radar deployed on a bridge	36
52. Truck-mounted radar	36
53. Radar mounted on a truck using a tripod	36
54. Profiling helicopter	37
55. Segment of skating arena profile	38
56. Sequence of increasing ice thickness on a frozen outdoor pond	39
57. Vertical cross section of an overflow pond ice core	39
58. Indication of surface roughness of overflow pond ice cover	39
59. Radar and borehole measurements from overflow pond	40
60. Post Pond survey path	40
61. Segment of Post Pond profile from survey by cart-mounted radar	40
62. Horizontal and vertical cross sections of 11 January 1991 sample of Post Pond ice core	41
63. Indication of surface roughness of Post pond ice cover	41
64. Segment of Post Pond profile with snowcover	42
65. Segment of Post Pond profile without snowcover taken at 10 km/hr	43
66. Indication of surface roughness of Post Pond ice cover without snowcover	43
67. Horizontal and vertical cross sections of 23 January 1991 sample of Post Pond ice core	43
68. Radar and borehole measurements from Ledyard Bridge	44
69. Indication of maximum surface roughness encountered while profiling Connecticut River ice from Ledyard Bridge	44
70. Turtle Pond survey site near Concord, New Hampshire	45
71. Segment of airborne profile of Turtle Pond	45
72. Pemigewasset River survey site	45
73. Segment of airborne profile of Pemigewasset River near Franklin, New Hampshire	45
74. Error attributable to frequency bin resolution as a function of ice thickness	47
75. T-bar ice thickness measurement tool with offset indicated	48
76. Radar and borehole thickness measurement from tape 6	48
77. Difference between radar and borehole thickness from tape 6	48
78. Radar and borehole thickness measurement for tape 11	49

	Page
79. Difference between radar and borehole thickness from tape 11	49
80. Parameters for analysis of a pulse reflected from a metal plate	50
81. CDF of widths of pulses reflected from a metal plate	51
82. Pulse width asymmetry (windowed data)	51
83. CDF of rectangular windowed pulse	52
84. CDF of Hanning windowed pulse	52
85. Parameters for analysis of a pulse reflected from an ice sheet	53
86. CDF of air/ice interface pulse width	53
87. CDF of ice/water interface pulse width	53
88. CDF of pulse width difference between first and second interface reflected pulses	54
89. CDF of pulse width spreading between first and second interface reflections	54
90. Pulse width asymmetry (interface data)	55
91. CDF of pulse width asymmetry at -5-dB point	55
92. CDF of air/ice pulse width asymmetry	56
93. CDF of ice/water pulse width asymmetry	56
94. Representation of FM-CW radar waveform components used for statistical analysis	57
95. CDF of peak magnitudes	57
96. CDF of peak magnitude differences between air/ice and ice/water interface	58
97. Summary of ice thickness vs peak magnitude difference	58
98. Overlay plot of radar system responses to a metal plate and sky, indicating an approximate 50-dB SNR	58

TABLES

Table

1. Apparent ice thickness for variations in refractive index	5
2. Computer simulation parameters	18
3. Calculation of SNR from typical system parameters	21
4. Typical transmitted power levels and related SNR for given system parameters	22
5. Selection of optimum sweep times	24
6. FM-CW MMW radar specification summary	28
7. System power requirements	37
8. Prototype implementation costs	37
9. Summary of survey studies	38
10. Summary of calculated thickness resolution errors for 5- and 10-cm-thick ice	47
11. Comparison of calculated and measured resolution error	50
12. Comparison of mean pulse widths at -5- and -10-dB measurement points	54
13. Comparison of mean pulse asymmetry at -5- and -10-dB measurement points	56
14. Summary of pulse peak magnitudes survey data	59
15. Comparison of calculated and prototype system SNR	59

NOMENCLATURE

A_e	antenna aperture (m^2)	k_o	wave number in free space ($2\pi/\lambda_o$)
A_{illum}	area illuminated (m^2)	L_1	system losses
A_{ovlp}	area of scan overlap (m^2)	L_2	random propagation losses
A_{sym}	percent of pulse width asymmetry	N	total number of samples
ali	air-to-ice interface boundary	N_{fft}	number of points (bins) in FFT
a/s	air-to-snow interface boundary	n	complex index of refraction of medium
B_n	noise bandwidth	n_a	refractive index of first material at interface boundary
BW	FM-CW swept bandwidth (Hz)	n_b	refractive index of second material at interface boundary
bw	antenna beam angle/2 (degrees)	n_i	imaginary part of the complex index of refraction
c	propagation velocity in free space (m/s)	n_{ice}	refractive index of ice
Dif_n	percent difference between borehole and radar measurements	n_0	refractive index of air
E	complex electric field strength	n_r	real part of the complex index of refraction
E_o	electric field strength	n_{snow}	refractive index of snow
F_{hi5}	trailing edge -5-dB intercept frequency	n_{samp}	number of samples per scan
F_{hi10}	trailing edge -10-dB intercept frequency	NL	nonlinearity of sweep
F_{if}	intermediate frequency	P_a	amplifier noise power
F_{lo5}	leading edge -5-dB intercept frequency	P_n	thermal noise power = KT_oB_n
F_{lo10}	leading edge -10-dB intercept frequency	P_r	average received power
F_{mixer}	mixer noise figure	P_t	average transmitted power
F_n	overall noise figure	r	radius (m)
F_p	pulse peak amplitude intercept frequency	R	range (distance from antenna to ice surface)
F_{r1}	difference frequency of air/ice interface reflection (Hz)	R_{ab}	reflection coefficient at interface boundary ab
F_{r2}	difference frequency of ice/water interface reflection (Hz)	R_{max}	maximum radar range in free space
FC	focus coefficient	R_{res}	range resolution per bin (cm/bin)
f	frequency	S_{Bn}	borehole thickness measurement (cm)
f_{samp}	sampling frequency (Hz)	S_{Rn}	radar thickness measurement (cm)
f_{swp}	sweep frequency (Hz)	s	thickness of an ice sheet
G_r	receiving antenna gain	s_{min}	minimum measurable thickness of an ice sheet
G_t	transmitting antenna gain	s/i	snow-to-ice interface boundary
Gap	spatial gap in coverage between adjacent scans (m)	SNR_i	signal-to-noise ratio at system component input
i/w	ice-to-water interface boundary	SNR_o	signal-to-noise ratio at system component output
j	$\sqrt{-1}$		
K	Boltzmann's constant (1.38×10^{-23} J/K)		
k	wave number		

T_{ab}	transmission coefficient at interface boundary ab	z	resistivity of the medium (W m)
T_{hi5}	one-way travel time to pulse trailing -5-dB point	α	attenuation constant (Np/m)
T_{hi10}	one-way travel time to pulse trailing -10-dB point	β	phase constant (rad/m)
T_{lo5}	one-way travel time to pulse leading -5-dB-point	ΔPW	percentage of pulse width increase i/w to a/i interface
T_{lo10}	one-way travel time to pulse leading -10-dB point	Δt	round-trip travel time
T_o	receiver temperature (290 K)	δf	maximum deviation of modulation from linear
T_p	one-way travel time to pulse peak	ϵ_{mix}	dielectric constant of mix
t_b	propagation time from antenna footprint beam edge	ϵ_o	permittivity of free space (F/m)
t_n	propagation time from nadir ice/water interface point	ϵ_1	dielectric constant of first material
t_{rec}	recovery time between sweeps (s)	ϵ_2	dielectric constant of second material
t_{swp}	FM-CW sweep time (s)	λ	wavelength in medium
v	ground speed (m/s)	λ_o	wavelength in free space (m)
vol_1	volume fraction of first material (air)	μ_x	distribution mean
vol_2	volume fraction of second material (ice)	ϕ	antenna beam angle (degrees)
$W_{A/I}$	air/ice reflection pulse width (ps)	ρ_1	reflection coefficient for first surface
$W_{I/W}$	ice/water reflection pulse width (ps)	ρ_2	reflection coefficient for second surface
$w_{Hann}(n)$	discrete Hanning window function	σ	radar cross-section of target (m ²)
$w_{rect}(n)$	discrete rectangular window function	σ_x	standard deviation
x	real random variable	θ_a	incident angle
		θ_b	refractive angle with respect to vertical
		ω	angular frequency ($2\pi f$)
		v	propagation velocity in a ice
		v^*	complex phase velocity

An Airborne Millimeter-Wave FM-CW Radar for Thickness Profiling of Freshwater Ice

NORBERT E. YANKIELUN

INTRODUCTION

Problem statement

The ability to profile rapidly and accurately the thickness of freshwater ice down to a few centimeters over large surfaces of frozen ponds, lakes and rivers has wide application and utility for ice safety and trafficability studies. Other important applications include monitoring ice flow on rivers and non-destructive measurement of ice sheet thickness for laboratory studies. In addition, the ability to obtain high-resolution profiles of other dielectrics, including man-made materials, may prove to have military, commercial and industrial applications. However, to date, no geophysical device has been able to profile continuously thicknesses of less than 20 cm. The development of an instrument to measure ice thickness in the range of 3 cm or more is addressed by this research effort.

Previous work

The literature contains numerous studies, including Frankenstein (1966), Nevel and Assur (1968), Stevens and Tizzard (1969) and Gold (1971), that investigate and quantify the static and dynamic load-bearing capacity of floating freshwater ice sheets. Minimum ice thickness data for stationary and moving personnel and for a range of vehicle weight classes have been summarized (CRREL 1986) and indicate that for safe transit by a solitary individual, 5 cm is the lower thickness limit. Thus, it is necessary to develop an ability to profile ice thickness to a resolution better than that lower limit, which can provide reliable safety survey profiling for the entire practical range of personnel and vehicular transit possibilities.

Geophysical profiling of the ground, sea ice and

freshwater ice for at least the last 25 years has been successful with only impulse (or short-pulse) and spread spectrum (e.g., Frequency Modulated-Continuous Wave [FM-CW]) radars. Impulse radar employs a sinusoidal pulse of a few cycles length and nanoseconds (or less) in duration, which is then amplified and coupled to an appropriate antenna for transmission. Morey (1974) describes in detail impulse radar technology; a summary of impulse radar technology is presented in Van Etten (1979); Hickman and Edmonds (1983) include a description of impulse radar in a survey of technologies for sensing ice characteristics; and Arcone (1985) provides a general discussion of the techniques for impulse radar profiling of ice with emphasis on frequencies below 1 GHz. Wills (1987) and Riek (1988) summarize the development and application of radar to ice profiling and other geophysical surveys. In spread spectrum radars, the pulsed echo waveforms are synthesized from a broad frequency spectrum (Eaves and Reedy 1987). Ice thickness is then determined from the time separation between ice surface and bottom echoes, given that the pulse is short enough in time to prevent the two reflections from overlapping. In both cases, thickness resolution is directly proportional to the spectral bandwidth of the radar signal.

To date, efforts with impulse radar have not been able to resolve ice thickness to better than about 10 cm, primarily because of the inability to generate a pulse of sufficiently short duration using a field-portable system. Vickers et al. (1974) describe a helicopter-borne short-pulse radar, having a high resolution and a 2.7-GHz center frequency, that is capable of airborne profiling with a minimum resolvable ice thickness of 10 cm. Cooper et al. (1974), Cooper et al. (1976a) and Cooper et al. (1976b) discuss measurement of 29- to 60-

cm-thick freshwater ice with an S-band short-pulse radar from ground-based, helicopter and fixed-wing platforms, with an average difference between borehole ground truth and radar measurements of less than 9.8%. Annan and Davis (1977a) explored the use of VHF impulse radar for both ice thickness (1–2 m) measurement and freshwater bathymetry, with graphic recorder and magnetic tape output. Chudobiak et al. (1978) developed and applied a nanosecond-impulse X-band radar to profile ice with and without snow cover to minimum thicknesses of 14 cm; output was directly displayed on an oscilloscope. Arcone et al. (1986) obtained ground-based thickness measurements of 40-cm freshwater ice sheets and brash ice with 700- and 900-MHz short-pulse radars, and Arcone and Delaney (1987) discussed helicopter-borne continuous river ice profiling at 500 MHz, with a resulting minimum measurable ice thickness of 15 to 20 cm. Later processing of signals from impulse radar profiling data by Riek (1988) and Riek et al. (1990) has lowered the resolution of 900-MHz impulse radar data to the 10-cm range.

Related work with short-pulse radar includes Vickers and Rose (1972), who reported an error of less than 10% from a ground-based radar having a 2.7-GHz center frequency and a 1-ns pulse for measurement of snowpack stratigraphy; Butt and Gamberg (1979) and Rossiter et al. (1980), who applied airborne VHF impulse radar for sounding sea ice thickness; Daly and Arcone (1989), who surveyed freshwater ice from a helicopter using a 500-MHz short-pulse radar, but who could not deduce thickness directly because bottom echoes could not be received; and Arcone et al. (1989), who employed a 6- to 7-ns pulse radar from a helicopter to detect liquid water trapped beneath ice sheets.

The FM-CW technique has not fared any better in resolving ice thickness below 15 cm, primarily because of the unavailability of field-portable sweep oscillators with sufficient bandwidth and power output level. Chudobiak et al. (1974) used a ground-based X-band FM-CW radar to measure freshwater ice thickness to a minimum of 15 cm. Similar results were obtained by Venier and Cross (1975) with an X-band system that was ground mobile and by Venier et al. (1975) with an airborne system, where the radar data were recorded on magnetic tape for later processing and display. Jakkula et al. (1980) have applied an FM-CW mobile radar (1–1.8 GHz) to measure ice and frost thickness on bogs, providing a real-time display by means of a bank of 32 bandpass filters and a LED matrix, but only to a minimum theoretical thickness of 10 cm in ice. Their measurements were made on ice significantly thicker than the minimum capability.

Several related geophysical applications of FM-CW

radar techniques have been reported. Wittman and Stoltenberg (1981) developed a 1- to 2-GHz FM-CW radar as a general remote sensing instrument, but did not measure ice thickness with it. Gubler and Hiller (1984) and Gubler et al. (1985) employed an 8- to 12.4-GHz FM-CW radar specifically for snowpack stratigraphy and avalanche research; Ellerbruch and Boyne (1980) employed an 8- to 12-GHz FM-CW radar to study snow stratigraphy and water equivalence; and an L-band FM-CW system was used to detect small objects buried as deep as 80 cm in a wet snowpack by Yamaguchi et al. (1991). None of these efforts, however, attempted to make ice thickness measurements.

Several other techniques also exist that rely on ultrasonic or electrical capacitance sensing to determine ice thickness, but have been deemed unacceptable alternatives since physical contact or nearness to the ice sheet is required, as well as a long dwell time at the point of measurement. Thus, the majority of the effort to date has been with impulse or FM-CW radars, requiring playback and processing in the laboratory prior to display, at center frequencies of less than 10 GHz and relatively narrow bandwidths, with resulting minimum ice thickness resolution on the order of 10 cm. These characteristics, representative of the current state of the art in radar profiling of ice thickness, are inadequate for the real-time, continuous, high-resolution ice safety and trafficability survey application previously described.

Objective

The objective of this research is to develop an airborne-deployable, real-time, high-resolution radar system for continuous, large-scale river and lake surveying. The key aspect here is to improve the current lower limit of freshwater ice thickness measurement to clearly and accurately profile ice that is less than 5 cm thick. The real-time and continuous aspects are necessary to minimize delay in interpreting data when dangerous conditions are encountered.

Procedures

After a survey of available technologies, a prototype millimeter wave (henceforth, MMW) FM-CW system, equipped with a Digital Signal Processing (DSP) co-processor, was developed to allow continuous recording of echo scans for later playback and processing. The system was then operated from stationary and mobile ground platforms and flown in a helicopter over natural river and lake ice sheets with and without snow cover. Data were processed to reveal surface and bottom reflection profiles, the time separation of which was used to determine ice thickness. The results were then compared with ground truth measurements.

ELECTROMAGNETIC PROPAGATION IN ICE

The basis of radar ice thickness profiling is the measurement of the time delay of a radar pulse propagating through a sheet of ice. To make this measurement and interpret the results, the radar range equation and the theory of wave propagation through a dielectric medium must be employed.

Radar range equation

The radar range equation is used to determine the average power received P_r from a target when illuminated by a radar signal where radar system, propagation path and target parameters are known. Development of the radar range equation is well documented (e.g., Barton 1988). Later, in the *Specifications* section, a detailed discussion of the geophysical form of the radar range equation is provided. A parsing of the radar range equation, as done by Eves and Reedy (1987), lends clarity to its derivation.

$$\text{Power radiated toward the target} = P_t G_t \quad (1)$$

where P_t = average transmitted power and G_t = transmitting antenna gain.

$$\text{Power density at the target} = (P_t G_t) \left(\frac{1}{4\pi R^2} \right) \quad (2)$$

where R = range (m) (distance from antenna to ice surface).

Equivalent power reradiated toward the

$$\text{radar} = (P_t G_t) \left(\frac{1}{4\pi R^2} \right) (\sigma) \quad (3)$$

where σ = radar cross section of target (m^2).

Power density of the reflected wave at

$$\text{the radar} = (P_t G_t) \left(\frac{1}{4\pi R^2} \right) (\sigma) \left(\frac{1}{4\pi R^2} \right) \quad (4)$$

Power received at the radar

$$= (P_t G_t) \left(\frac{1}{4\pi R^2} \right) (\sigma) \left(\frac{1}{4\pi R^2} \right) (A_e) \quad (5)$$

where

$$A_e = \text{antenna aperture} (\text{m}^2) = \frac{G_r \lambda^2}{4\pi} \quad (6)$$

where G_r = receiving antenna gain and λ = wavelength.

Substituting eq 6 into eq 5, and including incurred power losses, we formally state the received power P_r as

$$P_r = \frac{P_t G_t G_r \lambda^2 \sigma L_1 L_2}{(4\pi)^3 R^4} e^{-4\alpha R} \quad (7)$$

where L_1 = system losses

L_2 = propagation scattering losses

α = absorption attenuation rate.

Electromagnetic velocity

The fundamental relationship for wave propagation through a dielectric medium is

$$v = \frac{2s}{\Delta t} = \frac{c}{n_r} \quad (8)$$

where v = propagation velocity in ice

s = thickness of an ice sheet

Δt = round-trip travel time in ice

c = propagation velocity in free space

n_r = real part of the complex index of refraction of ice n .

Thus, the thickness s of an ice sheet can be determined from the equation when v and Δt are known. Ambiguities in measuring Δt arise from changes in the shape of the radar waveform as it propagates through dielectric media encountered. Beam spreading and reflection boundary effects mainly affect signal strength, while dispersion considerations can cause waveform distortion. These phenomena depend strongly on n , which is related to the dielectric permittivity ϵ , discussed next.

Dielectric permittivity of ice, water and snow

Reflection, transmission, propagation and dispersion depend on the absolute and relative dielectric permittivities of all materials involved. The index of refraction n , or the permittivity $\epsilon = n^2$, is found in the theory of wave propagation in dielectric media, generally described in many texts (e.g., Hayt 1967, Seshardi 1971). A geophysical remote sensing perspective is given by Ulaby et al. (1981). Following standard exponential notation, we may describe a scalar plane wave propagating in the general direction r by

$$E = E_0 e^{j\omega \left(t - \frac{k}{\omega} r \right)} \quad (9)$$

where E = complex electric field strength

E_0 = electric field strength amplitude

$j = \sqrt{-1}$

ω = angular frequency ($2\pi f$)

f = frequency

t = time
 k = complex wave number ($2\pi/\lambda$) in medium
 λ = wavelength in medium
 r = displacement vector.

The complex phase velocity v^* of the wave is

$$v^* = \frac{\omega}{k} \quad (10)$$

where $k = k_0 n$
 k_0 = wave number in free space ($2\pi/\lambda_0$)
 λ_0 = wavelength in free space
 n = complex index of refraction of medium.

Complex relative dielectric permittivity is defined as $\epsilon = \epsilon' - j\epsilon''$, where ϵ' is the dielectric constant and ϵ'' is the loss. These terms are related to the real (n_r) and imaginary (n_i) parts of the complex index of refraction n by

$$\epsilon' = n_r^2 - n_i^2 \quad (11)$$

$$\epsilon'' = 2n_r n_i$$

For low loss materials, such as freshwater ice, at the frequencies of interest $n_i \ll n_r$, so that

$$\epsilon' = n_r^2. \quad (12)$$

Measured and theoretical values have been published for ϵ' or n_r , or both, for freshwater ice (e.g., Ray 1972, Vickers 1975, Blue 1980, Matzler and Wegmuller 1987) and snow (e.g., Cummings 1952, Hallikainen et al. 1986, Hallikainen et al. 1987) that cover the microwave and millimeter wave range. Variations in the actual value of n_{ice} (for simplicity n_{ice} will henceforth refer to the real part of the ice refractive index) from the "standard" value of about 1.77, as indicated in Cummings (1952) and Ray (1972), are caused by temperature change, stratigraphic variation, ice matrix porosity or metamorphosis and will cause erroneous interpretation of ice thickness. From the water and ice permittivity algorithm and data presented in Ray (1972) and illustrated in Figure 1, it can be seen that both the real and imaginary components of the permittivity of solid, cold freshwater ice remain virtually constant across the K_a -band at temperatures below 0°C.

Liquid water, on the other hand (Fig. 2), exhibits a significant variation in both real and imaginary components of dielectric constant, which is both temperature and frequency dependent across the K_a -band (26–40 GHz).

In applying radar to measuring ice thickness, the variation of water permittivity affects the reflection

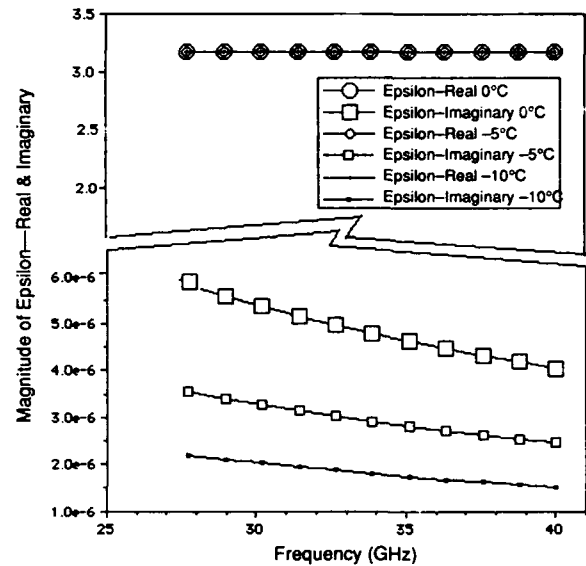


Figure 1. ϵ_r and ϵ_i of freshwater ice as a function of frequency and temperature (after Ray 1972).

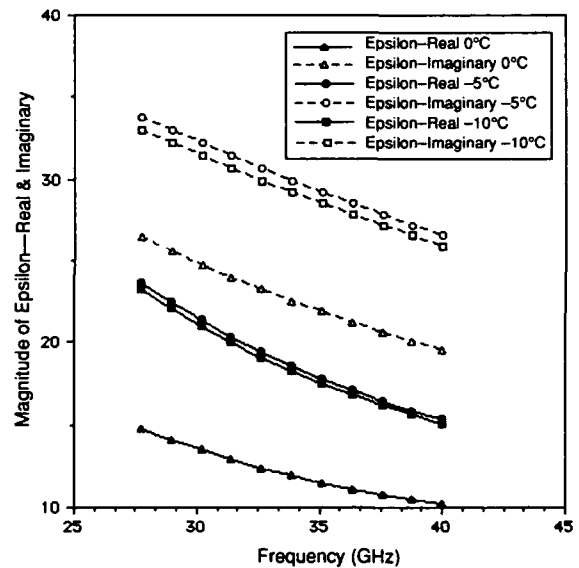


Figure 2. ϵ_r and ϵ_i of fresh water as a function of frequency and temperature (after Ray 1972).

coefficient and resultant amplitude of the reflected signal at the ice/water boundary, but does not otherwise interfere with the accuracy or resolution of ice thickness measurement. The significance of the reflection coefficient will be discussed later.

The inclusion of air bubbles is another factor that affects the dielectric constant of freshwater river and lake ice. Gow and Langston (1977) indicate that typical cross-sectional diameters of air bubbles in lake or river ice are less than 1 mm and that the total air volume is typically less than 5%, although a wide variation can be expected. At air volumes less than 20%, the dielectric

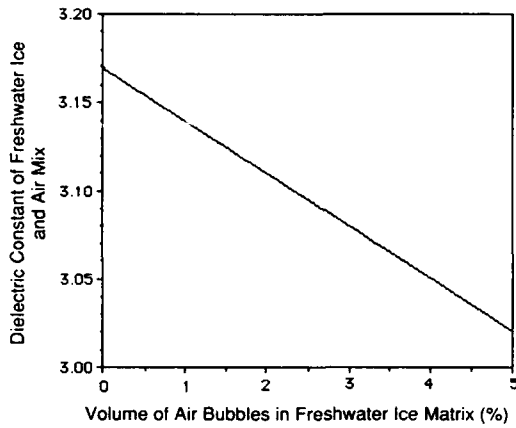


Figure 3. Dielectric constant of freshwater ice with air bubbles as a function of percent air by volume.

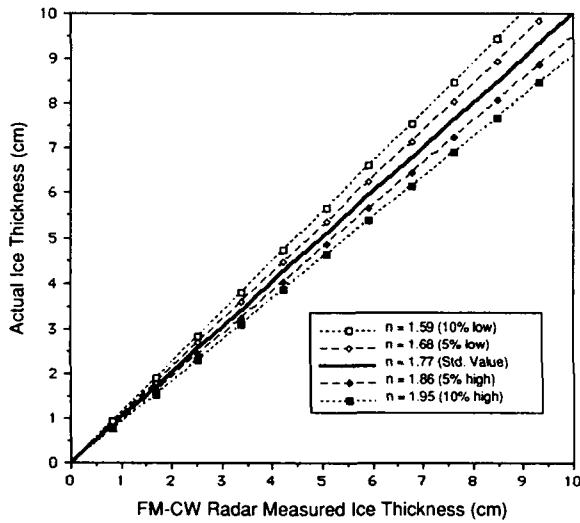


Figure 4. Measured ice thickness vs actual ice thickness based on ± 5 and $\pm 10\%$ variation in refractive index.

mixing formula of Landau and Lifshitz (1960) and used by Nelson et al. (1989) states that

$$\epsilon_{\text{mix}} = \left[(\text{vol}_1) \sqrt[3]{\epsilon_1} + (\text{vol}_2) \sqrt[3]{\epsilon_2} \right]^3 \quad (13)$$

where ϵ_{mix} = dielectric constant of mix
 ϵ_1 = dielectric of first material
 ϵ_2 = dielectric of second material
 vol_1 = volume fraction of first material (air)
 vol_2 = volume fraction of second material (ice).

Figure 3 illustrates the application of this formula to an air and ice mixture. Here, an error in dielectric constant of freshwater ice introduced by air bubble inclusions is less than 5% over the practical range of interest. This error will translate into an error in interpreting s as determined by eq 1. For example, Figure 4 and Table 1

Table 1. Apparent ice thickness for variations in refractive index.

Percent deviation n_{ice} from 1.77	Calculated		Measured thickness (cm)	
	n_{ice}	ϵ_{ice}	5-cm ice	182-cm ice
-10	1.59	2.53	4.50	200.2
-5	1.68	2.82	4.75	191.1
0.0	1.77	3.12	5.00	182.0
5	1.86	3.45	5.25	172.9
10	1.95	3.79	5.50	163.8

indicate the calculated thickness of ice when the actual value of n_{ice} varies by ± 5 and $\pm 10\%$ from the "standard" value of $n_{\text{ice}} = 1.77$. For a practical air volume of 5%, the error in thickness would be -2.2% .

In Cummings (1952), permittivity measurements at 10 GHz and -18°C with snow samples of varying densities indicate that snow with density between 0.7 and 0.8 g/cm^3 provides permittivities between 2.5 and 2.8, which lie close to the 10 and 5% uncertainty limits listed above. Additional data in Cummings (1952) indicate a value of 3.15 for ϵ_{ice} (density = 1 g/cm^3). This would seem to indicate that, in terms of permittivity, cold (below 0°C) ice and snow with densities as low as 0.7 g/cm^3 should provide thickness measurements within a 10% thickness error tolerance.

For warming ice, a melting or saturated snow cover, and candled ice, thickness measurement based on use of a "standard" value of n_{ice} is more uncertain. The bulk dielectric constant of an ice crystal/water matrix is significantly increased above that of cold ice, proving this method of measurement unreliable. In Arcone et al. (1986), measurement of $\epsilon_{\text{ice}} = 4.1$ was made for ice undergoing grain boundary melting; 4.1 translates to about a 1% water content by volume. This higher index of refraction provides an increased reflection coefficient at the air/ice boundary (top surface), thereby significantly attenuating the signal power that is transmitted through the slab and, consequently, is reflected from the ice/water boundary (bottom surface). Additionally, the loss component of the index of refraction n_i increases from near zero to a significant value as the ice warms and melts. This further attenuates the pulse signal through the warming ice slab.

These considerations limit the range of conditions over which the radar may be reliably used given a "standard" n_{ice} of 1.77. It appears that the radar can be designed to indicate ice thickness with an error of less than $\pm 10\%$ over the specified thickness measurement range. Accurate thickness measurement of cold ice and ice/snow configurations with a density of greater than 0.7 g/cm^3 is possible. Accurate thickness measurement of warm, wet ice or ice/snow configurations appears less feasible, but demands further experimental investigation.

Transmission and reflection processes

A mismatch of refractive indices exists at an interface of two different dielectric materials. This causes a fraction of incident electromagnetic energy to be reflected back from the interface, while the complementary fraction of the energy is transmitted through the interface. The fraction of the energy reflected back depends on the reflection coefficient. Assuming that we considered no losses ascribable to the medium, then

$$R_{ab}^2 + T_{ab}^2 = 1 \quad (14)$$

where R_{ab} is the field strength reflection coefficient at interface boundary ab and T_{ab} is the field strength transmission coefficient at interface boundary ab .

It is the dielectric discontinuity at the air/ice and ice/water interfaces and respective reflection coefficients that make the measurement of ice thickness by electromagnetic means possible. Brekhovskikh (1980), Ulaby et al. (1981) and Arcone (1984) discuss the reflection coefficient and its relation to electromagnetic and acoustic propagation in multi-layered dielectric media. At an arbitrary planar dielectric interface boundary ab , the reflection coefficient is defined as

$$R_{ab} = \frac{n_a \cos(\theta_b) - n_b \cos(\theta_a)}{n_a \cos(\theta_b) + n_b \cos(\theta_a)} \quad (15)$$

where n_a = refractive index of first material at interface boundary

n_b = refractive index of second material at interface boundary

θ_a = incident angle

θ_b = refractive angle, with respect to vertical.

Then, under Snell's law with a normal incident angle (θ_a goes to zero) and the associated normal refractive angle (θ_b goes to zero), the reflection coefficient for a normal incident wave upon an arbitrary dielectric boundary discontinuity results in

$$R_{ab} = \frac{n_a - n_b}{n_a + n_b} \quad (16)$$

Each dielectric layer of a multi-layered medium permits multiple reflections and transmissions at increasingly attenuated levels. In a multiple layered medium, discerning the primary and subsequent multiple reflections from each interface can be confusing and creates a more complex analytical problem than in a two- or three-interface medium. To determine ice thickness, it is necessary to consider only the initial reflections from each interface.

Figure 5 illustrates the dielectric interface reflection

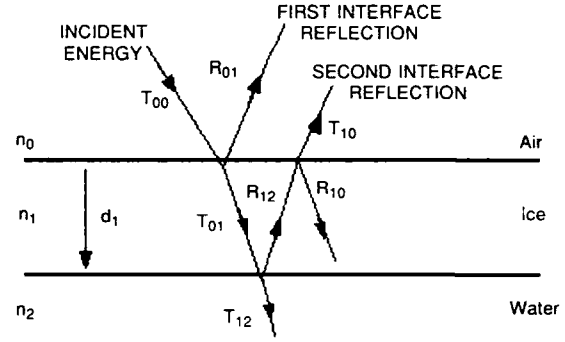


Figure 5. Reflection and transmission with two interfaces.

tions and transmissions pertinent to thickness measurement for a two-interface (air/ice, ice/water) dielectric medium. (While in practice, pertinent incident and reflected energy would propagate normal to the surface, the rays have been angled in the figure for illustrative clarity.)

Here, the power reflected by the air/ice boundary is attributable solely to the first interface reflection coefficient R_{01} , which, for consistency of notation later, can be denoted as ρ_1 .

$$R_{01} = \rho_1 = \frac{n_0 - n_1}{n_0 + n_1} \quad (17)$$

The power returned to the surface from the second ice/water interface is ascribable to the product of the transmission and reflection coefficients T_{01} , R_{12} and T_{10} or

$$\rho_2 = (T_{01})(R_{12})(T_{10}) \quad (18)$$

where the subscripts indicate the specific interface between dielectric layers and the direction of propagation. This can be further represented as

$$\rho_2 = (1 - R_{01})(R_{12})(1 - R_{10})$$

or

$$\rho_2 = \left(1 - \frac{n_0 - n_1}{n_0 + n_1}\right) \left(\frac{n_1 - n_2}{n_1 + n_2}\right) \left(1 - \frac{n_1 - n_0}{n_0 + n_1}\right)$$

and eventually as

$$\rho_2 = \left(\frac{4n_0n_1}{(n_0 + n_1)^2}\right) \left(\frac{n_1 - n_2}{n_1 + n_2}\right) \quad (19)$$

where n_0 , n_1 and n_2 represent the indices of refraction of each of the layers in the medium.

Figure 6 illustrates the relative magnitude of ρ_1 and

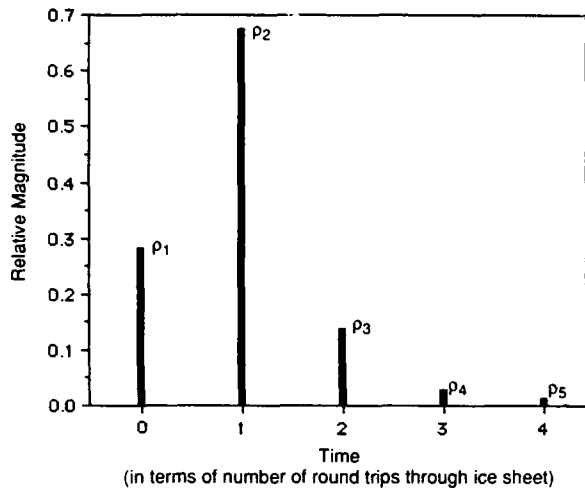


Figure 6. Relative magnitudes of reflections from an air/ice/water multi-layered medium.

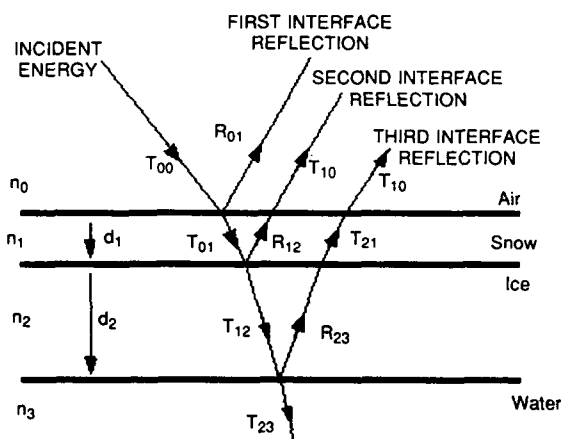


Figure 7. Reflection and transmission with three interfaces.

ρ_2 for an air/ice/water multi-layered dielectric medium. Here also, ρ_3 , ρ_4 and ρ_5 indicate the relative magnitude of subsequent returns occurring after multiple internal reflections in the ice sheet. The relative magnitude of these multiples rapidly becomes insignificant.

Figure 7 illustrates the dielectric interface reflections and transmissions pertinent to thickness measurement for a three-interface (air/snow, snow/ice and ice/water) dielectric medium. In the three-interface case, the power reflected by the first two interfaces can be calculated in a similar manner to that indicated above, and the reflected power at the surface from the third interface follows as

$$\rho_3 = (T_{01})(T_{12})(R_{23})(T_{21})(T_{10})$$

or

$$\rho_3 = \left(\frac{4n_0n_1}{(n_0 + n_1)^2} \right) \left(\frac{4n_1n_2}{(n_1 + n_2)^2} \right) \left(\frac{|n_2 - n_3|}{n_2 + n_3} \right). \quad (20)$$

In the case of an air/snow, snow/ice and ice/water boundary configuration, the lack of a substantial dielectric contrast between air and cold, low-density snow prevents strong reflections from this interface (ρ_1) compared with the reflections from the subsequent boundaries (ρ_2 and ρ_3).

Attenuation losses

Signal attenuation because of propagation through lossy resistive media is described in Ulaby et al. (1981) and can be determined from the refractive index n .

$$n = n_r - jn_i = \left(\frac{\beta - j\alpha}{k_0} \right) = \frac{j\omega}{k_0 c} \sqrt{\epsilon - \frac{j}{\omega z \epsilon_0}} \quad (21)$$

where α = attenuation constant (Np/m)

β = phase constant (rad/m)

ϵ_0 = permittivity of free space (F/m)

λ_0 = wavelength in free space (m)

z = resistivity of the medium (W m).

The signal attenuation (dB/m) because of resistive losses is taken as

$$A = 20 \log_{10}(\alpha). \quad (22)$$

For freshwater ice, ϵ'' is so small (Fig. 1) and z typically $\geq 5000 \Omega\text{m}$ (Gow and Langston 1977) that

$$\alpha \approx 0$$

and

$$\beta \approx \omega \sqrt{\epsilon} = \frac{2\pi}{\lambda}$$

Geometric spreading losses

Geometric spreading contributes to the attenuation of signal power. As the signal travels to, and is reflected from, a point target, the power density per square meter decreases at a rate proportional to the fourth power of range. A flat reflector, however, gives a decrease proportional to the second power. This factor is included in radar range analysis calculations discussed in the *Specifications* section. For now it suffices to say that at a helicopter altitude of 3–7 m, an ice sheet thickness of less than 20 cm presents insignificant spreading attenuation of the bottom reflection relative to the surface reflection.

Refraction and focusing effect

Focusing of the beam caused by refraction at the air/

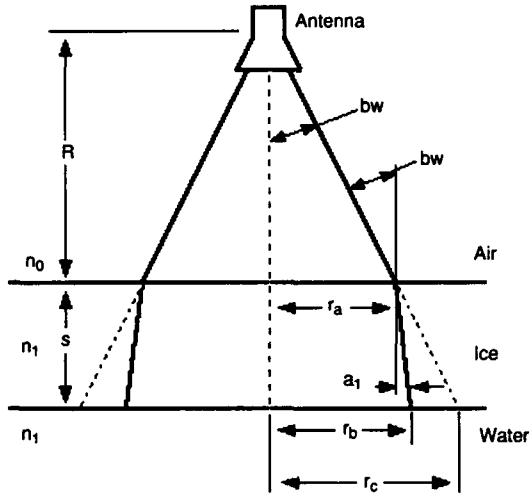


Figure 8. Representation of refractive focusing effect.

ice interface boundary will give some amplification to the bottom reflection. Although the rays leave the ice sheet at the same angle they entered, the beam has been collimated over the double thickness of the ice sheet. Figure 8 illustrates the geometrical parameters that are used with Snell's Law to calculate the focusing effect for an airborne antenna above an ice sheet. This effect is factored into subsequent radar range analysis calculations. The radius of the 3-dB beamwidth footprint at the air/ice interface r_a is calculated as

$$r_a = R \tan(bw) \quad (23)$$

where bw = antenna beam angle/2 and R = range from antenna to surface.

From Snell's Law for refraction, the refracted angle is calculated as

$$a_1 = \sin^{-1} \left(\frac{n_0}{n_{ice}} \sin(bw) \right) \quad (24)$$

where a_1 = angle of refraction in ice
 n_0 = refractive index of air
 n_{ice} = refractive index of ice.

Accounting for the effect of refraction at the ice/water interface r_b , we calculated the 3-dB antenna footprint radius as

$$r_b = r_a + s \tan(a_1) \quad (25)$$

where s is ice thickness.

Ignoring the effects of refraction at the ice/water interface r_c , we calculated the 3-dB antenna footprint radius as

$$r_c = (R + s) \tan(bw). \quad (26)$$

Finally, the focus coefficient FC is calculated as

$$FC = \frac{r_c^2}{r_b^2} \quad (27)$$

and in terms of decibels FC_{dB} as

$$FC_{dB} = 10 \log(FC) = 10 \log \left(\frac{r_c^2}{r_b^2} \right). \quad (28)$$

Figure 9 illustrates the result of these calculations for

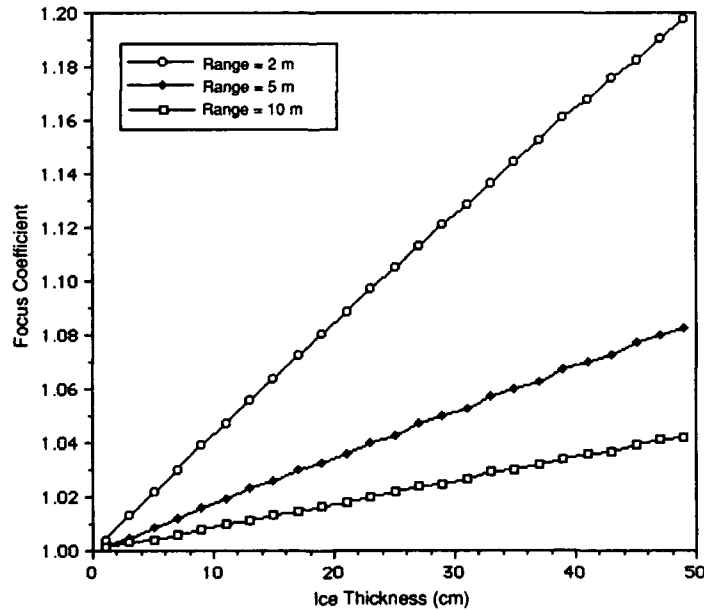


Figure 9. Refractive focusing coefficient vs ice thickness for several selected radar ranges (calculated for a 9° beamwidth horn antenna).

a variety of radar ranges and ice thicknesses. For example, at a range of 5 m above a 30-cm-thick sheet of ice, the focus coefficient is approximately 1.05, or converted to decibels, $FC_{dB} = 0.21$ dB.

External random noise

Sources of noncoherent reflected energy are classified as external random noise and are caused by surface and volume scattering. Ulaby et al. (1981) present several analytical models for the scattering process and discuss the implications of surface and volume scattering on the magnitude of the received reflected energy. Simply, specular (coherent) reflection of an impinging electromagnetic wave occurs at a dielectric interface where the two media form a smooth, infinite plane. Obeying Fresnel reflection laws, a reflection from this interface would not be visible with a monostatic radar unless it was positioned at nadir relative to the ice. Backscatter from a rough-surfaced dielectric interface would be sent in all directions and may be noncoherent or partially coherent.

Surface scattering is frequency dependent relative to the dimensions of the surface geometry (both large and small-scale surface variations). Both signal strength and pulse shape are adversely affected by surface scattering. Generally, specular scattering amplitude decreases while noncoherent scatter intensifies as surface roughness increases. Jezek et al. (1988) show that for a given wavelength, the skewness of a Rice-type amplitude distribution increases with surface roughness. When the surface is smooth compared to the wavelength, and backscatter is dominated by the coherent specular return, the Probability Distribution Function (PDF) of the backscatter magnitude is nearly normal. As the surface roughness increases and incoherent scatter becomes more significant, the backscatter magnitude PDF skews toward a Rayleigh distribution. The Rayleigh roughness criterion describes the maximum surface irregularity that will not substantially lower the reflection coefficient. The criterion states that, if the surface irregularities result in path-length variations that are significantly less than one wavelength, the surface can be considered as smooth. A smooth surface is defined as having variations on the order of $< \lambda/4$ (Eaves and Reedy 1987).

Dielectric inhomogeneities existing within a volume result in volume scattering of the radar signal propagating through the medium. In naturally occurring freshwater ice, the primary contribution to the volume inhomogeneity is from air bubble inclusions. The typical range of dimension and density of these inclusions are discussed in the *Dielectric Permittivity of Ice, Water and Snow* section. Volume scattering causes a redirection of some of the transmitted energy, resulting in an attenuation of the transmitted wave. The scattering

strength is proportional to the magnitude of the dielectric discontinuity and the density of the imbedded scatterers. Additionally, volume scattering is frequency dependent relative to the dimension and geometry of the air bubble inclusions and their spacing within the ice matrix. Both reflected signal strength and pulse shape are adversely affected by volume scattering.

RADAR TECHNOLOGIES

All radar technologies investigated here ultimately rely on a pulse with a large bandwidth and narrow time domain that is capable of distinguishing top and bottom ice layer surfaces. Trade-offs between resolution, power, signal-to-noise ratio and speed of data processing exist for all systems and each are examined to conclude which type is best suited for this thin ice profiling application. Of the several available options, impulse radar has been in constant use since the early 1970s and has demonstrated the least potential for achieving state of the art signal-to-noise ratio and performance; the radar inherently sacrifices much to gain a short pulse. It, therefore, is described first to be used as a basis of comparison with the other available technologies.

Impulse radar

Background information on the theory of impulse radar is discussed in Chudobiak et al. (1978), Arcone (1985), Currie and Brown (1987) and Wehner (1987). Briefly, a 1–2 cycle burst of RF (radio frequency) energy with a narrow pulse envelope (Fig. 10) is generated, transmitted and travels toward the target. It is reflected by the target back to the receiver, where it is then sampled to be converted to the audio range for recording and processing. The sampling process inherently creates random noise. All radars today use very low gain antennas to achieve narrow pulse widths.

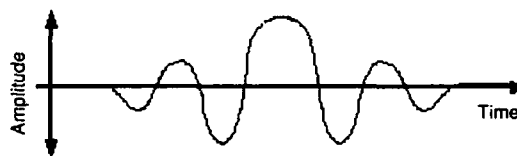


Figure 10. Representation of impulse RF burst.

Advantages

Low complexity. At microwave and lower frequencies, impulse radar designs are relatively simple. Systems discussed earlier by Vickers and Rose (1972), Chudobiak et al. (1978), etc., employ simply a pulser and an oscilloscope. To a significant degree, systems can be built from commercially available hardware.

Minimal signal processing. Ice thickness can be

measured using only a single return of raw data. This limited signal processing allows the thickness measurement to be displayed in real time.

Disadvantages

Antenna considerations. Depending on the bandwidth of the radar pulse and the antenna configuration, there may be undesirable pulse wave shaping at the antenna. Currently available technology dictates the use of low-gain antennas (7 dB at most) to limit this pulse distortion effect. There are no practical, high-gain, short-pulse radar antennas apparent in the literature. Significant clutter is evident, even with shielded antennas. Shielding, while lessening the effects of clutter, tends to lengthen the radar pulse, decreasing the ability of the radar to measure accurately thin ice thickness.

Sampling noise floor. Traditionally, impulse radars use sampling techniques to reconstruct VHF-UHF (very high frequency-ultra high frequency) signals in the audio range for later display and recording on magnetic tape. The sampling process generates about a 40- to 50-dB noise floor.

Low average power-low performance figure. With sampling, several thousand pulses at VHF-UHF must be used to recreate one pulse at audio frequencies. This is a waste of power and a drain on batteries. With a low power impulse and low gain antennas, system performance figures rarely exceed approximately 110 dB.

State of the art pulse-forming technology. High-resolution requires a broad bandwidth and, consequently, a proportionally narrow impulse must be generated. Resolving thickness on the order of a few centimeters requires a pulse width on the order of hundreds of picoseconds. Two approaches are suggested in the literature. The first is gallium arsenide circuit component

technology, currently limited to 200-ps pulse widths at very low output power, as illustrated by Avtek (1989). The second is electro-optic pulse generation techniques discussed by Valdmanis and Mourou (1986), Paulus et al. (1987), Auston and Nuss (1988), Paulter (1988) and Paulter et al. (1988). While both of these techniques are capable of generating sub-nanosecond pulses, they appear to be highly experimental laboratory implementations, not generally available and, therefore, not readily suited for application in a field-portable instrument.

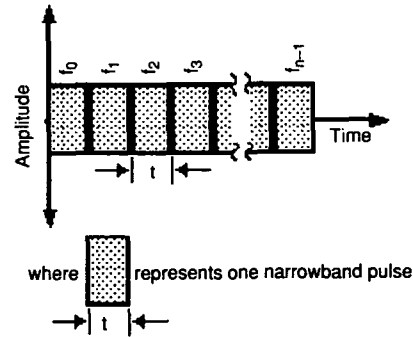


Figure 11. Representation of a burst of pulses by a synthetic pulse radar.

Synthetic pulse radar

Technical discussions of synthetic pulse radar are given in Ulaby et al. (1981), Wehner (1987) and in industrial microwave/MMW network analyzer operation manuals (e.g., Hewlett-Packard). Conceptually, a synthetic pulse radar transmits a burst of an integral number of narrow band pulses, as represented in Figure 11. Each narrow band pulse in a burst series is displaced by a uniform frequency step to span the full bandwidth of the radar. The spectrum of a wide band pulse is

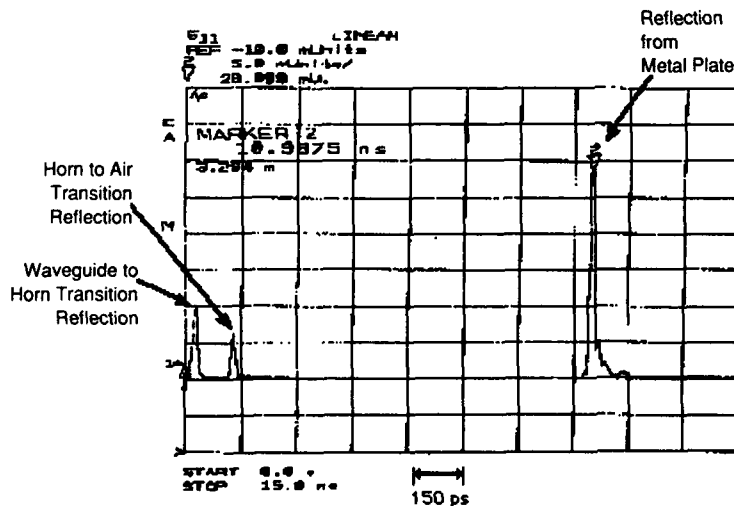


Figure 12. Time domain display of pulse magnitude on an HP 8510B MMW network analyzer (waveguide-to-horn transition, horn-to-air transition and reflection from a metal plate at a range of approximately 1.5 m are indicated).

formed when phase and amplitude components from each pulse in a burst series are combined. Each burst is coupled to an antenna, transmitted, reflected from the target, and the received phase and amplitude information is stored. An inverse Fourier transform is computed from the received phase and amplitude spectra, resulting in a time domain representation of the reflected, synthesized wide band pulse. Figure 12 is a typical time domain display of a radar reflection from a metal plate using an HP 8510B (Hewlett-Packard) network analyzer configured as a MMW synthetic pulse radar.

Advantages

Extremely high resolution. When appropriately configured, setups such as the HP 8510B are capable of range resolutions of less than 1 cm. This requires a broad bandwidth (>13 GHz), a large number of sampled frequencies in the bandwidth (801) and lengthy acquisition and processing times (≈ 150 s).

Low transmitted power. The spectrum of a large amplitude radar pulse can be synthesized from the many lower power frequency components required to form the pulse.

High signal-to-noise ratio. Synthetic pulse systems, exemplified by the HP 8510B, allow for multiple samples at each synthesized frequency. When these samples are averaged by the system, a substantial improvement in Signal-to-Noise Ratio (SNR) ratio can be obtained, but with a proportional increase in processing time.

Disadvantages

While this system provides excellent results in the laboratory, there are some disadvantages for field or airborne deployment. These include the following.

Expensive hardware. The HP 8510B configured as an MMW radar costs approximately \$200,000 (1991 dollars), too expensive for common deployment and for exposure to typical field environments and handling.

Slow data collection, analysis and display time. The fastest system throughput is 4 seconds per synthetic pulse. This is too slow for airborne applications with typical flight ground speeds of 2 to 9 m/s. (The dwell time required per sample is too great.)

Limited range. At the highest throughput, 4 seconds per pulse and a pulse bandwidth of 3 GHz, the system's maximum range is only 5 m. This is near the minimum limit of altitude of typical helicopter survey flights.

Not portable. The HP 8510B is intended as a laboratory instrument, not for field or airborne application. Fully configured, it weighs more than 200 kg, occupies close to a cubic meter and requires 10 A at 120 V (rms), 60 Hz, for operation. It is not designed to be portable, nor is it field-hardened.

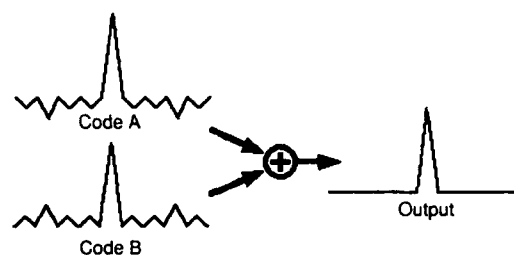


Figure 13. Representation of autocorrelation function of complementary codes.

Coded radar

Wehner (1987) and Wills (1987) provide technical discussions of digital phase coded radar and Wills (1987) developed a working prototype operating at 40 MHz. Briefly, a pair of complementary coded digital sequences with power-of-two length are consecutively transmitted. When the autocorrelation functions of both codes are added together, a perfect autocorrelation response without time sidelobes results (Fig. 13). Coded radars provide a satisfactory alternative for some geophysical profiling applications. However, there are serious considerations that eliminate it from possible MMW implementation.

Advantages

Low noise. High SNRs are attainable, since both in-phase and quadrature signal components are available for processing. (Both magnitude and phase can therefore be derived.) When scans are integrated, an SNR improvement proportional to the number of integrated scans is obtained. In an instrument where only magnitude information is available, the SNR improvement is proportional to only the square root of the number of integrated scans.

Improved range ability. Long transmitted pulse sequences produce greater average transmitted power and permit longer range capability.

Disadvantages

Complexity. The coded radars are considerably more complex than either the FM-CW or pulse radars because, at least in part, of their code generation and signal processing hardware and software. For the level of resolution required by the radar design under consideration, it does not appear that this level of complexity provides any increased advantage over simpler apparatus.

Expense. A cost of \$53,000.00 (less overhead and profit) was estimated by Wills (1987) to develop a VHF digital phase-coded ground-probing radar. We can expect that, if feasible, an MMW system of this type, given the greater cost of the higher frequency hardware required, would be prohibitively expensive.

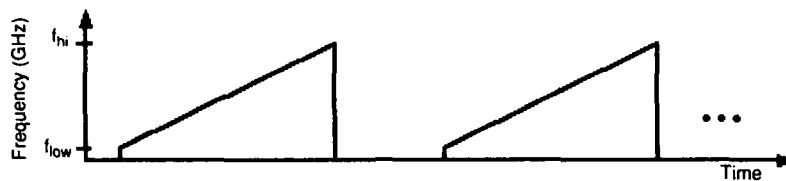


Figure 14. Representation of an FM-CW linear frequency sweep.

Hardware limitations. Even if the two former issues are not thought to limit this application, digital hardware for generating the necessary coded pulse trains at gigahertz switching frequencies is currently unavailable.

FM-CW radar

Detailed technical descriptions of FM-CW (Frequency Modulated–Continuous Wave) radar are given in Venier et al. (1975), Wittmann and Stoltenberg (1981) and Currie and Brown (1987). Basically, the output of a linear sweep oscillator (Fig. 14) is transmitted toward the target. The received energy, reflected back from the target, is mixed with a sample of the sweep oscillator output. The difference frequency is detected. This difference frequency is proportional to the target range and can be determined using spectral analysis techniques. With two primary scattering boundaries, as in the case of the air/ice and the ice/water interfaces found on a sheet of ice floating on water, ideally there will be two distinct frequency components, one from each of the interfaces. The difference between these two frequencies is proportional to the distance between the two interfaces.

Advantages

Simple RF design. In its most fundamental form, an FM-CW radar consists of very few components: a sweep oscillator, a power divider, a mixer, a spectrum analyzer and two antennas. The sweep oscillator serves as both the transmitter and local oscillator signal source.

General availability of components. The MMW and low-frequency components required are readily available from several major manufacturers. The key component is the MMW sweep oscillator, models of which now are specified to maintain better than a $\pm 0.1\%$ sweep linearity at 10- to 15-dBm power levels across the entire K_a -band.

High resolution. By taking advantage of the full K_a -bandwidth of available MMW sweep oscillators, a theoretical resolution on the order of 1 cm or less is possible.

High average power. The FM-CW radar continuously transmits a sweep frequency signal of constant amplitude.

Disadvantages

Transmitter–receiver isolation. In FM-CW radar the sweep oscillator is continuously generating an RF output signal. The transmitting antenna needs to be isolated from the receiving antenna so that inter-antenna coupling is minimized. This coupling, at worst, could damage the receiver elements and, at least, overload the receiver front end, inhibiting the detection of the reflected signal energy. Isolation also aids in minimizing inter-antenna reflections, which appear as spurious responses. These problems can be somewhat alleviated by adjusting the transmitter power to a sufficiently low level to avoid receiver saturation.

Sweep linearity. For high range resolution, an extremely linear sweep oscillator is required. The wider frequency deviation that is required in a broadbanded system may be difficult and expensive to make linear.

Homodyne mixing noise. Currie and Brown (1987) suggest that a balanced mixer and high gain preamplifier may be required to overcome the effects of high noise associated with the homodyne mixing process, potentially increasing complexity and cost.

MMW sweeper component cost and suitability. Laboratory-grade MMW sweep oscillators (such as units manufactured by Hewlett-Packard, Inc., and Wiltron, Inc.) can cost as much as \$40,000 (1991 dollars) and are not particularly suited for a portable or field application. Component-type MMW sweepers (such as YIG-Tuned Oscillators [YTO] manufactured by AvanteK) are more suitable for integration into portable or field equipment and are less expensive options at \$5,000 (1991 dollars).

Complex signal processing. Since FM-CW radar signals must be transformed from the time domain to the frequency domain for analysis and display, either software or hardware Fast Fourier Transforms (FFT) must be applied to the received radar reflection signal. Considerable computer real-time overhead (on the order of several seconds per scan) is required for software FFT implementation, substantially affecting the rate of radar scan throughput. Alternatively, a hardware FFT transforms a typical radar scan in several milliseconds or less, but requires an expenditure of between \$5,000 and \$10,000 (1991 dollars) for hardware and support software.

Selected technology

Based on an examination of available radar technologies applicable to the airborne profiling of thin, fresh-water ice, an FM-CW radar system is the choice for this research project. The criteria for selection of this technology included component availability (preferably from stock), reliability, robustness, functionality and cost.

Impulse radar was eliminated as a candidate primarily because of the general unavailability of a suitably robust, readily available, field-deployable and reasonably economical wide-band pulse generator. The coded radar technique was discarded primarily because of the unavailability of logic components capable of tens of gigahertz clock rates. Synthetic pulse radar was rejected primarily because of the long single-scan dwell times (order of tens of seconds) required over a target for radar data acquisition.

An FM-CW MMW radar system can be conveniently and reliably built with readily available and reliable hardware. With MMW YTOs having a proven history of reliability in military avionics applications, they appear to be an appropriate choice for integration in a field instrument for use in a harsh (winter or Arctic)

environment. These YTOs operate at a wide temperature range (-54 to 85°C), operate directly from single polarity dc power supplies, are hermetically sealed, have a robust mechanical design and are physically small. Full K_a -bandwidth units (as well as units for other full-bandwidth microwave bands) are readily available at appropriate power levels given typical range and SNR requirements for less than \$5000 (1991 dollars). The waveguide hardware for an FM-CW radar system consists of few, simple, robust stock components that can be easily repaired or replaced in the field. Signals can be acquired and processed rapidly and continuously in real-time using readily available state of the art DSP technology. Imbedded in a field-hardened computer system, DSP hardware can immediately process and display profile survey data or store them to disk or tape for subsequent playback and analysis.

SPECIFICATIONS

FM-CW radars have been used since the early days of radar (Ridenour 1947) and Figure 15 illustrates their present day operation. As the figure shows, the output

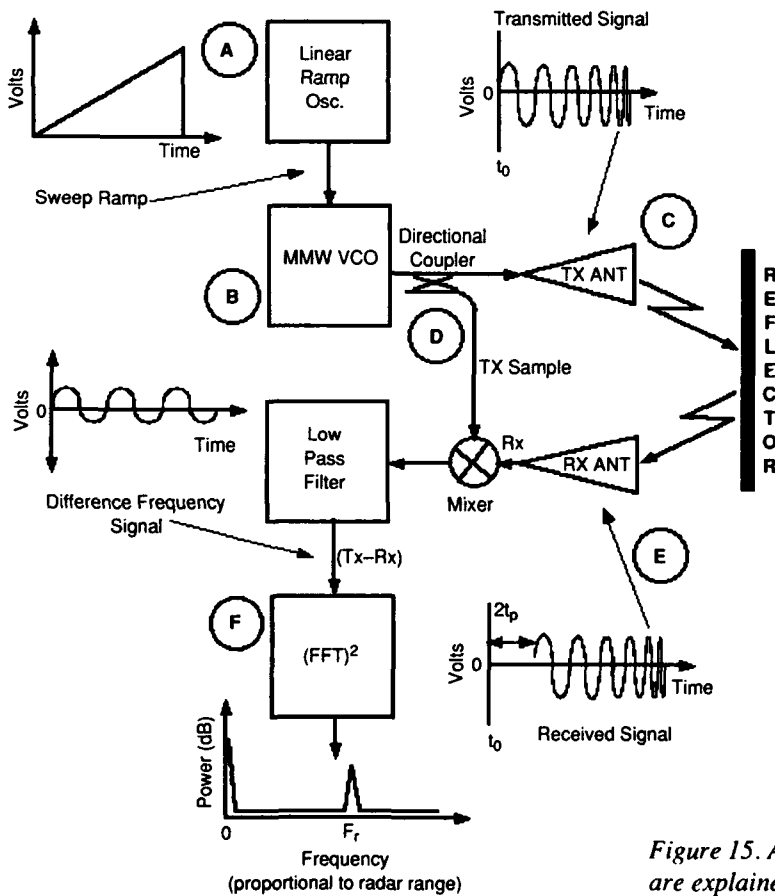


Figure 15. An FM-CW radar system (A, B, C, D and E are explained in the text).

of a linear ramp oscillator (A) is applied to the control input of the MMW Voltage Controlled Oscillator (VCO) (B), causing a linearly swept-frequency RF signal to be transmitted toward the target (C). At the same time, a sample of the swept RF oscillator output is coupled to the receiver (D). The energy received from the target, delayed by the round-trip propagation time $2t_p$ (E), is mixed with the current sample of the sweep RF oscillator output. The difference frequency F_r is proportional to the target range and can be determined using spectral analysis techniques (F). With two reflecting boundaries, as in the case of the air/ice and the ice/water interfaces, ideally there will be two distinct frequency components, one from each of the interfaces. The difference between these two frequencies is proportional to the distance between the two interfaces.

The tasks in designing an appropriate FM-CW radar to measure ice thickness continuously are to achieve the desired resolution at the necessary range, to ensure that the signal amplitude is sufficient to produce a clearly identifiable pulse after the data processing, and to implement several original processing specifications to realize the objective of rapid data interpretation.

Range and resolution

Figure 16 shows an example of a typical difference frequency time-series scan for an FM-CW radar. Figure 17 gives the Fourier transformed power spectrum of this scan, showing the spectral components that correspond to the direct coupling, first surface, second surface and multiple return events.

The one-way travel time is calibrated in terms of frequency according to the relationship

$$\text{One-way travel time (ns)} = \frac{(F_{r1}) (t_{\text{swp}})}{2(BW) (n)} \quad (29)$$

where F_{r1} = difference frequency ascribable to the air/ice interface reflection (Hz)

t_{swp} = FM-CW sweep time (s)

BW = FM-CW swept bandwidth (Hz)

n = index of refraction of appropriate medium.

Ice thickness is calibrated from the separation of the two difference frequencies according to the relationship

$$\text{Ice thickness (m)} = \frac{(F_{r2} - F_{r1}) (t_{\text{swp}}) c}{2(BW) (n_{\text{ice}})} \quad (30)$$

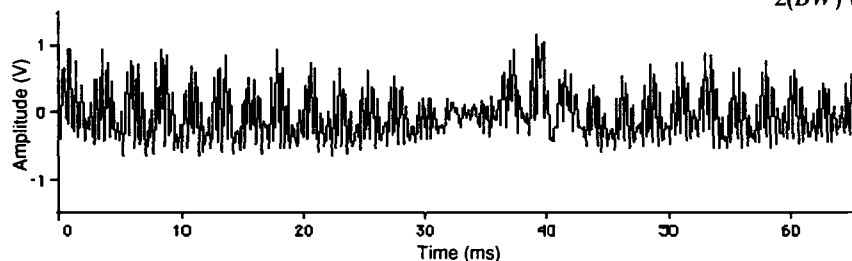


Figure 16. Typical time series scan for an FM-CW radar.

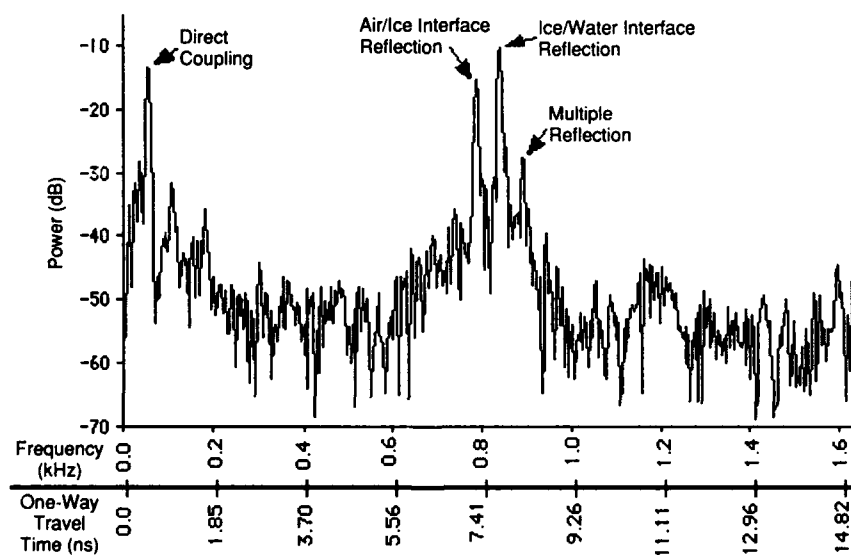


Figure 17. Typical Fourier-transformed scan for an FM-CW radar.

where F_{r2} = difference frequency attributable to the ice/water interface reflection (Hz)

n_{ice} = index of refraction of freshwater ice = 1.77
 c = velocity of light in vacuum = 3×10^8 m/s.

There is thus a trade-off between range and resolution as there is a limit on the number of time series samples that can be taken (typically 1024) during a given sweep at a set sample rate; the greater the maximum radar range, the fewer the samples that can be allocated to a small frequency segment of interest.

There are several things that one must take into account when designing a radar that affect its ability to resolve clearly the top (air/ice) surface and the bottom (ice/water) surface of an ice sheet, thereby determining the lower limit of measurable ice thickness: bandwidth, sampling, windowing, surface and volume scattering, and surface wetness.

Effect of bandwidth

Figure 18 illustrates the effect of bandwidth on resolving the radar pulse reflections from two dielectric interface boundaries. Clearly, the greater the bandwidth, the narrower the pulse shape and the easier it is to resolve closely spaced adjacent pulse maxima. The results are independent of the center frequency of the FM-CW bandwidth (i.e., 23–28 GHz yields the same resolution as 48–53 GHz).

The following calculation, as suggested by Wehner (1987), provides a *theoretical* minimum bandwidth. The minimum resolvable thickness of a dielectric slab is related to resolving two radar reflection pulses in the time domain. Under the assumption that the time domain envelope of each of two pulses is of the $\sin(\beta x)/x$

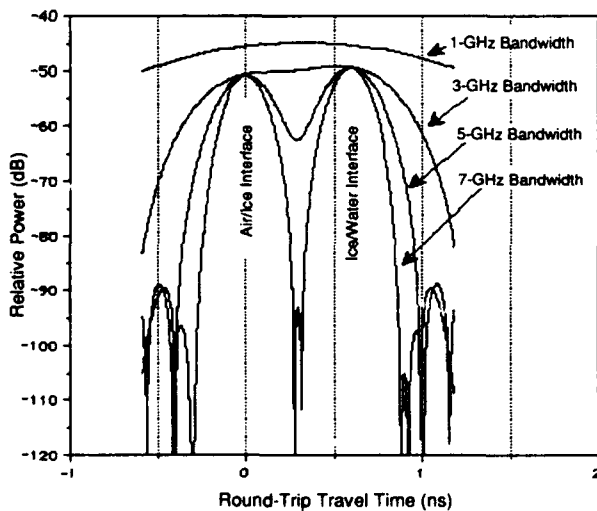


Figure 18. Effect of bandwidth on resolution of adjacent pulses (ice thickness = 5 cm).

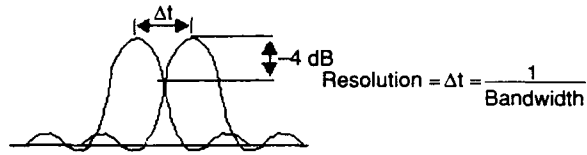


Figure 19. Minimum resolution parameters.

form, the resulting frequency domain representation is rectangular with a bandwidth BW . The minimum resolution is defined (Fig. 19) as the delay difference between these two pulses resulting in a crossover point that is -4 dB down from the pulse peaks. Then

$$BW = \frac{1}{\Delta t} \quad (31)$$

The quantity Δt is also the -4 -dB time domain maximum pulse width for resolution of top and bottom surfaces of a slab of given thickness.

With this information, the minimum required frequency bandwidth can be determined. The minimum time separation Δt between the pulse reflection off the air/ice interface and the reflection off the ice/water interface is

$$\Delta t = \frac{2s_{\min} n_{ice}}{c} \quad (32)$$

where s_{\min} is the minimum thickness of ice.

For example, given $s_{\min} = 5$ cm and $n_{ice} = 1.77$, then the pulse separation $\Delta t = 590$ ps.

Consequently, the minimum *theoretical* bandwidth, given a -4 -dB crossover, required for resolution of the thickness of 5-cm-thick freshwater ice is 1.69 GHz. If the entire K_a -bandwidth (26.5 to 40 GHz) is available, then the minimum *theoretically* measurable ice thickness is calculated to be 0.63 cm.

Effect of sampling and transformation

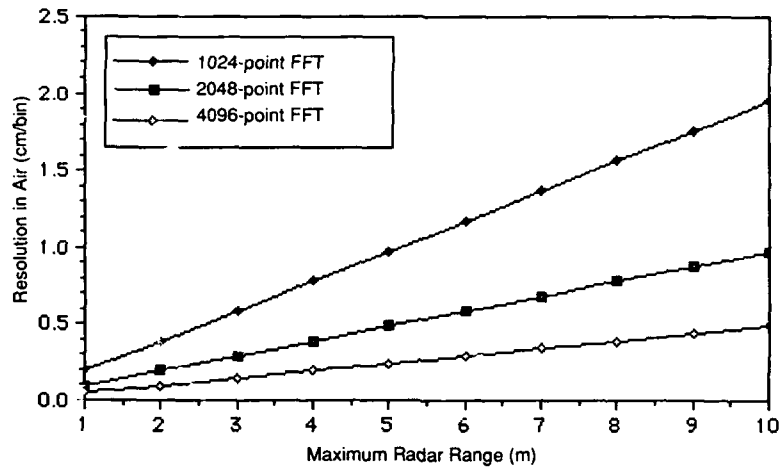
Thickness resolution is also affected by R_{\max} , the maximum radar range in free space allowed by the bandwidth, sweep time and sampling rate. R_{\max} is determined from the relationship

$$R_{\max} = \frac{(f_{sa} n_r) (t_{swp}) c}{(BW)} \quad (33)$$

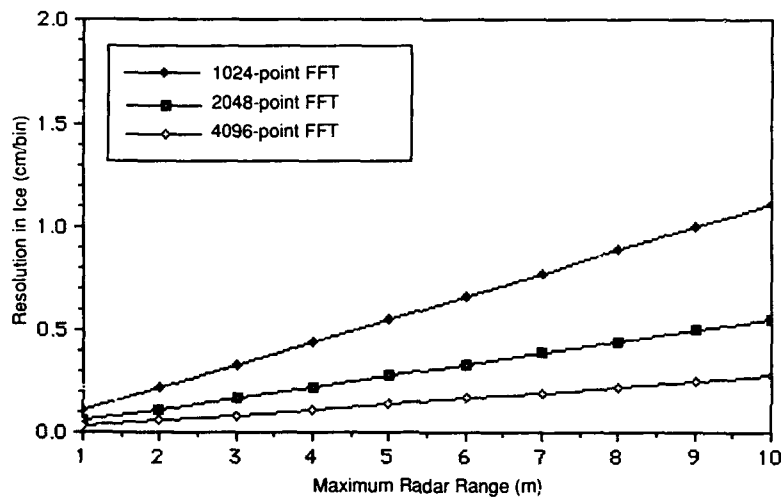
where f_{samp} is the sampling frequency (Hz).

For a given maximum radar range and FFT transform size (or number of discrete power spectrum bins) the maximum radar range resolution R_{res} can be determined by

$$R_{\text{res}} = \frac{2(R_{\max})(100)}{(N_{\text{fft}})(n_r)} \quad (34)$$



a. In air.



b. In ice.

Figure 20. Resolution as a function of maximum radar range.

where R_{res} = range resolution per bin (cm/bin)
 N_{fft} = number of points (bins) in FFT
 n_r = refractive index of medium (real part).

Figure 20 illustrates the dependency of distance resolution in free space and thickness resolution in ice on maximum range and FFT size for practical parameter values. For example, Figure 20b shows that a 2048-point FFT is required for the transform resolution to approach the minimum *theoretical* resolution calculated for a 13.5-GHz bandwidth at a maximum radar range of 5 m.

Effect of windowing

The general concept of *windowing* is explained by Oppenheim and Schaffer (1975), Stanley et al. (1984) and Kay (1988). Briefly, when a finite length segment of a time series is sampled and Fourier transformed, the abrupt beginning and end points of the sampling pro-

cess introduce spurious spectral components into the periodogram. These components appear as sidelobes that may be of sufficient magnitude to mask low level spectral components of interest. In this case, the sampled data are said to be windowed by a discrete rectangular function $w_{rect}(n)$, defined as

$$w_{rect}(n) = 1, \quad 0 \leq n \leq N-1 \quad (35)$$

where n is the sample number and N is total number of samples.

The masking effect of the sidelobes can be mitigated by convolving the sampled time series with an appropriate tapered window function, for example a discrete Hanning window $w_{Hann}(n)$, defined as

$$w_{Hann}(n) = \frac{1}{2} \left[1 - \cos \left(\frac{2\pi n}{N-1} \right) \right], \quad 0 \leq n \leq N-1. \quad (36)$$

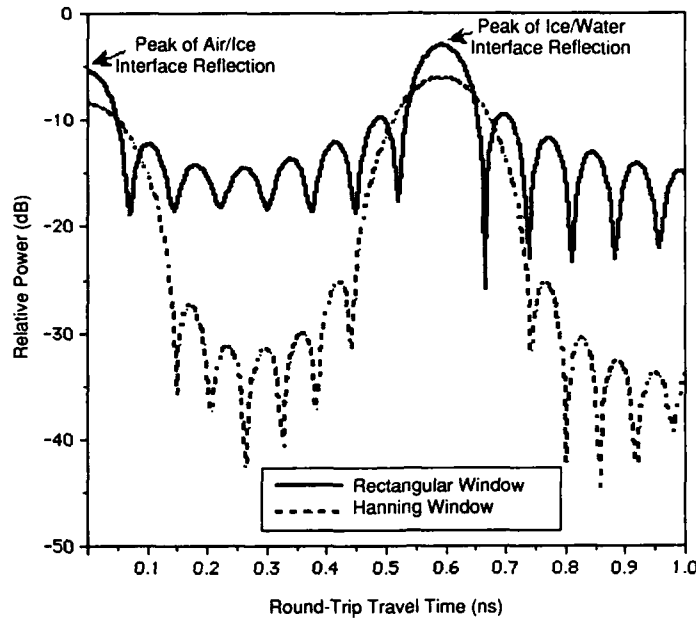


Figure 21. Pulse-widening effect of windowing.

In the time domain, a non-rectangular window, such as the Hanning, tapers the leading and trailing ends of the sampled time series to zero. After Fourier transformation the frequency domain periodogram appears smoother and with sidelobe magnitude reduced to a level as much as 30 dB less than that realizable with a rectangular window. This aids in the location of reflection artifacts that would otherwise be overwhelmed by the rectangular window sidelobe amplitude, especially when the SNR is low. There are two negative side-effects, however, as illustrated in Figure 21. First, the reflection amplitude is attenuated. In the example shown, the attenuation is 3 dB. Second, resolution is significantly limited by the widening of the pulse-width from the application of windowing. In the example shown, the -4 -dB pulse width of the rectangular-windowed data is 100 ps. When Hanning windowed, the -4 -dB pulse width is broadened to 170 ps.

Effect of sweep linearity

Deviation from a linear relationship between sweep frequency and sweep time will adversely affect the accuracy with which radar range and ice thickness can be measured. Nonlinearity of sweep NL is defined as

$$NL = \frac{\delta f}{BW} \quad (37)$$

where δf , the maximum deviation of modulation from linear, can negatively affect range resolution accuracy. Distortions in the sweep frequency vs sweep time relationship cause proportional errors in the apparent radar range of targets, by making them appear closer or far-

ther away. A typical nonlinear sweep might appear as in Figure 22.

It is desirable that range distortion attributable to nonlinearities of the sweep time/frequency relationship be significantly less than the minimum range resolution of the system. Thus, a maximum constraint on nonlinearity can be determined by requiring that NL be much less than the ratio of the minimum resolvable range R_{res} to maximum range R_{max} of the system. Given that

$$R_{res} = \frac{c}{(BW) (n_r)} \quad (38)$$

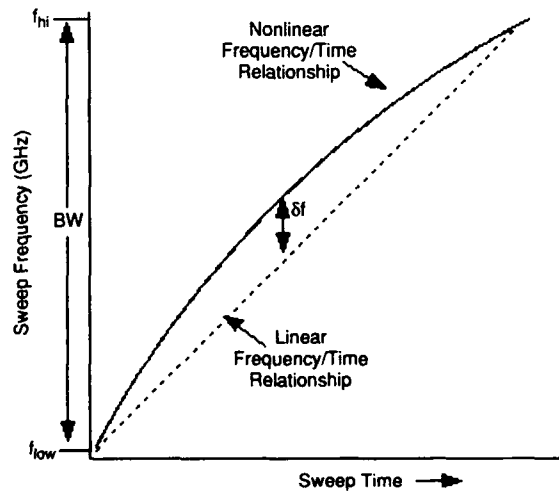


Figure 22. Parameters defining sweep linearity.

then the constraint on NL is

$$\frac{\delta f}{BW} \ll \frac{R_{res}}{R_{max}} \quad (39)$$

As an example, for a system with a 13.5-GHz swept bandwidth and a maximum range of 10 m, the minimum range resolution is 1.11 cm and the nonlinearity must be much less than 0.11%.

Bandwidth vs minimum resolvable thickness

Computer simulations were done to determine the effects of bandwidth on thickness resolution. The plane wave formulations discussed in the *Electromagnetic Propagation in Ice* section were used to simulate the reflections of a radar pulse at dielectric interface boundaries. An infinite ice sheet with smooth, parallel surfaces and no distorting effects of noise were assumed for the model. Figure 23 shows the results of one such simulation with pertinent artifacts labeled. Here, reflections from a 13.5-GHz bandwidth radar pulse are shown to resolve clearly the air/ice and ice/water interfaces of a 5-cm-thick sheet of ice floating on water. The several multiple reflections of decreasing magnitude are caused by a portion of the transmitted pulse energy reflecting back and forth between the two dielectric interfaces before returning through the air/ice interface. A Kaiser window was used in this simulation to decrease the sidelobe level.

Further simulations were conducted using the parameters shown in Table 2 and the reflection coefficients of the air/ice and the ice/water interfaces, losses in ice and focusing effects of ice on antenna beamwidth. Plane

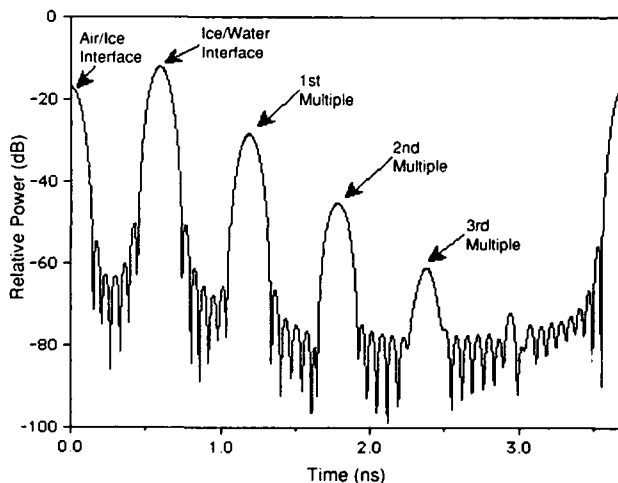


Figure 23. Computer simulation of radar reflections from a 5-cm slab of freshwater ice floating on fresh water (bandwidth = 13.5 GHz, Kaiser window coefficient = 6).

Table 2. Computer simulation parameters.

Antennas:	Standard gain pyramidal horns, 24-dB gain, 9° beamwidth
Range:	10 m
Ice thicknesses:	5, 10, 50, 100 and 200 cm
Peak transmitted power:	1 W
Transmitted waveform:	Hanning-windowed synchronized pulse
Bandwidth:	1, 3, 5 and 7 GHz
Wavelength:	1 cm (at radar center frequency in free space)
System losses:	6 dB
Receiver noise figure:	6 dB

wave reflection coefficients were used, as the beamwidth and range allows a nearly planar phase front to the waves. The separation and resolution of the air/ice and ice/water interface reflections were observed; graphical examples of outputs are shown in Figure 24.

Based on numerous iterations of the process, employing the range of practical and realizable bandwidths, peak power levels, Hanning windowing and ice thicknesses, it appears that a reasonable minimum bandwidth needed to meet the specifications is 3 GHz. At this bandwidth ice somewhat thinner than the 5-cm minimum thickness should be reliably measured using signal processing techniques (e.g., Riek 1988, Riek et al. 1990) to determine the location of the two interface reflections. This result compares favorably with the 1.69-GHz minimum *theoretical* bandwidth calculated in the *Effect of Bandwidth* section where windowing was not applied. Since Hanning windowing broadens the pulse, a greater bandwidth is required to maintain a specified thickness resolution.

Attenuation of MMW radar signals in ice

The loss component of the refractive index n_i for freshwater ice in the K_a -band, as reported in Ray (1972), is on the order of 0.001 to 0.0001. Simulations were performed to determine the effect of this loss on the reflected radar signal over a wide range of ice thickness. Figure 25 graphs the total for the bottom reflected signal for a specified set of radar parameters. The addition of 1 m of ice adds only about 1 dB of loss. Figure 26 indicates the attenuation over a range of values of n_i for a given ice thickness. These results indicate that these losses, while measurable, have little overall effect on profiling capability.

Signal-to-noise ratio

The Signal-to-Noise Ratio (SNR) is the ratio of the received power P_r to the noise present in the environment and system. Consideration of the SNR is essential when specifying system parameters for satisfactory radar performance. The system SNR is calculated to determine the feasibility of the proposed design. This SNR

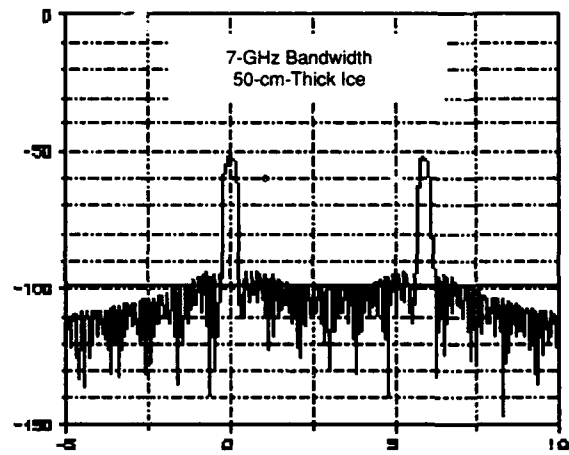
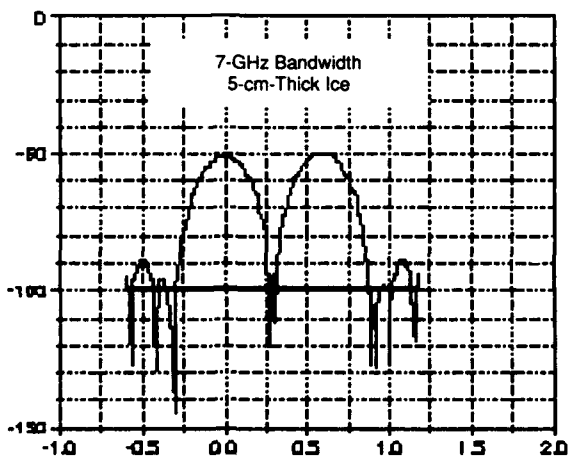
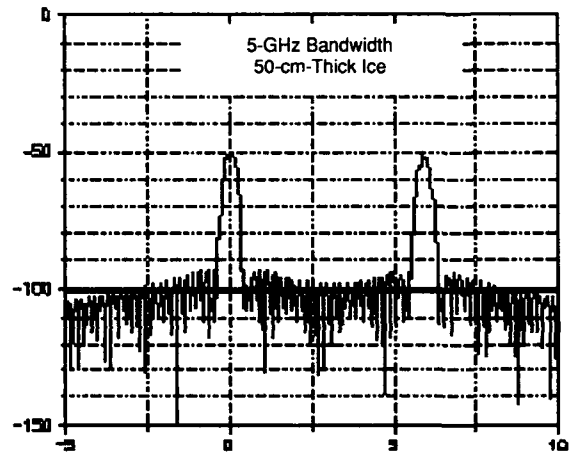
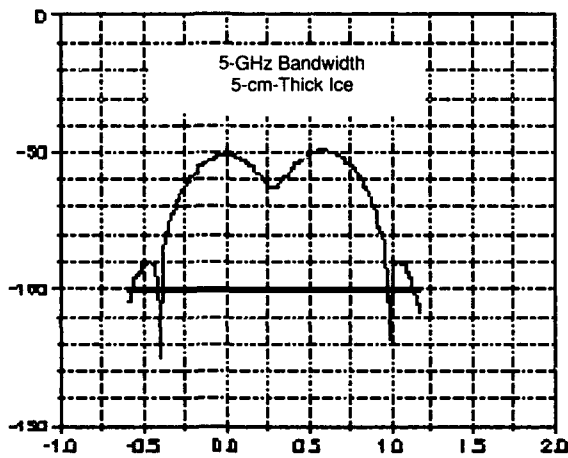
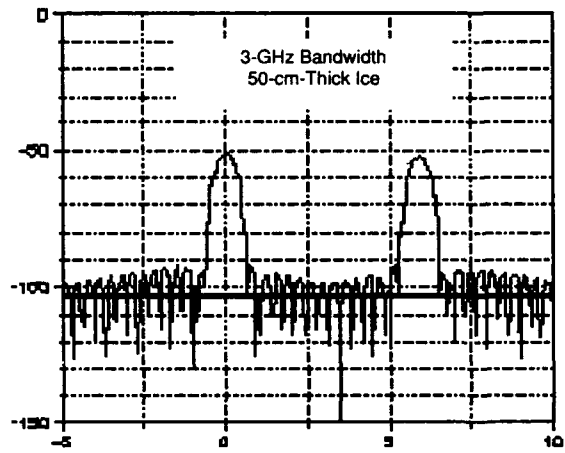
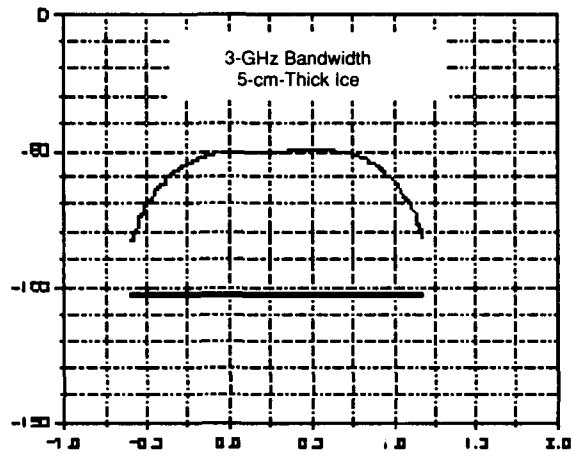


Figure 24. Example of thickness resolution simulation results. For all graphs vertical scale is relative power (dB) and horizontal scale is one-way travel time (ns). Solid horizontal line is $KT B_n$ noise power associated with given bandwidth.

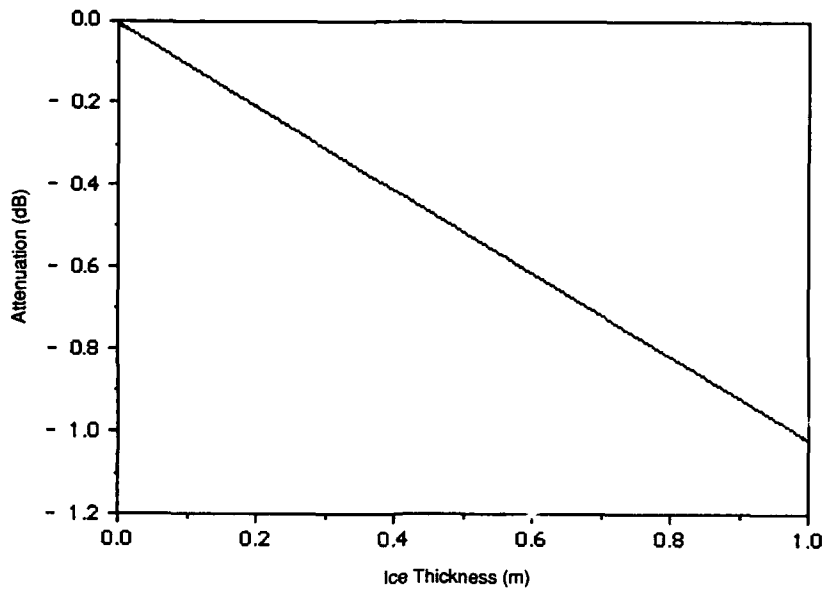


Figure 25. Attenuation vs ice thickness for $n_i = 0.0001$ (wavelength [in air] = 1 cm).

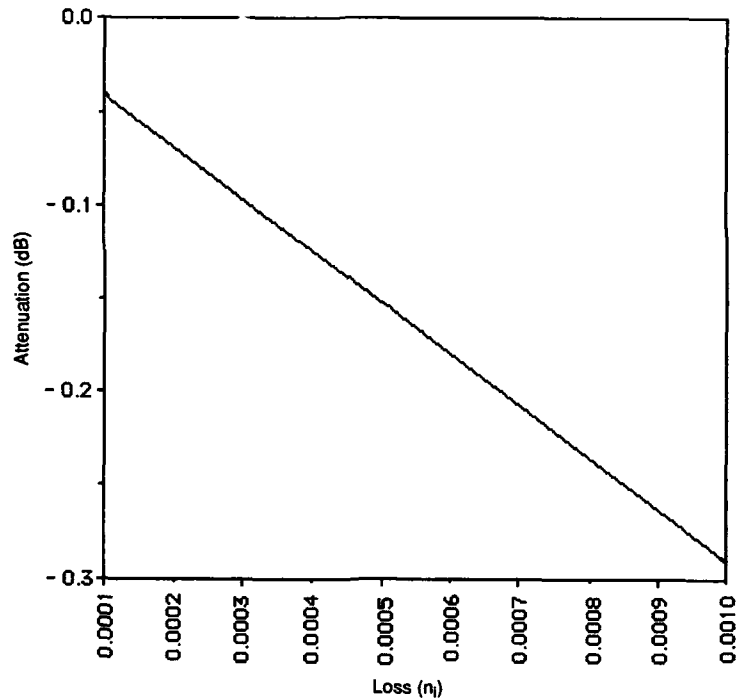


Figure 26. Attenuation vs loss factor (n_i) for a range of loss factors through a 5-cm-thick sheet of freshwater ice.

formulation is representative for a FM-CW system transformation of a single scan. If multiple pulses are stacked, a proportional increase in the SNR ratio can be obtained.

Radar range equation for geophysical application

The geophysical form of the SNR relationship was

developed from Annan and Davis (1977b), Currie and Brown (1987) and Wills (1987) and represents the SNR ratio of a radar pulse reflected from the top surface of a sheet of freshwater ice. Many of the parameters that affect the SNR were defined in eq 1.

$$SNR = \frac{P_t G_r G_t \lambda^2 L_1}{(4\pi)^2 (2R)^2 k T_o B_n F_n} (\rho_1) \quad (40)$$

where ρ_1 = reflection coefficient for first surface
 k = Boltzmann's constant (1.38×10^{-23} J/K)
 B_n = noise bandwidth
 T_o = receiver temperature (290 K)
 F_n = receiver noise figure

and

$$SNR_{dB} = 10 \log_{10}(SNR) . \quad (41)$$

The noise power term $kT_o B_n$ is shown as a function of noise bandwidth in Figure 27.

The SNR of a radar pulse reflected from the bottom surface (ice/water interface) of a sheet of freshwater ice is represented by an extension of the above relationship.

$$SNR = \frac{P_t G_r G_t \lambda^2 L_1}{(4\pi)^2 (2R)^2 k T_o B_n F_n} (\rho_2) (FC) (L_2) \quad (42)$$

where ρ_2 = reflection coefficient for two-interface medium
 FC = focus coefficient
 L_2 = medium losses due to scattering (absorption losses assumed negligible).

The viability of this approach was analyzed using realizable and specified values for these parameters as obtained from reference materials (Table 3).

1. Transmitted power P_t was assumed to be between 1 mW (1 dBm) and 100 mW (20 dBm), based on the range of output power levels available from an HP 8350B MMW sweeper source.
2. Receiver antenna gain G_r was assumed to be 24 dB from the available standard gain pyramidal horn.
3. Transmitter antenna gain G_t was assumed to be 24 dB, identical to the receiver antenna since, typically, identical horns are used for transmitting and receiving.
4. Average wavelength λ_o of the radar system (in free space) was assumed to be 1.0 cm (30 GHz).

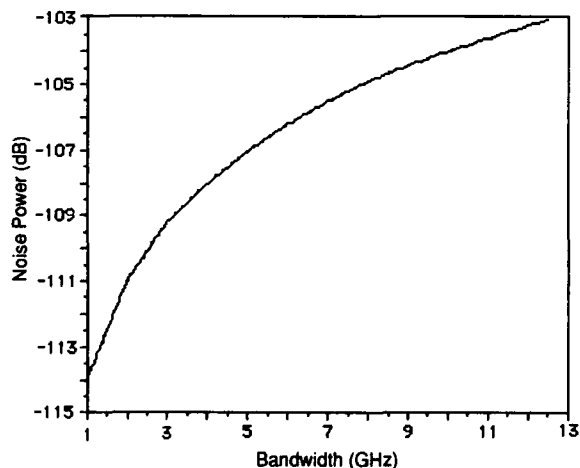


Figure 27. Noise power vs bandwidth.

5. Receiver noise bandwidth B_n was assumed to be 100 kHz. This value was selected because it is on the order of the maximum difference frequency expected at the output of the MMW mixer and input to the audio amplifier used before data acquisition.

6. Noise figure F_n is defined as

$$F_n = \frac{SNR_i}{SNR_o} \quad (43)$$

where SNR_i = signal-to-noise ratio at the input and SNR_o = signal-to-noise ratio at the output (of an amplifier, mixer or system). A typical single-ended mixer noise figure F_{mixer} is given as 10 dB by Brookner (1988). The intermediate frequency noise figure F_{if} is calculated as

$$F_{if} = 1 + \frac{P_a}{P_n} \quad (44)$$

where P_a = amplifier noise power, P_n = thermal noise power = $kT_o B_n$ and

$$F_n = F_{mixer} + F_{if} - 1 \quad (45)$$

(for a mixer with unity gain). In decibels

$$F_n(dB) = 10 \log F_n \quad (46)$$

where F_n is overall noise figure.

This figure was calculated to be -50 dB based on the specifications of an Analog Devices, Inc., AD-524 instrumentation amplifier employed as a high-gain audio amplifier used after the mixer.

7. System losses L_1 resulting from signal attenuation caused by the mixer and other waveguide and signal processing components were assumed to be 15 dB. The value chosen was significantly larger than typical values for radar systems: 7 and 6 dB seen in Currie and

Table 3. Calculation of SNR from typical system parameters.

(Worst-case L_2 would subtract an additional 30 to 40 dB from above total SNR—see text.)

P_t (dB)	10 dB _m	($P_t = 10$ mW)
G_r (dB)	24 dB _i	($G_r = 250$)
G_t (dB)	24 dB _i	($G_t = 250$)
F_n (dB)	-50 dB	
L_1 (dB)	-15 dB	
B_n (dB)	-50 dB	($B_n = 100$ kHz)
$2R^2$ (dB)	-20 dB	($R = 5$ m)
λ^2 (dB)	-40 dB _{sm}	($\lambda = 0.01$ m)
ρ (dB)	-5.6 dB	($\rho = 0.28$ for air/ice)
$(4\pi)^2 k T_o$ (dB)	182 dB	
Total SNR	59.4 dB	

Brown (1987) and in Brookner (1988) respectively. It was selected as a worst-case estimate to account for practical levels of system losses and for any unforeseen losses that may be present in the design.

8. Range R represents the distance from radar antenna to the ice surface. A value of 5 m was assumed since it represents the typical measurement range employed in references cited earlier.

9. Losses L_2 represent propagation losses that can be ascribed to random processes, i.e., surface and volume scattering. It is expected that surface scattering will be the dominant factor, and that there will be a sufficiently strong specular reflection from normally oriented smooth-surfaced facets for a wide range of surface roughnesses. While the degree to which medium losses negatively affect the SNR of the system is currently unknown, it is expected that scan-to-scan variations in the magnitude of L_2 may range as much as 30 to 40 dB (Ulaby and Whitt 1988). Jezek et al. (1991) show theoretically significant coherent returns from a surface characterized by a ratio of rms surface roughness to wavelength over a range of at least 0.0033 to 0.1667. Therefore, the system needs only have sufficient absolute SNR to make top and bottom surface returns apparent. For example, if the radar system has a 60-dB absolute SNR, then in the worst-case situation where the signal returns are scatter-attenuated by as much as 40 dB, they would still be clearly apparent, 20 dB above the noise floor. Additionally, since the magnitude of the returns are statistically described by a Gaussian or Rayleigh distribution (Ulaby and Whitt 1988, Jezek et al. 1991), it can be expected that, while not every scan provides a discernible return, a sufficient percentage of the scans in a continuous profile will include coherent reflections significantly above the system noise floor and provide a reasonably detailed ice profile.

Converting the radar range equation (eq 40) to the decibel form, we obtain

$$SNR_{(dB)} = \left[P_{t(dB)} + G_{r(dB)} + G_{t(dB)} + \lambda_{(dB)}^2 + P_{(dB)} \right] - \left[(4\pi)^2 k T_{\alpha(dB)} + L_{1(dB)} + (2R)_{(dB)}^2 + B_{n(dB)} + F_{n(dB)} \right]. \quad (47)$$

Given the SNR formulation and the assumed values of the parameters, the results in Table 4 have been developed.

Other signal and noise-related parameters

Several additional quantities that describe the performance of a radar can be derived from signal and noise power. These include noise figure, dynamic range and performance figure.

Table 4. Typical transmitted power levels and related SNR for given system parameters.

P_t (W)	P_t (dBm)	SNR (dB)
0.001	0	49.4
0.01	10	59.4
0.10	20	69.4

Dynamic range. The dynamic range is the difference between the smallest detectable signal level (typically at the noise power P_n [dB] level) and the largest nonsaturating detectable signal level (as from a close or large target) that can be viewed or recorded during one scan.

For a 13.5-GHz bandwidth, $P_n = kTB_n = -103$ dBm. For a typical MMW mixer with a 20-dB gain, approximately -20 dBm appears to be the input power level to cause saturation. This results in a dynamic range of 83 dB.

Performance figure. The performance figure of the radar system is defined as the difference between the power at the output of the transmitting antenna (dB) and the smallest detectable signal level (typically at the noise power P_n [dB] level).

For a 13.5-GHz bandwidth, $P_n = kTB_n = -103$ dBm. With a 10-mW (10-dBm), average transmitter output and a 24-dB gain antenna, the effective power at the output of the antenna is 34 dB. The performance figure is then 137 dB.

External coherent noise

Extraneous radar returns from man-made and natural structures that interfere with interpretation of desired radar return are classified as sources of external coherent noise. This is of little concern, given the narrow beamwidth of the radar antennas and distance from typical sources such as power lines, bridges, docks and buildings encountered during airborne profiling surveys of lakes and rivers. Coherent returns from the helicopter itself are not a problem since the narrow-beam radar antennas are mounted away from interfering structures. Additionally, the propagation time for a coherent reflection directly from the helicopter is significantly less than the round-trip travel time from antenna to the surface of the ice. A coherent return caused by multiple reflections from the ice sheet and aircraft structure undergoes a greater round-trip travel time and is more greatly attenuated by geometric spreading than a reflection returning directly from the ice sheet.

Data acquisition and recording

There is a direct interaction between data acquisition

and recording parameters, and sweep time, sweep rate and radar range. Here, these effects are defined and examined. Specifications are determined that provide an optimal compromise between available technology and desired system capability

The time required to frequency modulate the sweeper linearly from the lower to upper band limits once is defined as the sweep time (Fig. 28) The full K_a -bandwidth sweep time of the HP 8350B MMW source is adjustable from 0.01 to 100 seconds. Recovery time (Fig. 28) is defined as the duration between linear frequency-modulated sweeps. The sweep rate is the number of full band frequency sweeps per unit time. Sweep rate, recovery time and sweep time are related to the sweep frequency f_{swp} by

$$f_{swp} = \frac{1}{\text{sweep rate}} = \frac{1}{(t_{swp} + t_{rec})} \quad (48)$$

where f_{swp} = sweep frequency (Hz)
 t_{swp} = sweep time (s)
 t_{rec} = recovery time (s).

The sweep duty-cycle is the percent of time of a sweep cycle that the oscillator is linearly sweeping between the upper and lower limits of the frequency band and is defined as

$$\text{Duty cycle (\%)} = \frac{(t_{swp})(100)}{(t_{swp} + t_{rec})} = (t_{swp})(f_{swp})(100). \quad (49)$$

It shall be shown later that sweep duty-cycle, when related to parameters including ground speed, antenna height and beamwidth, is useful in determining the percentage of antenna beam footprint overlap or the gap in surface coverage between successive radar scans.

Sweep rate vs FM-CW signal frequency

The radar difference frequency is related to several system parameters, as discussed earlier. The equation

relating these parameters can be rewritten to determine the resulting maximum difference frequency component. For reliable measurements, it is necessary that the highest possible radar difference frequency for a given set of system parameters be within the capabilities of data acquisition sampling rate and data recorder bandwidth.

For the first surface (air/ice interface), the radar difference frequency F_{r1} is determined from

$$F_{r1} = \frac{2(R)(BW)(n_o)}{(t_{swp})(c)}. \quad (50)$$

For the second surface (ice/water interface), the difference frequency F_{r2} is determined from

$$F_{r2} = \frac{2(R)(BW)(n_o)}{(t_{swp})(c)} + \frac{2(s)(BW)(n_{ice})}{(t_{swp})(c)}$$

or

$$F_{r2} = \frac{2(BW)}{(t_{swp})(c)} \cdot [R(n_o) + s(n_{ice})]. \quad (51)$$

Since $F_{r1} < F_{r2}$, the data acquisition system must be capable of a bandwidth greater than F_{r2} . Since the data acquisition sampling rate and recorder bandwidth are limited, given available technology, accommodations must be made by adjusting other system parameters. Figure 29 illustrates the relationship between sweep rate and radar difference frequency for various radar ranges. Maximum bandwidths of available data processing and storage technologies are also shown, bounding the practical limits of sweep rate and maximum radar difference frequency. A typical Digital Signal Processing Analog-to-Digital Converter (DSP ADC) capable of acquiring, processing and displaying radar difference frequency data has a maximum sample rate of 128 kHz. A typical Digital Audio Tape recorder (DAT) useful for recording and long-term storage of radar difference frequency data has a maximum sample rate of 40 kHz. For example, given a maximum radar

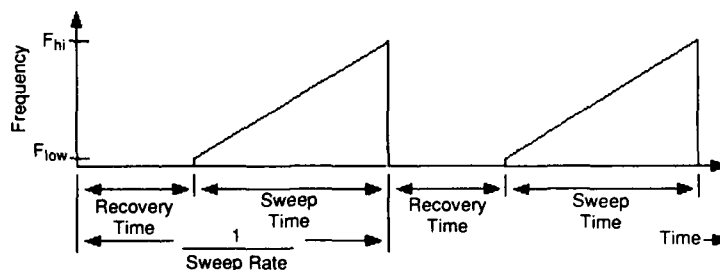


Figure 28. Sweep time and sweep rate parameters.

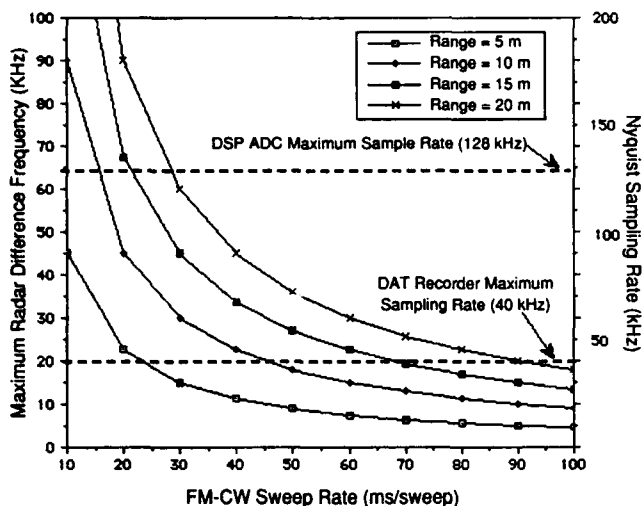


Figure 29. FM-CW radar difference frequency vs sweep rate for various radar ranges (sweep bandwidth = 13.5 GHz).

range of 10 m and the maximum radar difference frequency of 20 kHz (the maximum bandwidth at the DAT sample rate of 40 kHz), the fastest sweep rate possible is approximately 45 ms/sweep. With an analog tape recorder, having a 5-kHz bandwidth, for example, a sweep rate of 100 ms/sweep at a range of 5 m would be an acceptable combination.

Selection of optimal sweep time

Most data acquisition hardware is designed with a limited selection of sampling frequencies derived using hardware frequency division techniques from an internal, fixed-frequency crystal oscillator clock. Available DSP hardware is typically capable of performing FFTs based on power-of-two (e.g., 512, 1024, 2048, etc.) multiple time samples per scan. To assure that advantage is taken of the full available radar bandwidth, it is necessary to completely sample the difference frequency time series output of the radar over the entire sweep time. Sampling over less than the entire sweep time translates into a proportional decrease in the available radar bandwidth and, thereby, resolution. Since the choices for the number of samples per scan and the sample rate are limited by hardware constraints, the FM-CW sweep time t_{swp} must be adjusted to fulfill the following relationship

$$t_{\text{swp}} = \frac{n_{\text{samp}}}{f_{\text{samp}}} \quad (52)$$

where n_{samp} = number of samples per scan and f_{samp} = sampling frequency (Hz).

Using eq 52, Table 5 documents the sweep times allowed for the available sampling frequencies for a

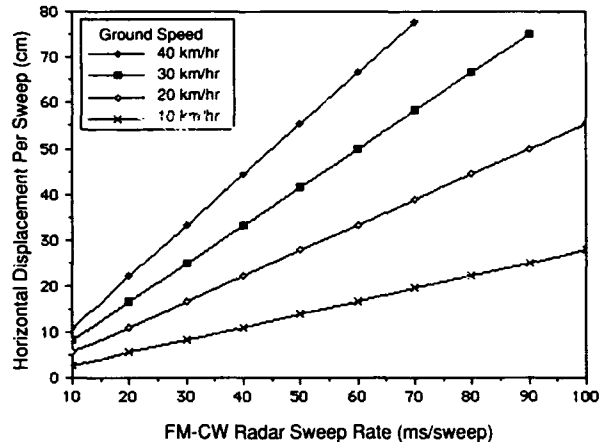


Figure 30. Horizontal displacement per sweep vs sweep rate for a range of typical profiling ground speeds.

MacDSP256KNI DSP ADC board (Spectral Innovations, Inc.). Here, the sampling frequencies f_{samp} and the samples per scan n_{samp} are fixed by the DSP ADC board hardware and software configuration. For example, for $f_{\text{samp}} = 15.62$ and $n_{\text{samp}} = 1024$, $t_{\text{swp}} = 0.66$ seconds.

Profiling speed and sweep rate

When the radar is in motion, a certain amount of ground will be covered during a single scan, the duration of which is determined by the sweep rate. Figure 30 indicates the effect of profiling speed upon the dependency of horizontal antenna displacement on sweep rate. For example, a helicopter flying at 30 km/hr carrying a radar system with a sweep time of 66 ms would undergo a horizontal displacement of approximately 55 cm during each scan. The relationship of ground speed and sweep rate to the amount of antenna footprint overlap between adjacent scans and the ability of the radar to discern abrupt changes in the ice thickness or surface roughness is explained in the *Antenna Ground Footprint and Overlap* section.

Table 5. Selection of optimum sweep times.

Based on samples per scan n_{samp} and sampling frequency f_{samp} of a Spectral Innovations MacDSP256KNI DSP ADC board.

Samples per scan, n_{samp}	Sweep time (s)			
	Sampling frequency, f_{samp} (kHz):			
	3.91	7.81	15.62	31.25
1024	0.262	0.131	0.066	0.033
2048	0.524	0.262	0.131	0.066
4096	1.048	0.524	0.262	0.131

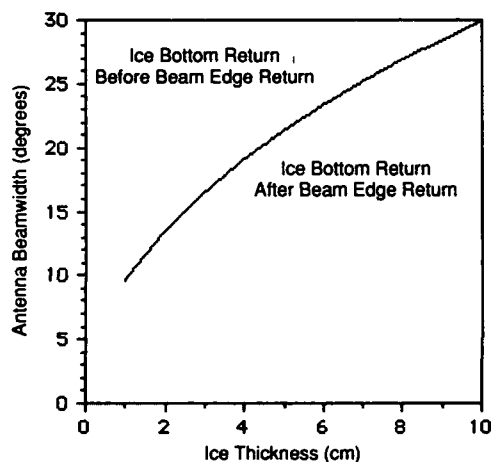
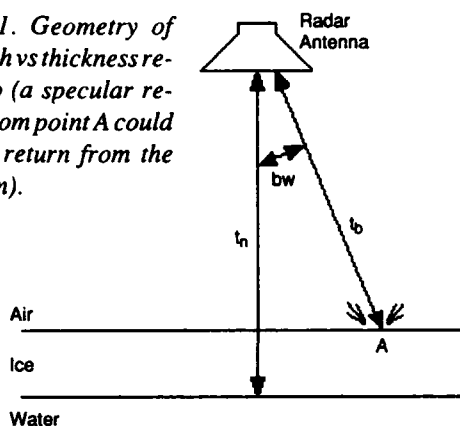
Antenna parameters

The antenna configuration affects the size of the radar footprint on the ice sheet, the bandwidth of the transmitted and received radar signal, the effective radiated power of the signal, the gain of the received signal, and the effects of sidelobe interference on the top and bottom surface returns. Standard gain horn antennas appear to have sufficient bandwidth for this application. However, beamwidth and phase error across the aperture may be a limiting factor on minimum thickness resolution.

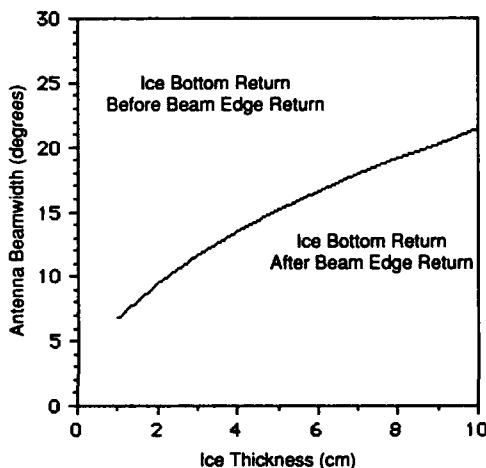
Antenna beamwidth and ice thickness

A relationship exists between antenna beamwidth and the thickness of the measured ice that may lead to

Figure 31. Geometry of beamwidth vs thickness relationship (a specular reflection from point A could mask the return from the ice bottom).



a. Range = 5 cm.



b. Range = 10 m.

Figure 32. Antenna beamwidth as a function of ice thickness for reflections from the ice/water interface and air/ice interface at beam pattern edge to coincide at ranges of 5 and 10 m.

ambiguous or confusing results. The confusion would result from the propagation delay from an ice surface specular reflector at the edge of an antenna footprint t_b being comparable to the propagation delay from the reflection at the ice bottom surface t_n (Fig. 31). Ideally, the return from the ice/water interface should distinctly occur after any possible returns from the air/ice interface, that is

$$t_b < t_n. \quad (53)$$

Figure 32 indicates that, to limit reflection ambiguity, a narrower beamwidth is preferable. The 9° standard gain horn antennas satisfy this condition for ice thickness of as little as 1 cm for radar ranges greater than 5 m. Figure 33 illustrates the beam geometry of the 9°

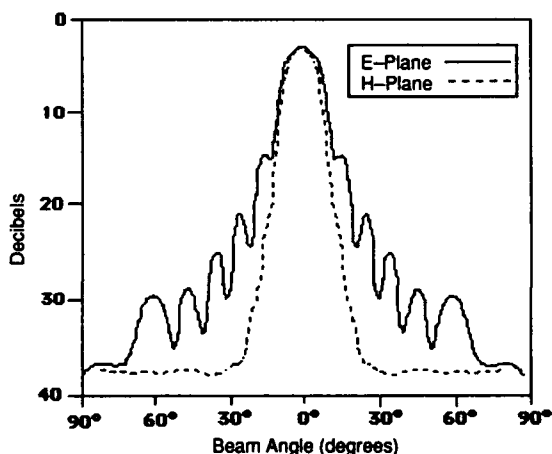


Figure 33. Beam geometry of standard gain 9° antenna.

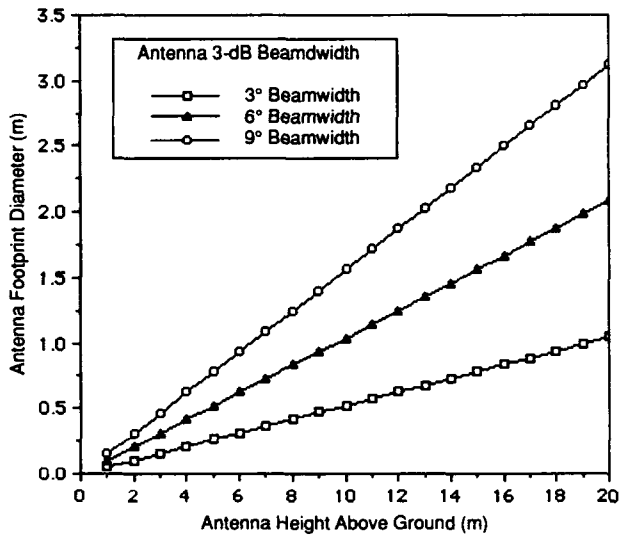


Figure 34. Footprint diameter for 3-dB antenna beamwidths vs altitude.

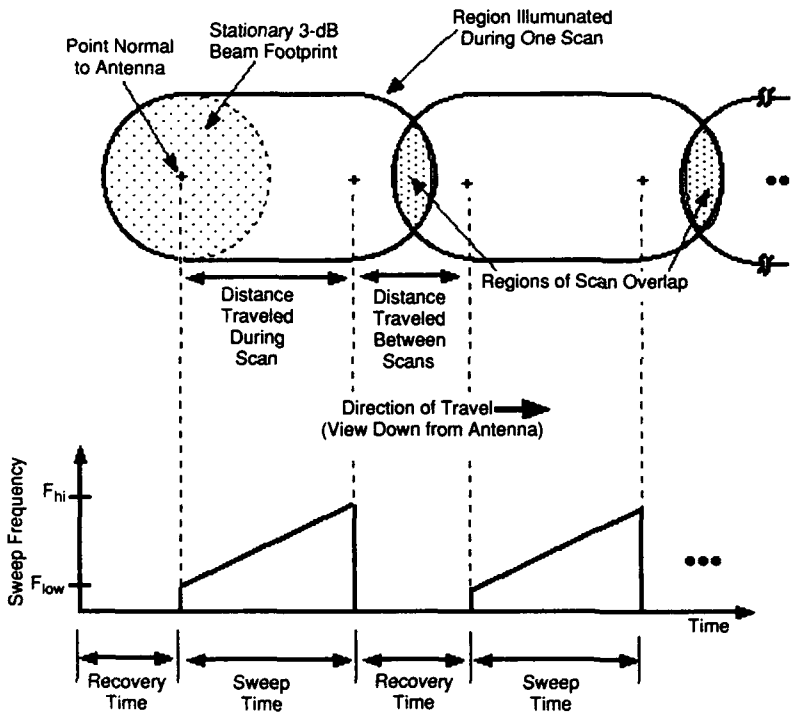


Figure 35. Parameters for determining antenna footprint overlap, relating antenna footprint dimensions to FM-CW sweep signal.

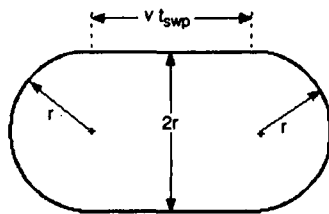


Figure 36. Dimensions of area illuminated by one scan.

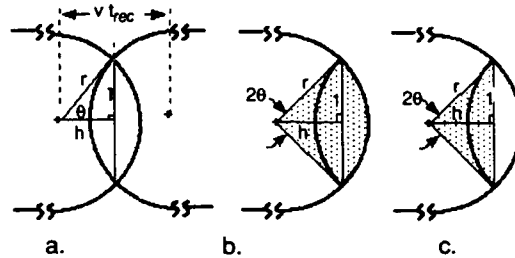


Figure 37. Geometric elements for calculating percent overlap of antenna footprint on adjacent scans.

standard gain horn antenna. Narrower beamwidths are achieved only with a large increase in cost and physical dimension (dielectric lens horns or parabolic dishes).

Antenna ground footprint and overlap

Figure 34 illustrates the footprint diameter for several antenna 3-dB beamwidths over a range of radar profiling altitudes. For example, a 9° beamwidth horn at an altitude of 10 m gives a 3-dB main lobe footprint approximately 1.5 m in diameter. The footprint, when considered with profiling ground speed and sweep rate, determines the degree of footprint overlap, and hence, physical averaging of sequential profiling scans. The percentage of overlap area between sequential scans is a function of antenna beamwidth, survey altitude and sweep duty-cycle in addition to sweep rate and survey vehicle speed. Figure 35 illustrates the physical relationship among these parameters. Here, for a given ground speed and antenna altitude, the ice surface area illuminated by the antenna's 3-dB main lobe pattern is illustrated in relation to the sweep and recovery times of the FM-CW MMW oscillator.

The percentage of overlapping area of adjacent scans as shown in Figure 35 is calculated by determining the 3-dB beamwidth area illuminated during one scan. Figure 36 illustrates the parameters necessary for this calculation. The radius r (in meters) of the footprint depends upon antenna altitude and antenna beamwidth, and can be determined from Figure 34 or by the relationship

$$r = R \tan\left(\frac{\phi}{2}\right) \quad (54)$$

where R is range to surface of the ice (m) and ϕ is antenna beamwidth ($^\circ$). Then, the area illuminated A_{illum} (m^2) during one scan is determined from

$$A_{\text{illum}} = \pi r^2 + 2rvt_{\text{swp}} \quad (55)$$

where v = ground speed (m/s) and t_{swp} = sweep time (s).

The area (m^2) of scan overlap and the percent of overlap between adjacent scans can be determined using geometrical relationships illustrated in Figure 37a. The distance h , one half of the distance covered during the sweep recovery time, is calculated as

$$h = \frac{(v t_{\text{rec}})}{2} \quad (56)$$

where t_{rec} = recovery time between sweeps (s). Then,

$$\theta = \cos^{-1}\left(\frac{h}{r}\right) \quad (57)$$

and

$$l = r \sin(\theta). \quad (58)$$

The area of the wedge A_{wedge} (shaded area in Fig. 37b) is calculated as

$$A_{\text{wedge}} = \frac{2\theta}{360} (\pi r^2) \quad (59)$$

and the area of the triangle A_{tri} (shaded area in Fig. 37c) is calculated as

$$A_{\text{tri}} = hl. \quad (60)$$

Thus, area of scan overlap A_{ovlp} is

$$A_{\text{ovlp}} = A_{\text{wedge}} - A_{\text{tri}} \quad (61)$$

and the percentage of area overlapping between scans is

$$\text{Overlap (\%)} = \left(\frac{A_{\text{ovlp}}}{A_{\text{illum}}}\right) (100). \quad (62)$$

If, however

$$2r > vt_{\text{rec}} \quad (63)$$

then, instead of an overlap, there would be a spatial gap Gap (in meters), in coverage between adjacent scans where

$$Gap = 2r - vt_{\text{rec}}. \quad (64)$$

Figure 38, generated from these equations, illustrates the percentage of overlapping area of adjacent radar scans for several radar ranges as a function of ground speed and other parameters, as specified.

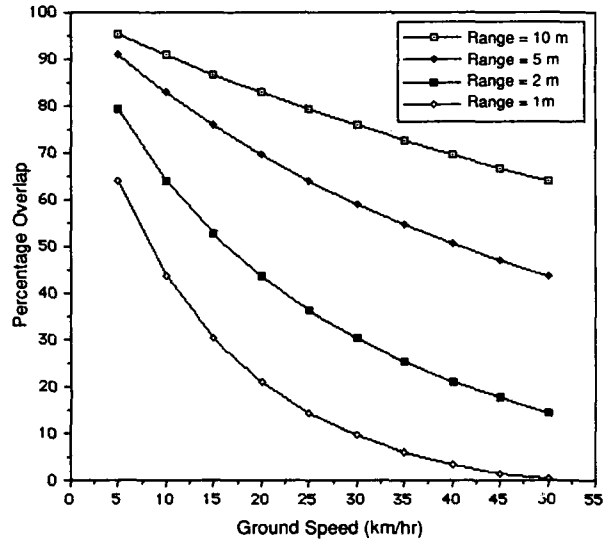


Figure 38. Percentage of 3-dB antenna beamwidth overlap as a function of ground speed, altitude, sweep rate and duty cycle (antenna beamwidth = 9° , sweep rate = 0.066 s and duty-cycle = 75%).

For example, a survey vehicle traveling 5 m above the ground at 25 km/hr with a 0.066-s sweep rate and a 75% sweep duty-cycle would have an adjacent scan antenna footprint area overlap of 65%.

Physical parameters

Physically, the system is constrained by the way it is to be used. Weight, physical dimension, deployment mode and operational environment influence the system's configuration.

Weight

As this radar package is intended to be operated from on-board a small helicopter (e.g., Bell Jet Ranger 206B), it is necessary that the weight be limited. The typical aircraft used for radar profiling purposes can transport a pilot, three passengers and limited additional payload. Therefore, total weight should be no more than the equivalent of one passenger, approximately 90 kg (200 lb). Also, the system should be made into modular components that can be easily carried by one or two people.

Dimensions

Because the system must be field-transportable, and space available on-board the survey helicopter is limited, it, less power supply and antennas, should occupy a space of no more than 0.25 m³ (8 ft³). Additionally, modules should be dimensioned for convenient shipping in containers, and for easy transport by personal or common carrier to the field site.

Operating power

Both the constraints of field and airborne operation require that the system use a minimum of electrical power. Typical aircraft suitable for profiling have an on-board 24- to 28-Vdc source capable of delivering 50 to 75 A. The supply of 115 V rms at 60 Hz is limited to approximately 2 A (if available at all). Therefore, the radar is designed to require less than the available on-board power or to use an independent battery to supply part or all required power.

Antenna attitude

Antenna attitude must be maintained to nadir or near-nadir pointing. The degree to which off-nadir look-angle can be tolerated is a function of antenna beamwidth. In the case of the 9° beamwidth standard gain antennas used in the prototype, experience indicates that an off-nadir look-angle of ±5° has minimal effect.

Operational temperature

The radar has to operate at 0°C or less, given the intended field environment and the typical temperatures at which helicopters are used.

Operational humidity

The system should operate in a noncondensing, 5 to 95% relative humidity environment. This is typical for helicopters.

Operational altitude

The system should work over frozen bodies of water located at altitudes up to at least 4600 m (15,000 ft) above sea level, permitting surveys at the majority of locations of interest on earth. This is within the typical operational range for helicopters.

Vibration levels

All radar components should be capable of withstanding the normal range of vibrations and g-shock associated with being used in the field and aboard helicopters. This especially applies to rotating memory devices, which may be particularly vulnerable.

Summary of specifications

The system specifications, as previously defined, are summarized in Table 6.

Table 6. FM-CW MMW radar specification summary.

Measurement parameters	
Range (height above surface)	3 to 10 m
Measurement speed	> 20 km/hr
Ice thickness	> 5 to 182 cm
Resolution	> ±10%
System parameters	
Output power	< 20 dBm (continuous)
Modulation type	FM-CW
Sweep rate	15 scans/s (nominal)
DSP processing time	2 ms (1024 pt. real FFT)
Bandwidth	13.5 GHz (full K _a -band)
Center frequency	33.3 GHz
Receiver SNR	> 60 dB
Receiver noise figure	< 6 dB
Receiver dynamic range	83 dB
Receiver performance figure	137 dB
Receiver noise floor	-103 dB
Antenna beamwidth (3 dB)	9°
Antenna gain	> 24 dB (Tx and Rx, each)
Output modes	
DSP video display	Time/frequency domain displays
DAT tape storage	For analysis and archiving
Removable/fixd disk storage	For analysis and archiving
Physical parameters	
System weight	< 90 kg
System dimensions	< 0.25 m ³
Antenna dimensions	< 0.03 m ³
Antenna attitude	Normal to surface
Minimum operating temperature	< 0°C
Humidity range	5 to 95% non-condensing
Altitude (maximum)	4600 m

DESIGN AND CONSTRUCTION

Prototype system configuration

The prototype system was built to best meet our specifications, given available hardware and software resources. It (Fig. 39) consists of a computer (Macintosh II) containing a data acquisition/Digital Signal Processing (DSP) board (Spectral Innovations, Inc., MacDSP256KC), an MMW sweeper (HP 8350B), an analog tape recorder (HP 3964A), audio amplification and scan synchronization electronics, a homodyne receiver constructed from assorted MMW waveguide components, and two standard gain (24-dB) pyramidal horn antennas of 9° beamwidth. Prior to the availability of computer and data processing hardware necessary for the prototype, a pre-prototype was assembled using components that were currently on hand in laboratory inventory. This system used an 80286-SX, 16-MHz, DOS-based computer with a 80287 math coprocessor, data acquisition board, an HP 8350B MMW sweeper, a homodyne receiver constructed from assorted MMW waveguide components, and the two standard gain (24-dB) horn antennas. Processing time with this configuration was unacceptably lengthy, requiring approximately 5 to 10 seconds per scan. This system was used to acquire and process ice profiling scan data as described in the *Skating Arena Profile* section and Appendix A.

The prototype is made from standard off-the-shelf hardware, with the exception of the high-gain instrumentation amplifier and synchronizer electronics, which were designed specifically for this. The amplifier boosts the millivolt-level difference frequency voltage from

the receiver to an appropriate level for data acquisition and processing. Synchronization for framing radar scan data is taken from the "Positive Z-Blank" signal provided by the sweeper and interfaced to a two-channel analog multiplexer that inserts a start-of-frame pulse into the data stream prior to the beginning of each radar scan. Scan data acquisition and processing by the DSP board are triggered by level and slope transition of this intra-data stream pulse. For this series of tests, the system was powered by electric line or gasoline generator, whichever was more convenient at the test site.

The prototype FM-CW MMW can sweep the full 13.5-GHz K_a -band, 26.5 to 40 GHz, at a rate of up to 100 scans per second. But, because of analog data recorder bandwidth limitations (5 kHz), a maximum sweep rate of 20 scans per second has been employed in measurements to date. Data acquisition at rates of up to 128 kilosamples per second are possible with dedicated digital signal processing hardware that also offers windowing, 1024 (or more) point FFTs, block averaging and waterfall or spectrographic display. Sweeper power levels of up to 15 dBm, with a sweep linearity of better than 0.05%, are attainable. The maximum operating range has been shown to be on the order of 10 m, with an SNR in excess of 30 dB. Simulations indicate that accurate measurement of freshwater ice in excess of 200 cm thick is feasible.

The system is designed to acquire and process data in real-time or to record only. Data recorded to tape in either mode can be processed later as they are played back. The various modes of operation are explained later.

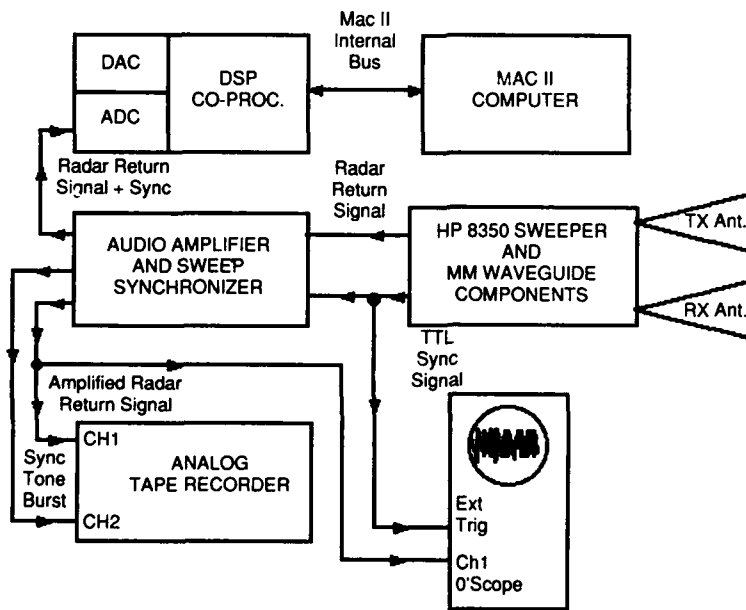


Figure 39. Block diagram of the MMW FM-CW radar (configured for real-time data acquisition and processing).

MMW source

There were two commercial options available for the MMW source: an HP 8350B series MMW source and an Avantek (YTO) YIG-tuned oscillator (AVO-26xxx M/W series). In terms of price, physical dimensions and performance, the Avantek unit is more desirable. However, owing to long lead times (more than 20 weeks) for the Avantek unit and the immediate in-house availability of an HP 8350B sweeper, the latter was chosen. Subsequent versions of the system will use the smaller, less expensive YTO.

The prototype employs an HP 8350B sweep generator with an HP 83550B RF plug-in unit and an HP 83554A MMW source module. As configured, this MMW source is capable of sweeping the full K_a -band (26.5 to 40 GHz), with a sweep time of 0.01 to 100 seconds at a leveled power output of up to 15 dBm, and a sweep linearity of less than 0.05%. The unit requires 3.25 A at 117 Vac and 60 Hz for operation.

Radar front-end

The radar front-end module (Fig. 40), performing both the transmitting and receiving functions, consists of a homodyne mixer fabricated with a waveguide crystal detector diode (HP R422C), two -20-dB waveguide directional couplers (HP R752D), and two like-polarized, co-located, 26-dB standard gain pyramidal horn antennas (Scientific Atlanta 12A-26).

The theory of homodyne mixing is described in detail by King (1978) and applied to FM-CW radar by Gubler and Hiller (1984). It entails the continuous mixing of a sample of the MMW sweeper output with the MMW signal reflected from a target without any intermediate frequency translations. This front-end design provides an adequate SNR for this application and can be conveniently, economically and robustly implemented.

The central elements of the front end are two -20-dB waveguide directional couplers with a connection between sampling ports. The through-connection of the transmit waveguide coupler is attached between the

MMW sweeper source and the transmit antenna. The through-connection of the receive waveguide coupler is attached between the receive antenna and a waveguide-mounted detector diode. A sample of the transmitted sweep signal and the received signal propagate down the receive coupler waveguide and are mixed by the detector diode acting as a single-ended mixer. Single-ended MMW waveguide mixers typically have an approximately 10-dB noise figure, according to Currie and Brown (1987). Substitution of a low-noise, broadband-balanced MMW mixer in place of the diode detector single-ended mixer can result in as much as 3 dB of SNR improvement. Economics and in-house availability prevailed in the choice of the diode detector.

Antenna parameters

The physical dimensions of the antennas are of practical concern for reasons of portability, convenience and safety of external helicopter mounting. Since this system is intended for airborne application, wind-loading and aerodynamic drag may also be of concern. The commonly available horn antennas used have a half-power beamwidth of approximately 9° and are specified for coverage of the complete K_a -band (26.5 to 40 GHz); they are approximately 15 cm tall with an aperture 6 by 7 cm wide and offer a maximum wind loading area of 53 cm².

Analog processing after mixing

The mixing process produces a number of frequency products, namely a sum and difference, of the two MMW signals. The sum product is in the higher millimeter frequency range and is not used. The difference product, here in the audio frequency range, contains the frequency information that can be transformed into an indication of ice thickness. This signal amplitude is on the order of tens of millivolts, peak, and must be amplified to the order of several volts, peak, for data acquisition. The circuit and corresponding waveforms in Figure 41 were specifically designed for this function. The signal is amplified by a cascaded combination of an

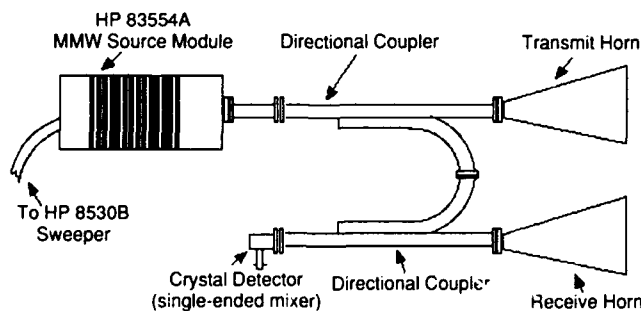
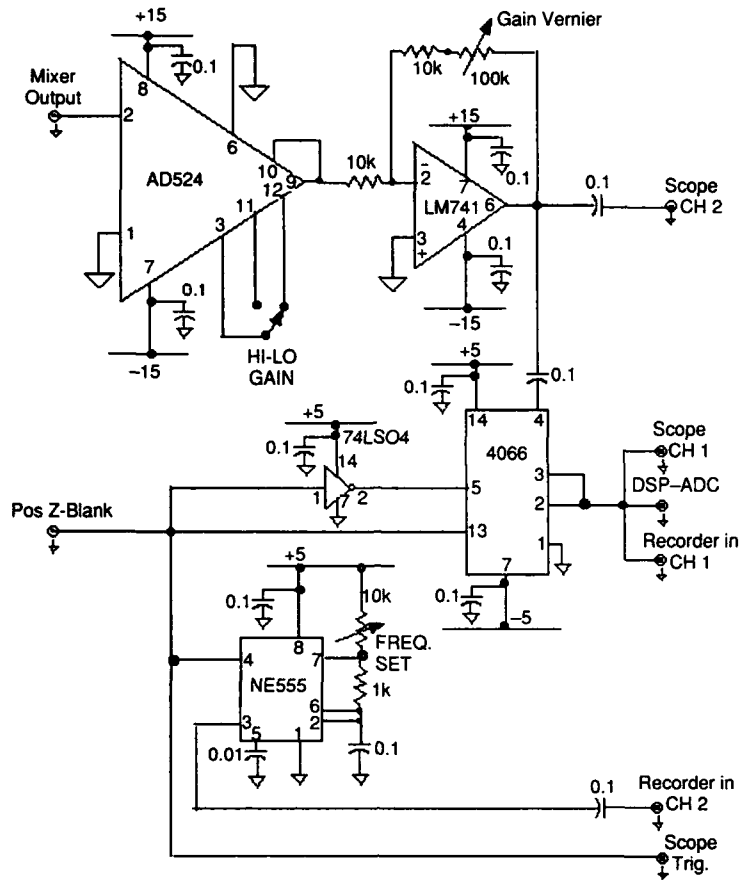
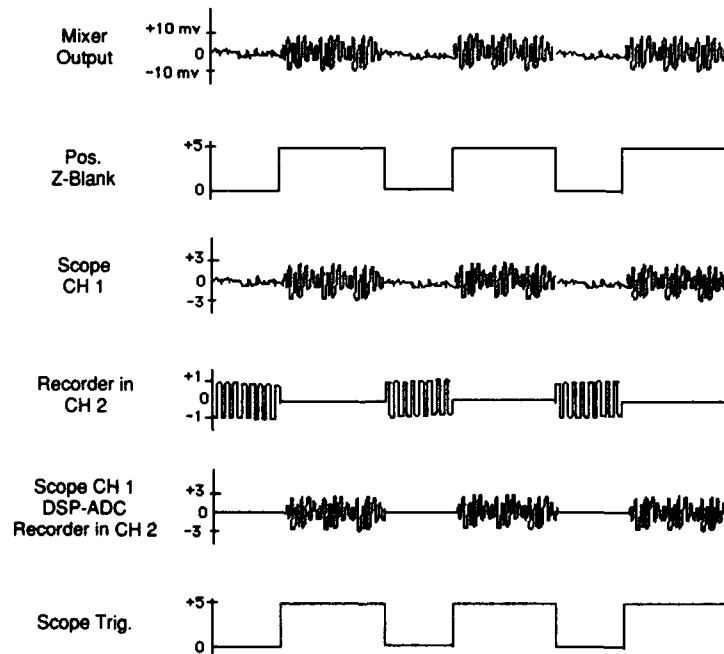


Figure 40. Radar front end.



a. Schematic.



b. Waveforms (waveform period is determined by sweep rate).

Figure 41. Amplifier-synchronizer used after mixing.

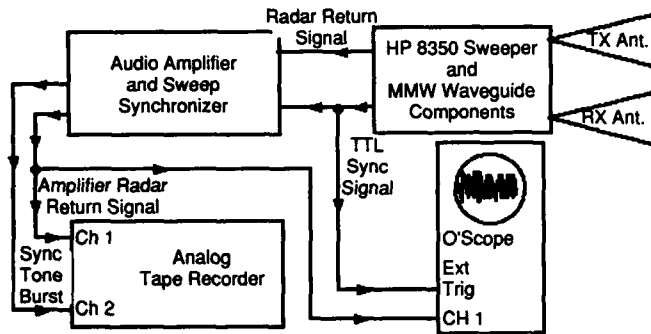


Figure 42. Record-only mode.

Analog Devices AD-524 adjustable gain instrumentation amplifier (switch-selectable gains of 100 or 1000) and an LM-741 op-amp, configured as an inverting adjustable gain amplifier (vernier gain from 1 to 10).

Gain is manually adjustable to provide reflected signal level strength, as displayed on the oscilloscope, within an acceptable amplitude range (± 3 V) for data acquisition. Individual radar scans are frame synchronized using the HP 8350B MMW sweeper "Positive Z-Blank," a TTL (Transistor-Transistor Logic) level signal that is logic-high (+5 V) during the frequency sweep and logic-low (0 V) during retrace. When radar data are recorded for subsequent processing and analysis, the TTL level, Positive Z-Blank signal, from the HP 8350B, is used to synchronously key an NE-555 astable oscillator producing bursts of 5-kHz tone. The amplified radar signal and the tone-burst synchronization signal are recorded on two separate channels of an analog data recorder. When real-time data are acquired and processed (Fig. 39), the radar signal and the Positive Z-Blank signal are multiplexed into a single data acquisition channel. The system data acquisition-DSP arrangement uses level and edge triggering to frame-synchronize the data stream.

A hardware block diagram of the record-only mode is shown in Figure 42, where system components, as earlier described, are assembled to collect and store profile survey data on audio tape for processing later. While there is no provision for instantaneous display of profiling results, the limited size, weight, complexity and power consumption facilitates portable and mobile operation.

In the playback mode, data that have been acquired and recorded to tape either during real-time or record-only operation can be played back and input to the computer for processing. A hardware block diagram of the playback mode is shown in Figure 43.

A circuit designed specifically for playback and corresponding waveforms is shown in Figure 44. Here, the 5-kHz tone bursts recorded to tape in the real-time or record-only modes are decoded back into the TTL synchronization pulse train by an NE-567 phase-locked

loop tone decoder. The reconstructed synchronization signal is interfaced to a 4066 CMOS analog switch configured as a two-channel analog multiplexer, which inserts a 5-V start-of-frame pulse into the data stream during the sweeper retrace prior to the beginning of each radar scan. Again, in this configuration, the system data acquisition-DSP arrangement uses level and edge triggering to frame-synchronize the data stream.

In both the record and playback modes, a Tektronics 475 dual-trace oscilloscope is employed as a diagnostic tool to monitor sweep rate, signal amplitude and general waveform appearance.

Raw data storage

The amplified output of the radar mixer and synchronization tone burst are recorded on an HP 3964A reel-to-reel four-channel instrumentation recorder capable of being powered from an ac or dc source. Manufacturer specifications for this analog data recorder indicate a 30-dB SNR and a 5-kHz audio bandwidth when recording at the highest tape rate of 38 cm/s (15 in./s). Here, a 550-m-long reel of tape provides approximately 15 minutes of recording time. Radar range, playback-mode SNR ratio and scan rate can be improved by substituting a Digital Audio Tape (DAT) recorder for the analog recorder used in the prototype. The greater audio bandwidth of the DAT (20 kHz compared to 5 kHz for the analog recorder) permits a proportional increase in scan rate and radar range. With a 70-dB SNR, the DAT recorder is approximately 10 to 20 dB better than the radar system noise floor and more than 40 dB better than the analog tape noise floor, thus permitting an increase in radar range. Use of the HP 3964A recorder prevailed because of the urgency of taking data in the winter, economics and in-house availability.

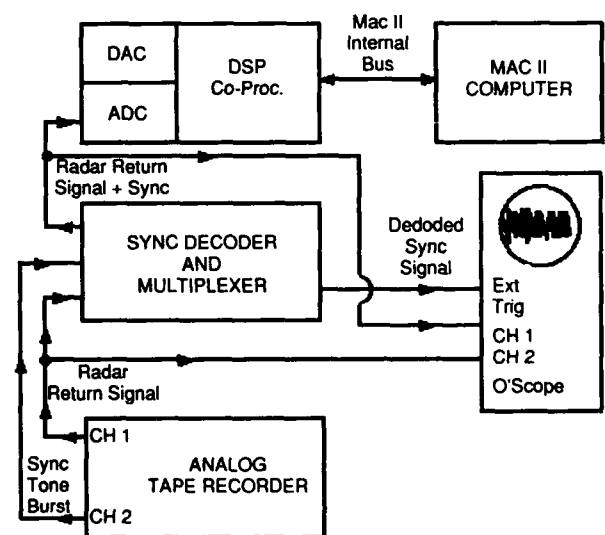
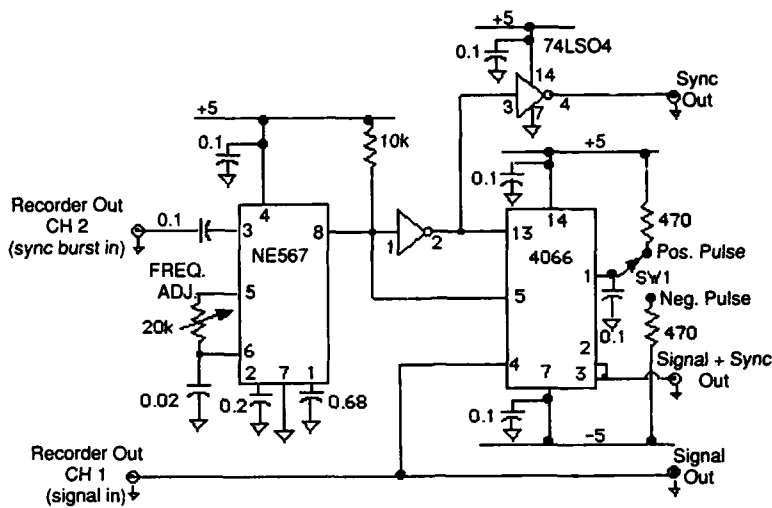
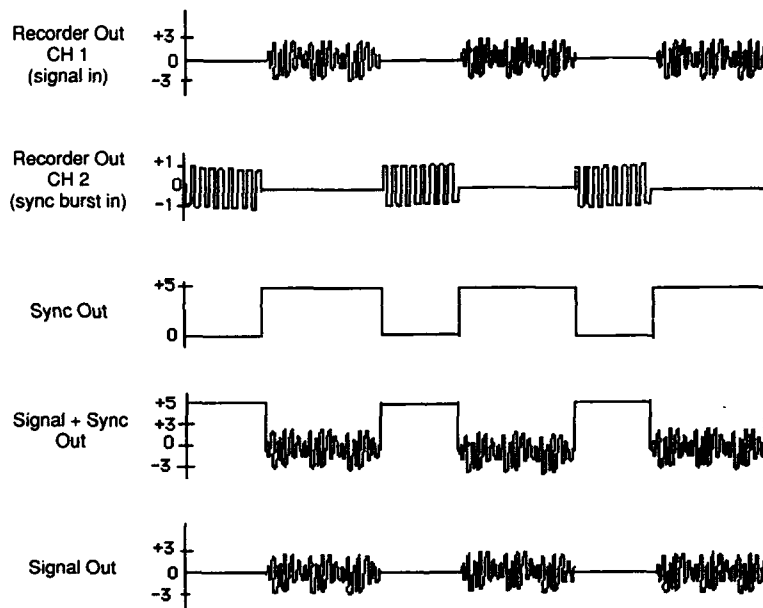


Figure 43. Playback mode.



a. Circuit schematic.



b. Waveforms (waveform period is determined by sweep rate).

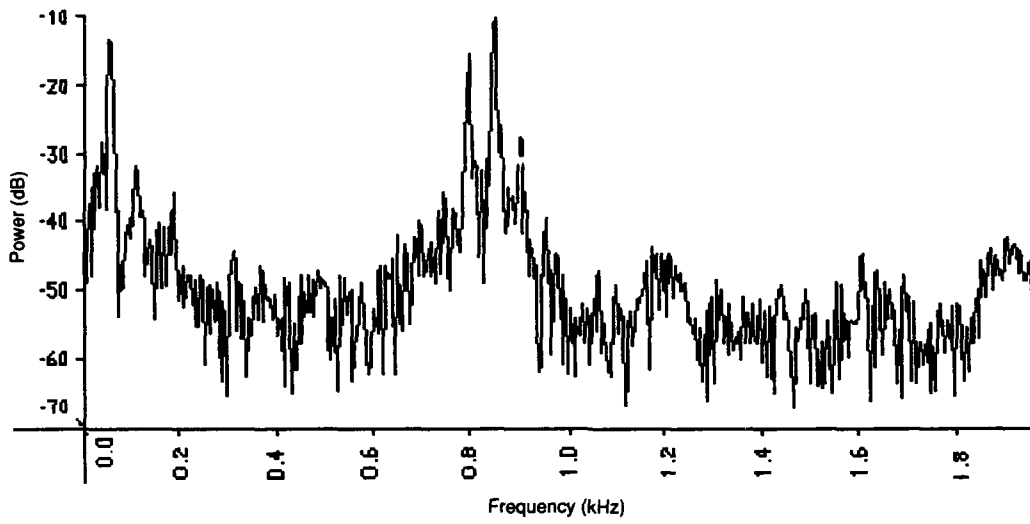
Figure 44. Playback synchronization decoder.

Digital signal processing

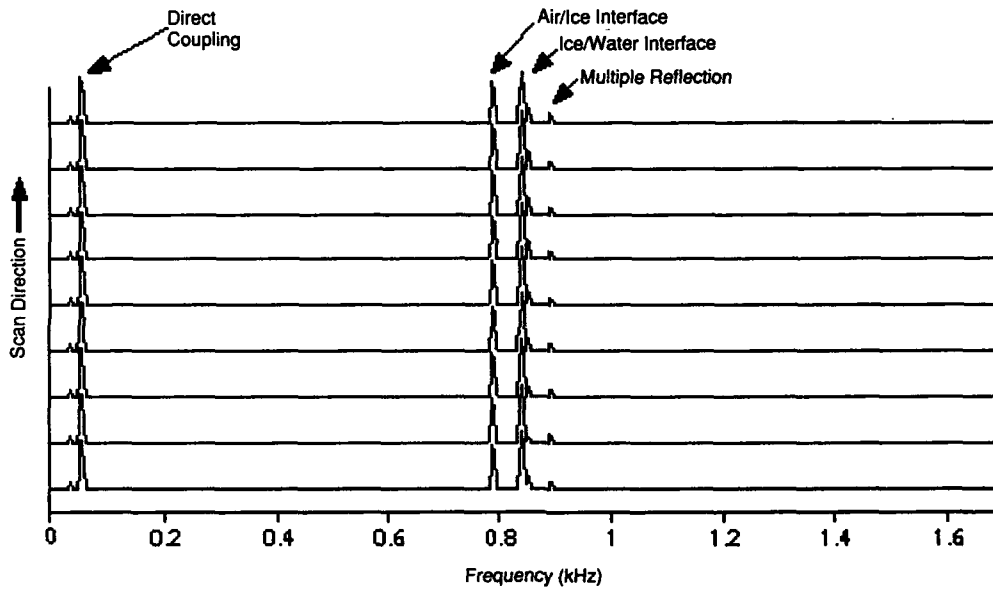
A wide choice of DSP boards was available, including one Macintosh-based and several DOS-based boards. All DSP systems considered for this application had reasonably similar capabilities, specifications, economics and software support. Selection was based on the in-house availability of a Macintosh II computer as well as for reasons of simplified DSP hardware procurement.

Data are acquired and digital signals processed by a Spectral Innovations, Inc., MacDSP256KNI coprocessor board, with an AT&T WE DSP32 32-bit floating-

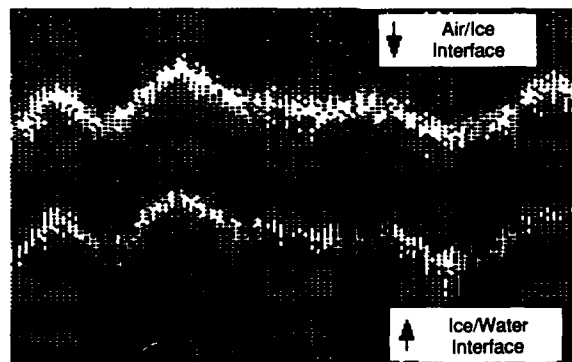
point, 32 MFLOP (Million Floating-point Operations per second) chip and a piggyback 16-bit 128-kilobyte-per-second analog-to-digital converter. The MacDSP 256KNI board, under software control, is capable of vector mathematics for arithmetic, digital filtering, windowing and other DSP functions. Processed data can be displayed in several formats, including single trace, waterfall and spectrogram. Single-trace display (Fig. 45a) is a log-magnitude versus linear-frequency representation of one frequency domain-transformed and processed radar scan, which is updated with each sub-



a. Single-trace (log magnitude presentation).



b. Waterfall (linear magnitude presentation).



c. Spectrogram (log magnitude presentation).

Figure 45. Typical DSP displays.

sequent scan. The waterfall representation (Fig. 45b) displays a continuously scrolled sequence of single scans.

In a spectrograph display (Fig. 45c), discrete signal magnitude quanta are represented by a range of color or gray scale. In monochrome, as illustrated, this results in signal magnitudes greater than a preset threshold appearing as white and those below the threshold as black. The level can be set in the DSP software to display clearly both the air/ice and ice/water interfaces. A multi-color spectrographic display provides significantly greater graphical resolution than is possible with a monochromatic display by indicating intermediate levels of signal intensity by a color gradient. Unfortunately, for this development and consequently for illustration in

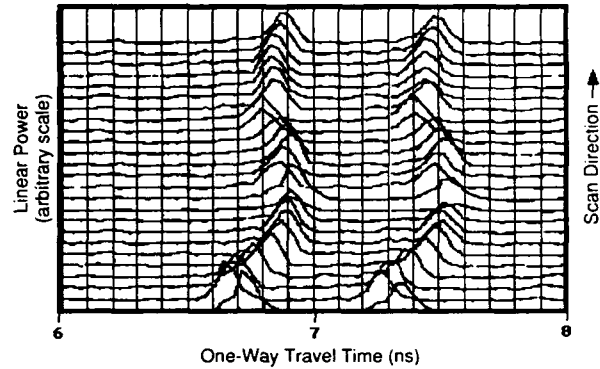


Figure 46. Linear stacked-scan waterfall representation of reflections from an 8-cm-thick granite slab (as processed by Cricket Graph).

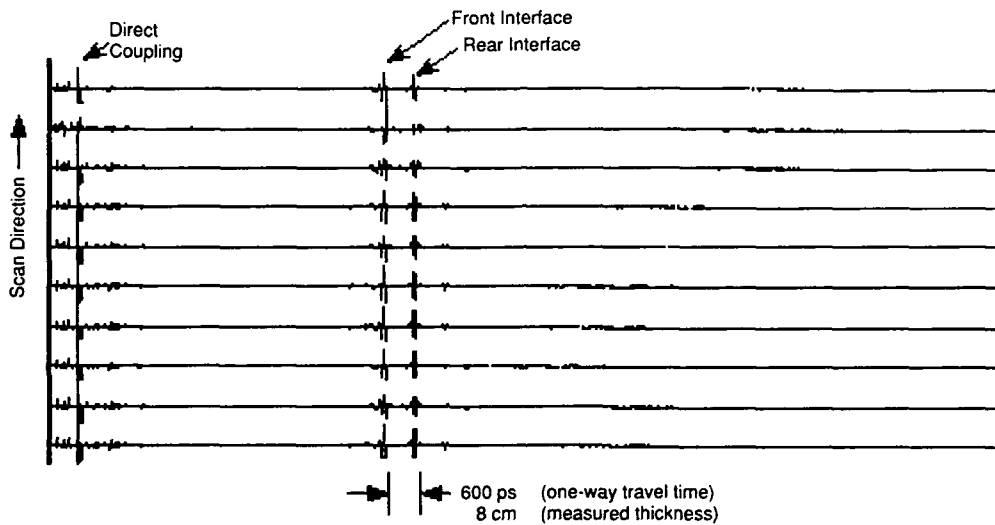


Figure 47. Radan-processed and wiggle-formatted display of reflections from an 8-cm-thick granite slab.

this document, only monochromatic display output was available. Ice or snow thickness is then computed as a function of the distance from peak to peak on the single scan or waterfall display and as the center-to-center distance of the two white bands on the spectrogram. Additionally, acquired data can be formatted for stacked-scan graphical display using the Cricket Graph (Cricket Software, Inc.) software package (Fig. 46) or for further processing and display by the Radan (Geophysical Survey Systems, Inc.) geophysical radar analysis program (Fig. 47).

Test platforms

At various stages the radar was tested and operated using a boom, cart, truck and helicopter over a variety of ice conditions.

Boom-mounted test platform

Several profiling measurements were made with the radar antennas deployed on a 4-m long cantilevered arm positioned over the ice from a shore-mounted tripod (Fig. 48). This configuration was used for ice too thin to support safely the system and operator. The boom was moveable in elevation (from 2 to 3 m) above the ice surface and in a 180° arc. All electronics, including the MMW sweep oscillator, were located on the shore. The MMW sweep signal was coupled to the radar front end by a 4-m length of WR-28 waveguide and the audio output from the mixer was returned to the system via a 6-m length of RG-58/U coaxial cable.

Cart-mounted test platform

The radar was mounted on a manually propelled cart

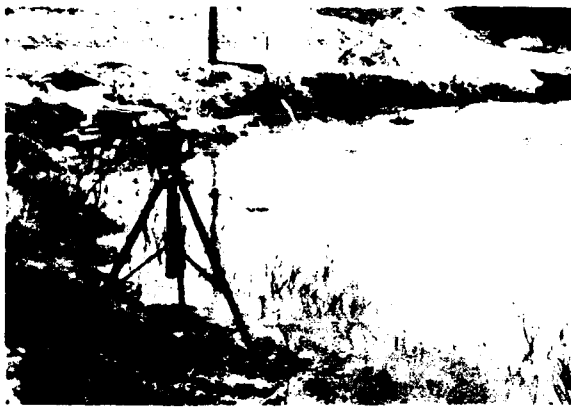


Figure 48. Boom-mounted profiling arrangement.

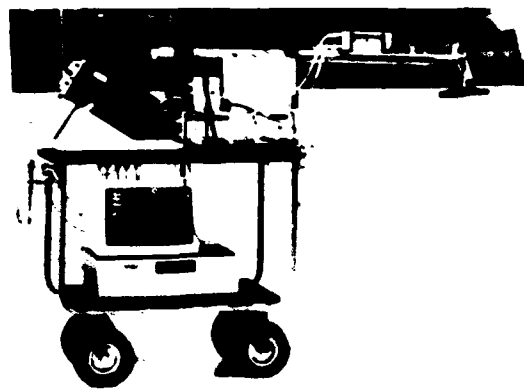


Figure 49. Pre-prototype mounted on the cart.



Figure 50. Cart-mounted device profiling pond ice.

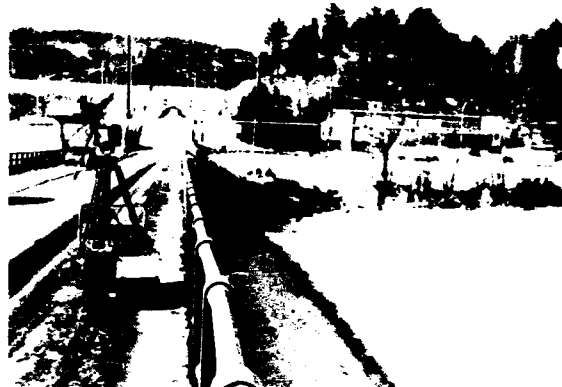


Figure 51. Cart-mounted radar deployed on a bridge.



Figure 52. Truck-mounted radar (range is approximately 1 m).



Figure 53. Radar mounted on a truck using a tripod (range is approximately 2 m).

and supplied with electrical power via an extension cord connected to a ground-fault interrupted 117 Vac main. Short-length profiles (less than 25 m) were made on an indoor ice sheet grown on a concrete, refrigerated floor, or on ice, marginally thick enough (about 10 cm) to safely support the cart and operator and formed on a shallow (about 0.5 m deep) outdoor pond (Fig. 49).

Where the ice was thicker (about 30 cm) and capable of supporting heavier loads, longer profile runs were possible by powering the radar from a gasoline generator mounted on the cart (Fig. 50)

A variant of the cart-mounted arrangement was used for profiling river ice from a bridge deck. In this arrangement a tripod was used to elevate the antennas

above the bridge safety railing and provide sufficient horizontal displacement to prevent extraneous reflections from the bridge structure (Fig. 51).

Truck-mounted test platform

The radar was mounted on a truck to simulate the ground speed and radar range that would be encountered in the air. With ice sufficiently thick to safely support a vehicle (more than 30 cm), the radar was mounted on the rear of a pickup truck and driven across a frozen pond at speeds up to 40 km/hr, allowing for high-speed profiling experiments. A truck was also used for measurements where the ice was snow-covered and it would have otherwise been difficult to manually propel the cart. Radar range was 1 m with the 4-m long antenna boom mounted across the top of the cargo bed (Fig. 52). Profiling without extraneous radar reflections from the vehicle body and without disturbance to the snowcover was possible by placing the boom-mounted antennas off to the side and away from the vehicle. With the antenna boom supported by a tripod bolted to the pickup bed, the range was increased to approximately 2 m (Fig. 53). Electrical power was supplied by a gasoline powered generator.



Figure 54. Profiling helicopter. Waveguide leads out the rear window to MMW horn antennas visible in inset.

Airborne test platform

The radar setup for airborne deployment was similar to that used during ground-mounted testing. A 12-V battery and power inverter were used for a power source. The two horn antennas were affixed centrally to the underside of a Bell Jet Ranger 206B helicopter (Fig. 54) and were adjusted to point normally to the ground during survey flight.

Power requirements

The power requirement for the prototype (Table 7) is calculated based on the power specifications on the equipment nameplates.

Table 7. System power requirements (VA).

HP 8350B MMW sweeper	375
HP 3964A recorder	150
Tektronics 475 oscilloscope	100
Audio amplifier and synchronizer	5
Total power requirement	630

The recorder, oscilloscope and audio amplifier and synchronizer can be powered directly by battery. The sweeper requires a dc-to-ac inverter for battery operation. If the Mac II computer were also to be field-operated, an additional 500 VA of dc-to-ac inverter capacity would be required for battery operation.

Economic considerations

Since the majority of hardware used here was obtained from existing laboratory inventory or borrowed from other projects, there was little actual expenditure. The following accounting (Table 8) is provided to indicate the overall cost should all system components be purchased new. Costs are approximated to the nearest \$100 in 1991 dollars and are listed by functional subsystem. In the case of manufacturer discontinued components (e.g., HP 3964A analog data recorder), a price of a current-technology DAT (TEAC RD-101) is substituted.

Table 8. Prototype implementation costs.

MMW source	
HP 8350B sweep oscillator	\$4,900
HP 83550B RF plug-in	\$16,000
HP 83554A MMW source module	\$9,000
	<u>\$29,900</u>
Radar front end	
Scientific Atlanta standard gain horns (2 ea)	\$1,600
HP R422C crystal detector	\$800
Miscellaneous WR-28 waveguide	\$500
HP 752AD directional couplers (2 ea)	\$2,000
	<u>\$4,900</u>
Processing after mixing	
Amplifier and synchronizer electronics	\$500
	<u>\$500</u>
Bulk data storage	
HP 3964A analog recorder (TEAC RD-101)	\$8,600
	<u>\$8,600</u>
Digital signal processing	
Macintosh II computer (8 MB RAM, 140 MB HD)	\$5,000
Macintosh monochromatic monitor	\$500
MacDSP256KNI data acquisition/DSP coprocessor	\$5,000
Data acquisition/DSP software	\$2,600
	<u>\$13,100</u>
Grand Total	<u>\$57,000</u>

Table 9. Summary of survey studies.

Survey study	Tape no.	Date	Location	Mode	Speed (km/hr)	Range (m)	Ice thickness (cm)	Air temperature (°C)	Ice surface conditions
A	NA	2 Nov 90	Thompson Arena Ice Rink, Dartmouth College, Hanover, N.H.	Cart	3	1.2	3	0	Very smooth (surface prepared by rink surfacing machine).
B	2	26 Dec 90	Overflow pond, CRREL	Fixed	0	2	5	2	Clear ice, minimal surface roughness.
C	6	28 Dec 90	Overflow pond, CRREL	Cart	3	1	7-8	-5	Snow cover; shoveled clear; minimal surface roughness.
D	7	8 Jan 91	Post Pond, Lyme, N.H.	Cart	3	1	20-25	-10	Smooth ice with < 1 cm of snow cover.
E	9	15 Jan 91	Post Pond, Lyme, N.H.	Truck	10	1	30	-7	18 cm dry, low-density snow cover over ice with minimal surface roughness.
F	10	23 Jan 91	Post Pond, Lyme, N.H.	Truck	10	2	35-40	-18	≤1 cm snow cover with roughened texture from refrozen meltwater.
G	11a	25 Jan 91	Connecticut River, from Ledyard Bridge, Hanover, N.H.	Cart	3	5-6	25-35	-12	Clear ice, minimal surface roughness.
H	11b	25 Jan 91	Connecticut River, from Ledyard Bridge, Hanover, N.H.	Cart	15	5-6	25-35	-12	Surface roughness ≤1 cm from refrozen snowplow ejecta on ice surface.
I	13	26 Feb 91	Turtle Pond, Concord, N.H.	Helicopter	15	3-5	30	>5	Smooth ice with patches of ≤1 cm of wind-packed snow cover.
J	14	26 Feb 91	Pemigewasset River, Franklin, N.H.	Helicopter	15	3-5	30	>5	Smooth ice with patches of ≤1 cm of wind-packed snow cover.

RESULTS

Several survey studies were conducted to examine the performance of the radar over a variety of ice sheet and snow cover conditions. Profiling tests were conducted in the laboratory and field from stationary and mobile ground platforms, and airborne radar profiling surveys were made over freshwater pond and river sites. Survey parameters are summarized in Table 9.

Skating arena profile (survey study A)

On 2 November 1990 thin ice was profiled employing the pre-prototype radar mounted on a cart that was manually propelled over an ice skating arena (Thompson Arena, Dartmouth College, Hanover, New Hampshire) where approximately 3 cm of cold, smooth ice overlaid a concrete floor. The arena presented a viable alternative to inaccessible natural conditions for testing performance over thin ice that could be directly measured. The results of a survey run of approximately 15 m (Fig. 55) were plotted using DeltaGraph (Deltapoint, Inc.) and presented in a stacked-scan, linear magnitude format. Appendix A gives survey details. The lack of a substantial dielectric contrast between the concrete and the ice prevented strong bottom returns. Nevertheless,

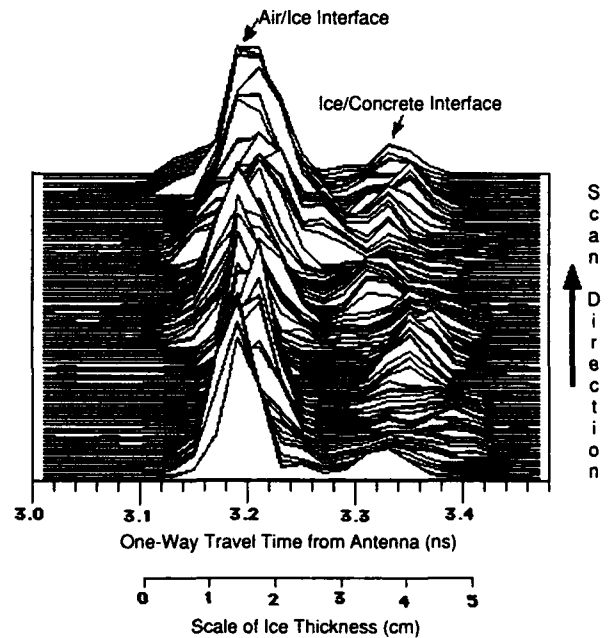


Figure 55. Segment of skating arena profile (linear power magnitude; arbitrary vertical scale).

it is apparent that the minimum resolution of this system is far less than the range of thickness encountered. It was not possible to obtain ground truth since it would have required drilling into the ice on the rink with the potential risk of damage to the refrigeration system. However, rink maintenance personnel reported that the ice typically ranged in thickness from 2 to 4 cm over the extent of the slab.

Stationary profiling of thin pond ice (survey study B)

This experiment examines the capabilities of the MMW FM-CW radar for profiling thin, naturally occurring pond ice. Since the ice was too thin to traverse safely, the radar was mounted on the shore of the pond and the antennas extended over the ice using a boom. Figure 56 shows a sequence of several radar returns extracted from profiles of a frozen outdoor pond made over a 3-day period in late December 1990, during which ice thickness increased from approximately 5 to 10 cm. The pond surface was smooth, with only a light, dry snow cover less than a centimeter thick. Antenna

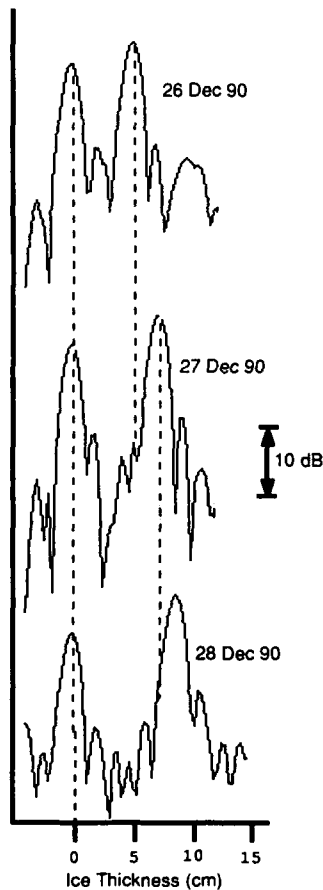


Figure 56. Sequence of increasing ice thickness on a frozen outdoor pond.

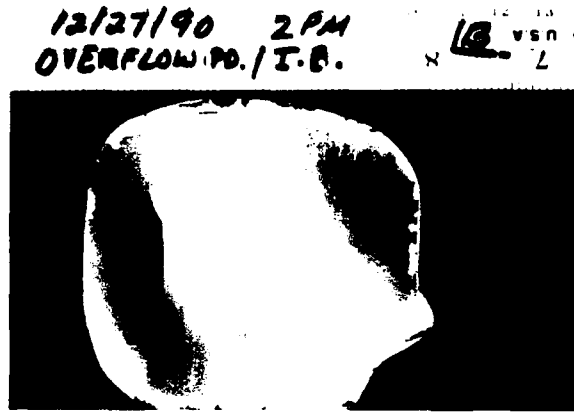


Figure 57. Vertical cross section of an overflow pond ice core (from data of 27 December 1990).



Figure 58. Indication of surface roughness of overflow pond ice cover (from data of 27 December 1990).

height was about 2 m. Direct measurement of the ice thickness by drilling verified the radar thicknesses. It is apparent from the data that the resolution limit is better than 3 cm.

Figure 57 is a vertical cross-section of a typical core sample obtained during this series of profiling surveys. The core revealed a solid ice cover with air bubble inclusions of less than 0.5 mm, typical of pond ice. An indication of surface roughness is given in Figure 58. The surface had a small pitting with height variations on the order of less than 1 mm. Appendix A gives survey details.

Cart-mounted profiling of overflow pond (survey study C)

On 28 December 1990, on a small overflow pond located on CRREL property was profiled. Here, the ice ranged in thickness from 5 to 9 cm with no snow cover. A short (25-m) profile was made using a cart carrying all components. The lightweight cart permitted the profiling of naturally occurring pond ice too thin to support a heavier profiling vehicle. Figure 59 is a DSP spectro-

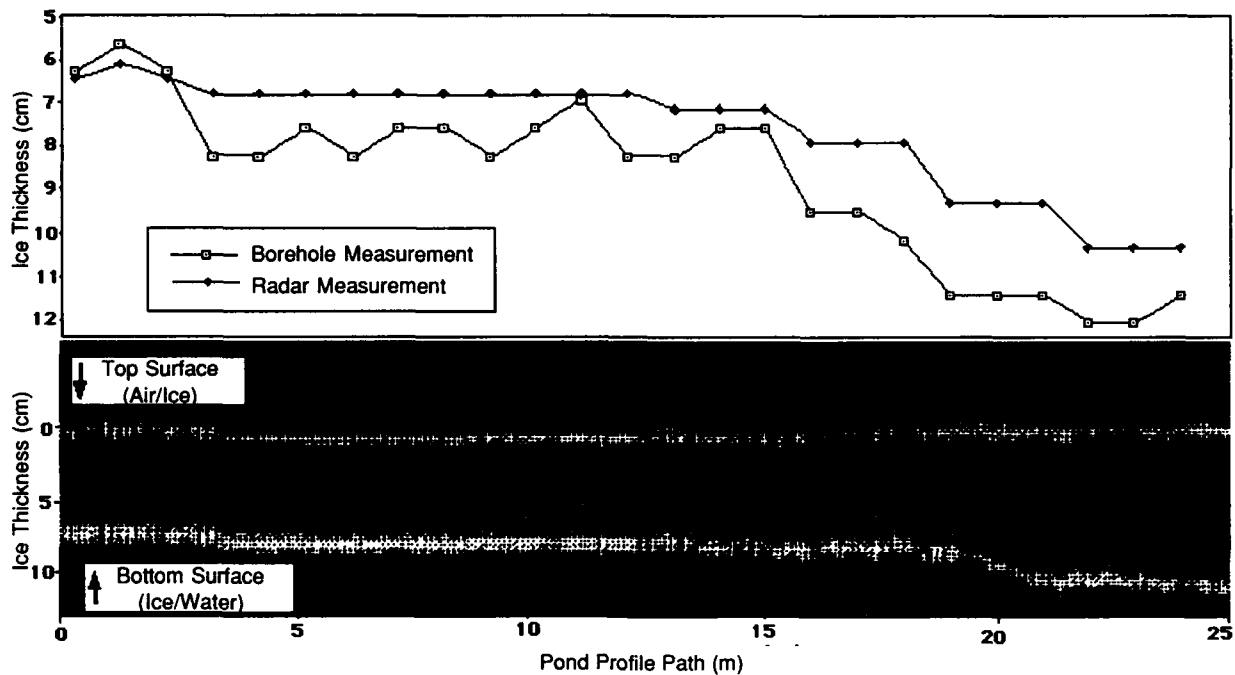


Figure 59. Radar and borehole measurements from overflow pond (not corrected for borehole tape offset error).

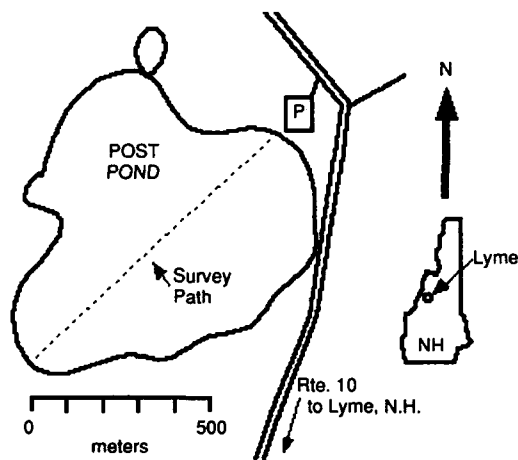


Figure 60. Post Pond survey path.

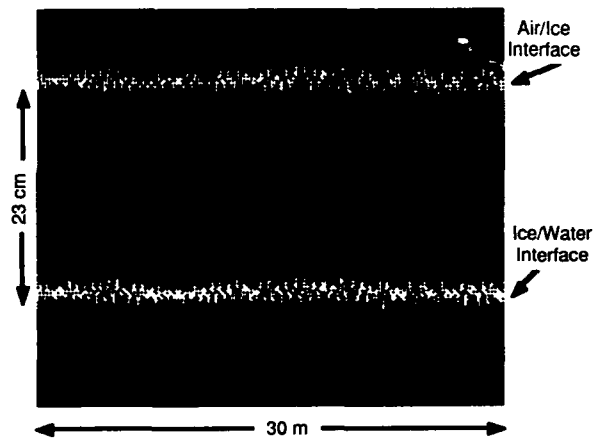


Figure 61. Segment of Post Pond profile from survey by cart-mounted radar.

graphic display of the radar ice thickness profile and graph comparing radar data with borehole measurements. Here, the comparison plot is not corrected for a 1.5 cm offset error in the borehole measurement tape. Further discussion of the tape offset error is given in the *Borehole and Radar Data Error Analysis* section. Appendix A gives survey details.

Cart-mounted profiling of Post Pond (survey study D)

On 8 January 1990, as the ice cover thickness had increased to approximately 30 cm, the cart-mounted system equipped with a gasoline-powered electrical

generator was taken out on Post Pond, near Lyme, New Hampshire, to profile of the entire length of the Pond (Fig. 60). A segment of the data is shown in Figure 61.

On 11 January 1991 several core samples were taken of Post Pond ice from along the survey path. Figure 62 shows a photograph of a vertical thin-section (in polarized light) of one of the ice cores, indicating the crystalline structure of the ice and a series of horizontal thin-sections (non-polarized light) taken at various points along the core to indicate the dimensions and density of air bubble inclusions in the ice. The core was solid and no water inclusions or snow ice layers of low density were encountered.

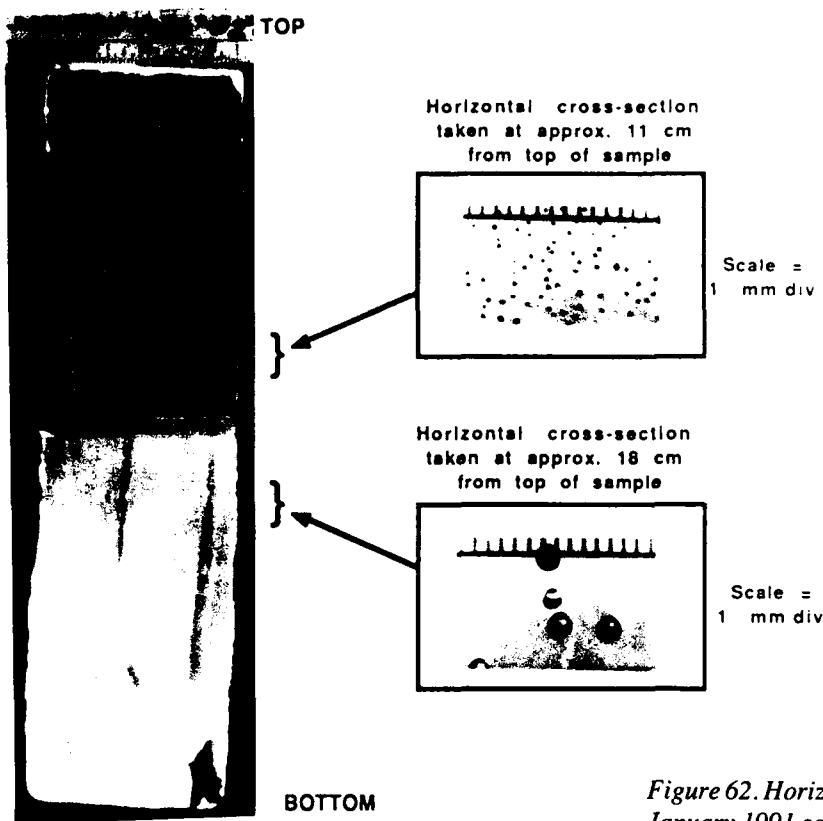


Figure 62. Horizontal and vertical cross sections of 11 January 1991 sample of Post Pond ice core.

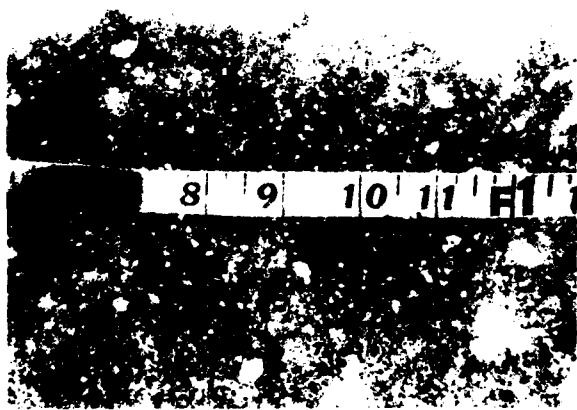


Figure 63. Indication of surface roughness of Post Pond ice cover (from data of 11 January 1991).

An indication of surface roughness of the pond is given in Figure 63. The surface roughness is estimated at 1–2 mm. There was no significant snow cover. Appendix A gives survey details.

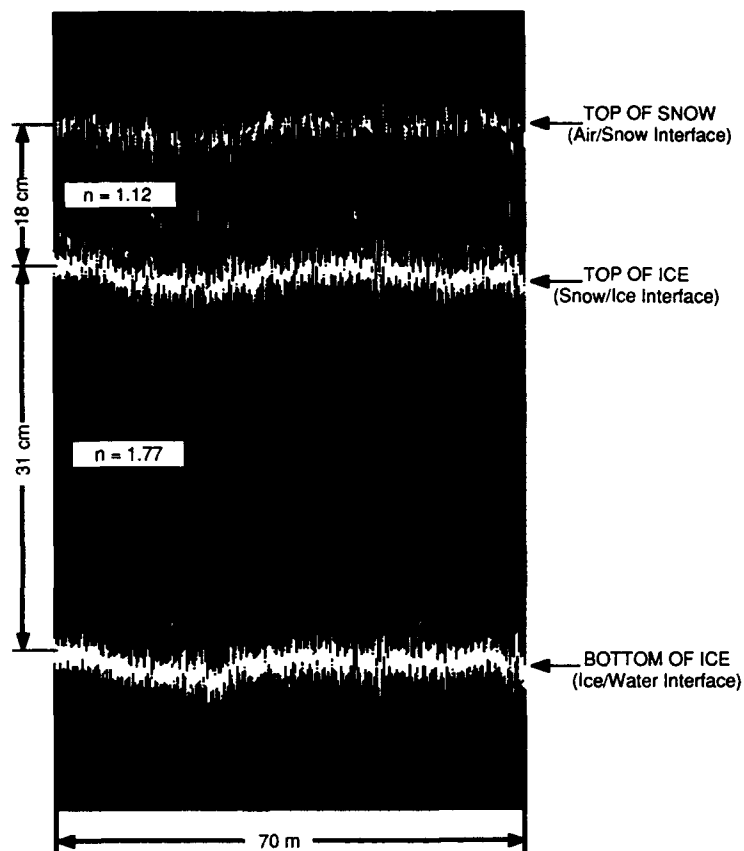
Profiling of snow-covered pond ice (survey study E)

High-speed profiling is illustrated in Figure 64a, which shows both snow cover and ice thicknesses on

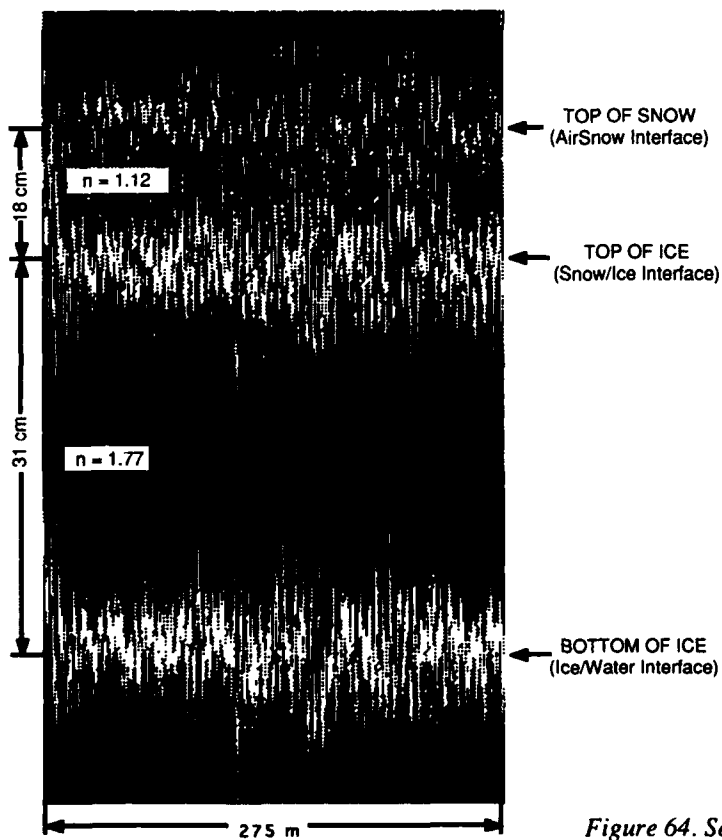
Post Pond in Lyme, New Hampshire. The data were collected on 15 January 1991 from a truck-mounted version of the prototype radar traveling at a velocity of 10 km/hr. Interpretable data were also obtained at ground speeds of up to 40 km/hr (Fig. 64b), with some degradation in visual quality caused by the mechanical vibration of the truck moving over rough terrain coupled to antenna boom assembly. This subjected the antennas to substantial vertical displacement, pitch and roll, resulting in intra-scan and scan-to-scan range and signal level variations. Appendix A gives survey details. The pond was covered with approximately 18 cm of cold, low-density snow (0.15 g/cm^3). Boreholes revealed solid ice with no water inclusions and with bubble dimensions and density similar to that found along the same survey line during the survey study D, 4 days earlier. In Figure 64 the thickness of the snow cover was calculated in a similar manner to that of the ice, using a value for the index of refraction, $n_{\text{snow}} = 1.12$, based on the correlation of measured snow density with the results reported by Cummings (1952). The radar results agree favorably with ground truth measurements at the test site.

Truck-mounted profiling of pond ice (survey study F)

Figure 65 shows a portion of a profile of Post Pond



a. Taken at 10 km/hr.



b. Taken at 40 km/hr. Deteriorated spectrogram quality primarily caused by vibration of sensor boom at high ground speeds.

Figure 64. Segment of Post Pond profile with snowcover.

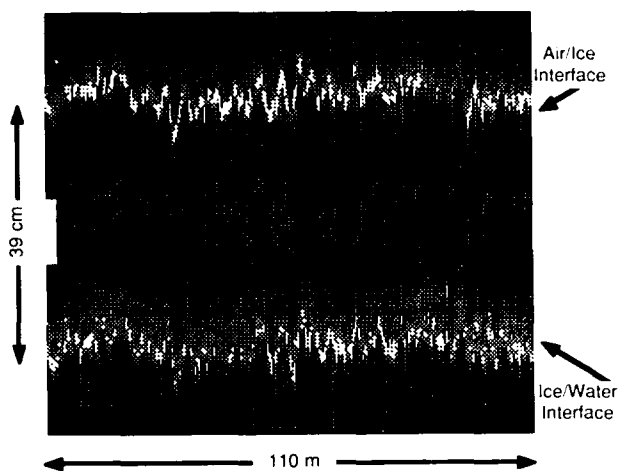


Figure 65. Segment of Post Pond profile without snowcover taken at 10 km/hr.



Figure 66. Indication of surface roughness of Post Pond ice cover without snowcover (from data of 23 January 1991).

ice with no snow cover. The data were collected on 24 January 1991 from a truck-mounted version of the prototype radar traveling at a velocity of 10 km/hr. The earlier snow cover had melted and refrozen, providing an increased surface roughness and eliminating all but a subsequent, minimal windblown snowcover. The radar results agree favorably with ground truth measurements at the test site.

On 23 January 1991 several core samples were taken of Post Pond ice from along the survey path. An indication of surface roughness is given in Figure 66. A photograph of a vertical thin-section (in polarized light) of one of the ice cores, indicating the crystalline structure of the ice, and a series of horizontal thin-sections (non-polarized light) taken at various points along the core to indicate the dimensions and density of air bubble inclusions in the ice, is presented in Figure 67.

Cart-mounted profiling of Connecticut River ice (survey studies G and H)

This experiment was performed to verify the capability of the radar to profile ice thickness from typical helicopter survey altitudes. A survey was made on 25 January 1991 from Ledyard Bridge over the Connecticut River in Hanover, New Hampshire, at an altitude of 5 to 7

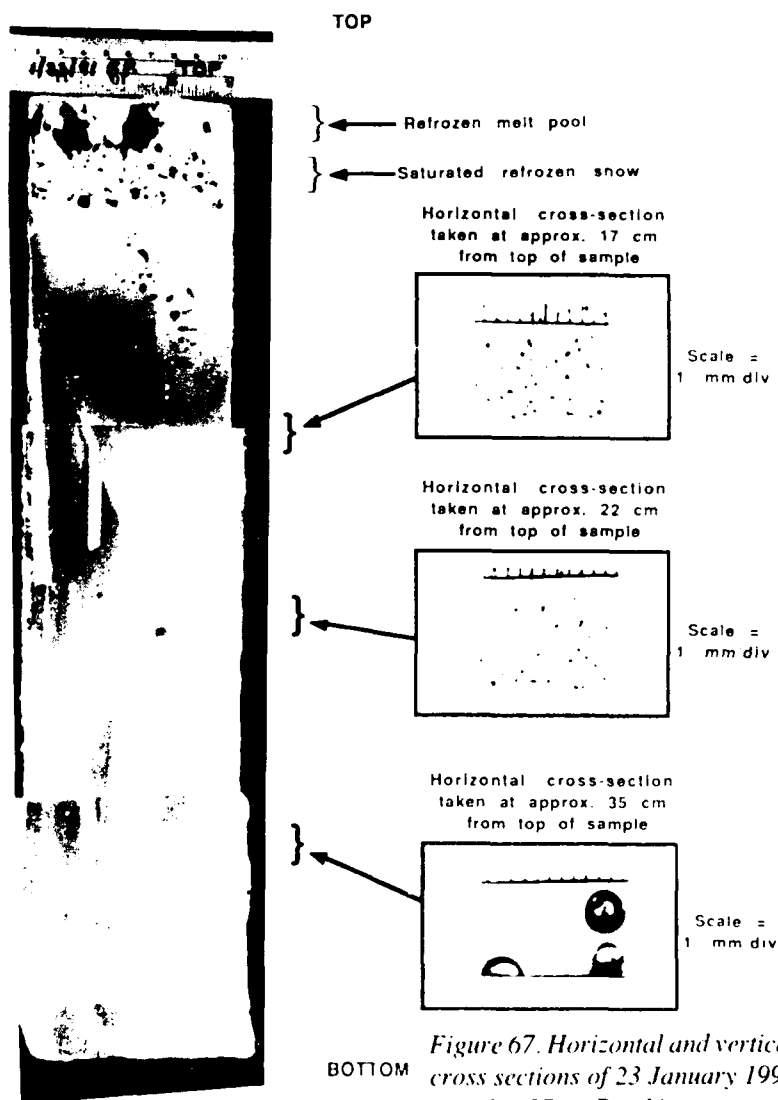


Figure 67. Horizontal and vertical cross sections of 23 January 1991 sample of Post Pond ice core.

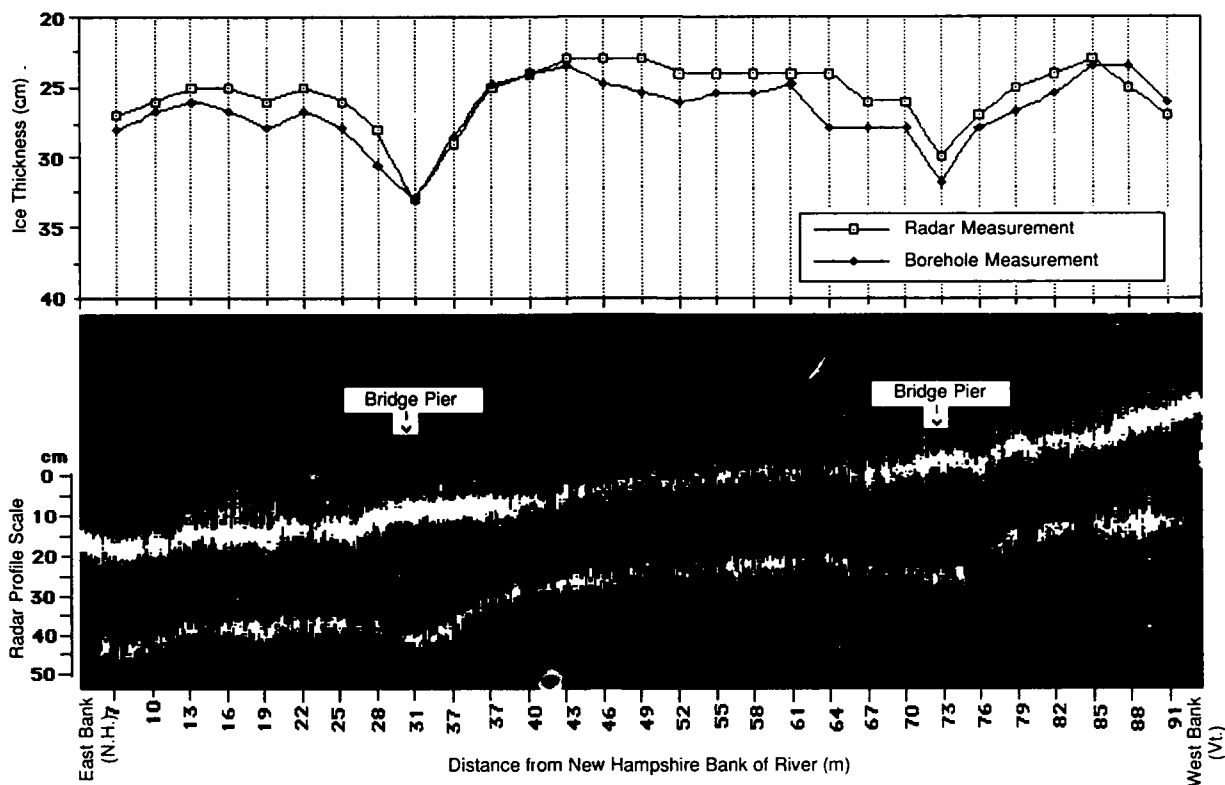


Figure 68. Radar and borehole measurements from Ledyard Bridge (not corrected for borehole tape offset error).

m. The system was mounted on a cart with the antennas suspended over the river by a 4-m-long boom and manually propelled across the bridge at approximately 3 km/hr.

Figure 68 compares borehole measurements with the spectrogram of a river ice profile. The plotted radar thicknesses were determined between the signal peaks at the center of the returns. The maximum ice surface roughness was estimated at less than 0.5 cm. Figure 69 indicates the maximum degree of ice surface roughness encountered. Variations in ice surface roughness approached 0.5 cm in the mid-span section of the survey. Closer to both river banks the ice was smooth with no measurable surface roughness. Relative surface roughness can be deduced by observation of the variation in intensity of the first surface return along the profile path. The smoother the reflecting surface, the less diffused the scattering and, consequently, the greater the magnitude of the received reflection above the spectrograph threshold; thus, the whiter (and broader) trace. The sloping appearance of the spectrogram is caused by an elevation differential of the bridge roadbed from the New Hampshire to the Vermont side.

Data from sections of the ice sheet with minimal surface roughness (survey study G) and with the rougher surface (survey study H and Fig. 69) were statistically analyzed and documented in Appendix A.



Figure 69. Indication of maximum surface roughness encountered while profiling Connecticut River ice from Ledyard Bridge.

Airborne profiling of lake ice (survey study I)

An airborne survey was undertaken on 26 February 1991 on Turtle Pond near Concord, New Hampshire (Fig. 70). For the pond survey shown in Figure 71, the helicopter was flown at an altitude of approximately 5 m and a ground speed of 15 km/hr. Other survey passes were conducted at altitudes of up to 7 m and ground speeds up to 40 km/hr with similar results. Boreholes

drilled along the survey path indicated an ice thickness in the range of 25 to 28 cm, which agrees favorably with the radar data.

Airborne profiling of river ice (survey study J)

Another airborne survey was done on 26 February 1991 along the Pemigewasset River near Franklin, New Hampshire (Fig. 72)

For the river profile segment shown in Figure 73, the helicopter was flown at approximately 2 m above the surface of the ice at a speed relative to the ground of approximately 10 km/hr. Other survey passes on the Pemigewasset River were conducted at altitudes of up to 7 m and ground speeds up to 40 km/hr with similar results. The deviations from straight horizontal traces visible in the spectrogram are ascribable to variations in helicopter altitude.

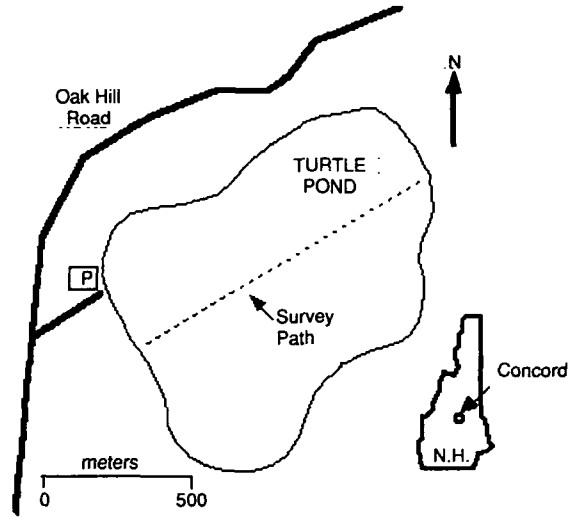


Figure 70. Turtle Pond survey site near Concord, New Hampshire.

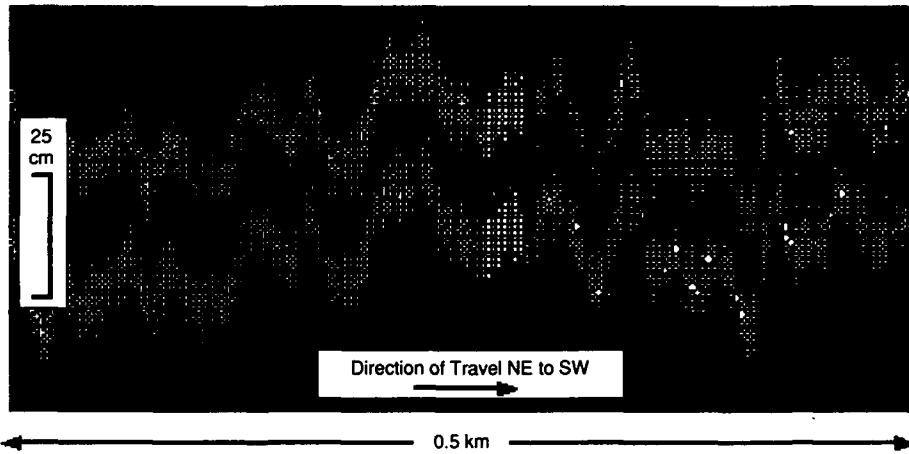


Figure 71. Segment of airborne profile of Turtle Pond (ground speed = 15 km/hr).

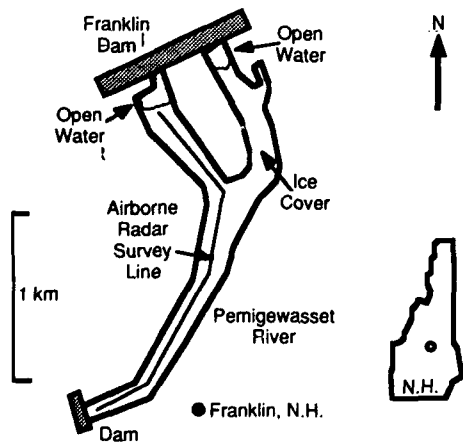


Figure 72. Pemigewasset River survey site.

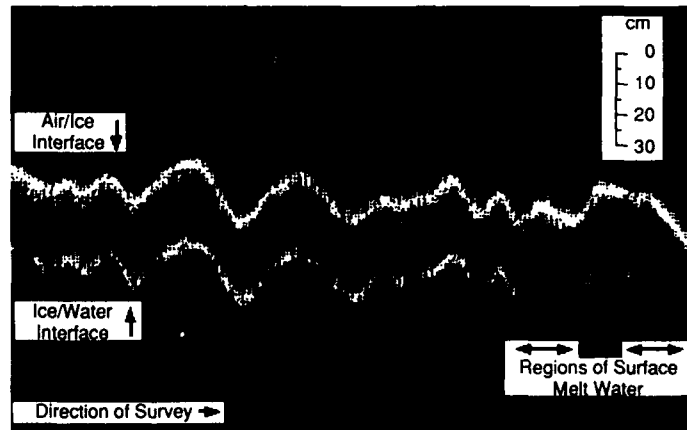


Figure 73. Segment of airborne profile of Pemigewasset River near Franklin, New Hampshire (ground speed = 8 km/hr).

Visual inspection of the horn antennas during hovering revealed small horizontal vibration, but no perceptible vertical vibration. Effects of helicopter vibration, pitch and roll during profiling runs were not apparent in the data. Surface melt water conditions were encountered and are seen in the spectrogram as segments where only the top surface reflection is extant due primarily to the high reflection coefficient of the air/melt water interface. The surface melt water was not always visually observable owing to snow cover, but was consistently and clearly indicated by the profiling radar. Ground truth was unavailable for this profile survey.

PERFORMANCE ANALYSIS

Survey data were analyzed to examine the performance of the radar and to compare it with theoretical expectations. Pulse shape spreading and asymmetry were statistically examined. The radar profiling data were compared with borehole thickness measurements to determine thickness measurement accuracy and statistical techniques were applied to determine if other physical attributes of the ice (e.g., surface roughness and dielectric loss) could be derived. A comparison between calculated and experimentally determined system SNR is presented. Specific details of individual surveys are included in Appendix A.

Theoretical measurement accuracy analysis

Error factors will be examined and their effect on system resolution accuracy calculated. Radar profiling field data are correlated with borehole measurements to obtain error statistics. A comparison and discussion of the resolution error values derived from these two exercises is included.

Radar system resolution error analysis

The factors in eq 30 contain the primary error sources in radar thickness measurements.

$$\text{Ice thickness (m)} = \frac{(F_{r2} - F_{r1}) (t_{\text{swp}}) c}{2(BW) (n_{\text{ice}})}$$

Changes in any of the variable terms of the above equation will yield a proportional error in the ice thickness measurement. The error contribution from each term is presented in terms of percent error in thickness measurement.

Bandwidth error. The swept bandwidth BW used with the HP 8350B MMW sweeper was 13.5 GHz, with a specified resolution error of ± 20 MHz or $\pm 0.15\%$ of the swept bandwidth.

Sweep time error. The HP 8350B has a sweep time

t_{swp} that can be set to ± 1.0 ms. For typical profiling experiments, t_{swp} is 0.066 s, resulting in a sweep time error of approximately $\pm 1.5\%$.

Sampling synchronization error. An error source related to t_{swp} is sampling synchronization offset error. Radar data time series sampling is triggered by a change in level and slope at the transition from imbedded synchronization signal to sampled time series data (see the *Analog Processing after Mixing* section). This synchronization event is detected within ± 1 sample interval. For a 1024 point time series scan, that translates into a 0.1% error.

Refractive index error. The *Dielectric Permittivity of the Water and Snow* section determined that the maximum variation of dielectric constant ϵ from air bubble inclusions in cold, natural freshwater ice is approximately -5% , resulting in a worst-case variation in the refractive index of ice n_{ice} of -2.24% .

Frequency bin resolution error. Errors corresponding to the air/ice and ice/water boundary difference frequencies, F_{r1} and F_{r2} , are primarily attributable to the FFT frequency bin resolution in relation to maximum range R_{max} and range resolution per FFT frequency bin R_{res} as indicated in eq 33 and 34 respectively.

$$R_{\text{max}} \text{ (m)} = \frac{(f_{\text{samp}}) (t_{\text{swp}}) c}{4 (BW)}$$

$$R_{\text{res}} \text{ (cm)} = \frac{2 (R_{\text{max}}) (100)}{(N_{\text{fft}}) (n_r)}$$

By use of the actual system parameters of

$$\begin{aligned} BW &= 13.5 \text{ GHz} \\ f_{\text{samp}} &= 15,620 \text{ samples/s} \\ t_{\text{swp}} &= 0.66 \text{ s/sweep} \\ N_{\text{fft}} &= 1024 \\ c &= 3 \times 10^8 \text{ m/s} \\ n_r &= 1.00 \text{ (for air) or} \\ n_r &= 1.77 \text{ (for freshwater ice)} \end{aligned}$$

the theoretical $R_{\text{max}} = 5.72$ m in air and $R_{\text{res}} = 1.12$ cm in air or 0.63 cm in ice. Figure 74 indicates the percent error in thickness resolution as a function of ice thickness for $R_{\text{res}} = 0.63$ cm.

Nonlinearity error. The effect of nonlinearities of the sweep frequency/time relationship must be considered. By use of the specified HP8350B sweep nonlinearity of 0.05%, and R_{max} and R_{res} calculated above, and eq 39, then

$$\frac{\delta f}{BW} = 0.0005$$

and

$$\frac{R_{\text{res}}}{R_{\text{max}}} = 0.002$$

so that the criterion

$$\frac{\delta f}{BW} \ll \frac{R_{\text{res}}}{R_{\text{max}}}$$

is satisfied.

Thus, the error from nonlinearity of the sweep frequency/time relationship over the given bandwidth is $\frac{1}{4}$ of that from the minimum range resolution. That is, resolution error from sweeper nonlinearity is 0.28 cm in air and 0.16 cm in ice.

Table 10 provides a summary of the error components affecting the resolution accuracy. The most significant source of thickness resolution error results from

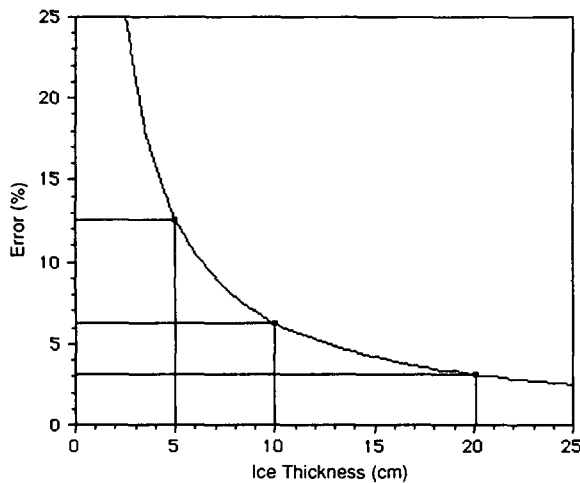


Figure 74. Error attributable to frequency bin resolution as a function of ice thickness for $N_{\text{fft}} = 1024$ (percent error for 5-, 10- and 20-cm-thick ice is indicated).

Table 10. Summary of calculated thickness resolution errors for 5- and 10-cm-thick ice.

Error type	Percent error (Relative to ice thickness)
Bandwidth error	± 0.15
Sweep error	± 1.5
Sampling synchronization error	± 0.10
Refractive index error	-2.24
Frequency bin resolution error (for $N_{\text{fft}} = 1024$)	± 12.8 (5 cm ice) ± 6.4 (10 cm ice)
Nonlinearity error	± 3.2 (5 cm ice) ± 1.6 (10 cm ice)

frequency bin resolution. Varying system parameters to obtain smaller values of R_{max} and larger values of N_{fft} may decrease this error, but to not less than the minimum resolution possible for a given radar system bandwidth. Thus, summing from Table 10, the calculated worst-case error that could result for 5-cm-thick ice is 15.5%, and for 10-cm-thick ice is 7.5%.

Borehole and radar data error analysis

As a measure of system accuracy, radar and borehole data are compared and analyzed. Two profiling surveys (survey studies C and F) included extensive thickness measurements taken from boreholes along the survey line. These measurements were made using a homemade depth gauge consisting of a collapsible "T-bar" linked to a length of measurement tape with $\frac{1}{4}$ -in. (0.64-cm) graduations. The T-bar and tape were placed down each borehole, hooked on the underside of the ice sheet and thickness measurements were taken at the ice surface to the nearest $\frac{1}{4}$ in. Borehole measurements were taken from a datum point at evenly spaced increments along the survey line across the ice sheet. Attempts were made to profile at a constant velocity so that the resulting survey spectrogram would represent a linearly scaled horizontal displacement. Radar thickness measurements were graphically derived from the survey spectrogram by measuring the distance between the center of the air/ice and ice/water reflection traces. The position of each radar thickness measurement was graphically correlated to an associated borehole using a datum (e.g., shoreline) and known physical features (e.g., bridge piers) as points of reference.

Initial comparison of radar and borehole measurements for both surveys indicated a systematic offset between borehole and radar measurements. This offset is on the order of 0.5 in. (1.27 cm) and is accounted for by a foreshortened linkage between the measurement tape and the T-bar. Verification of the precise offset of the particular tape used for these surveys is impossible since it was lost in the Arctic. However, consistent offsets were found with other identically constructed T-bar tapes. Figure 75 illustrates the cause of the offset to the borehole measurement tape. The average offset $Offset_{\text{avg}}$ for the data is calculated as

$$Offset_{\text{avg}} \text{ (cm)} = \frac{\sum_{n=1}^N (S_{Bn} - S_{Rn})}{N} \quad (65)$$

where N = number of borehole samples

S_{Bn} = borehole thickness measurement (cm)

S_{Rn} = radar thickness measurement (cm).

This yielded an average offset of 1.13 cm for survey study C and 1.52 cm for survey studies G and H. Subse-

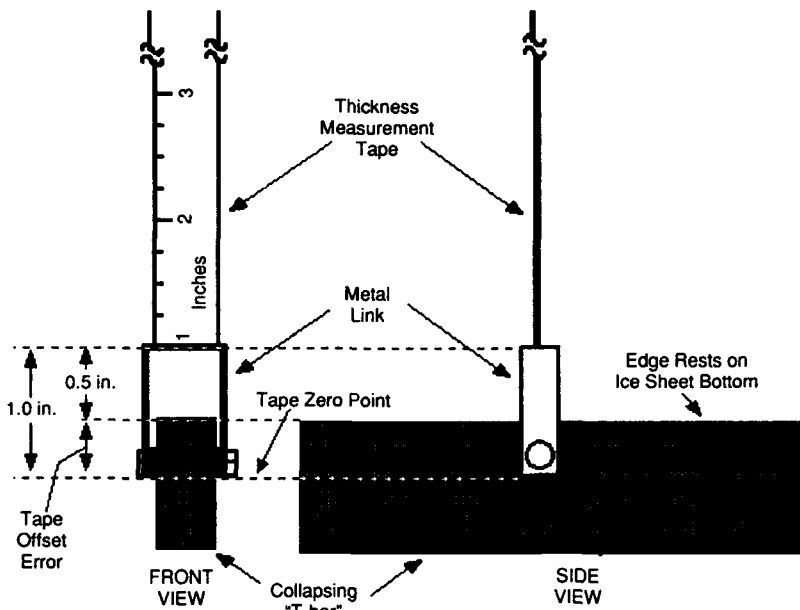


Figure 75. T-bar ice thickness measurement tool with offset indicated.

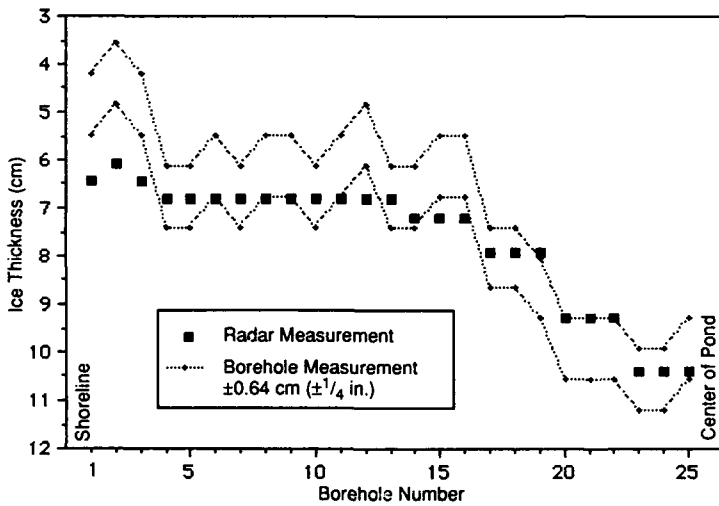


Figure 76. Radar and borehole thickness measurement from tape 6. Dotted line indicates ± 0.64 -cm ruler resolution bounds about borehole measurement.

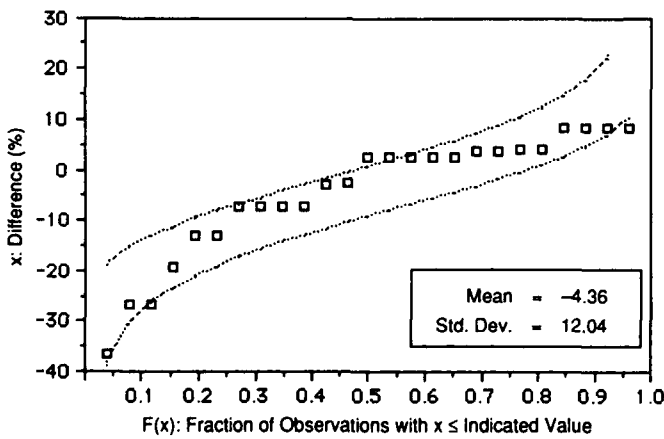


Figure 77. Difference between radar and borehole thickness from tape 6 (95 and 5% confidence bounds shown for normal distribution).

quent analysis was done with these average offsets subtracted from the borehole data.

With the offset corrected data, the percent thickness difference between borehole and radar measurements Dif_n for each borehole-radar data pair was calculated as

$$Dif_n (\%) = \frac{S_{Bn} - S_{Rn}}{S_{Bn}} (100). \quad (66)$$

Figure 76 compares survey study C radar profiling data with a ± 0.64 -cm error-band region bounding the offset-corrected borehole measurements. Here, boreholes were drilled every 1 m along the survey path. With the exception of boreholes 1, 2 and 3, the majority of the radar measurements fall within the resolution bounds of the measurement tape. The error exhibited by the first

three points is possibly caused by variations in the dielectric constant or scattering by bottom grass and other debris imbedded in ice formed over shallow water close to the shoreline. Figure 77 gives an indication of the percent difference (relative to the offset-corrected borehole measurement) Dif_n for the data. Excluding the error data from boreholes 1, 2 and 3, the greatest error is approximately $\pm 10\%$ about the mean.

Figure 78 compares survey study G and H radar profiling data with a ± 0.64 cm error-band region bounding the offset-corrected borehole measurements. Here, boreholes were drilled every 3 m along the survey path. Figure 79 gives an indication of the percent difference Dif_n for the data. With only one exception, the error range is less than $\pm 10\%$. The error for boreholes 29 and 30 is again potentially caused by shoreline effects, as

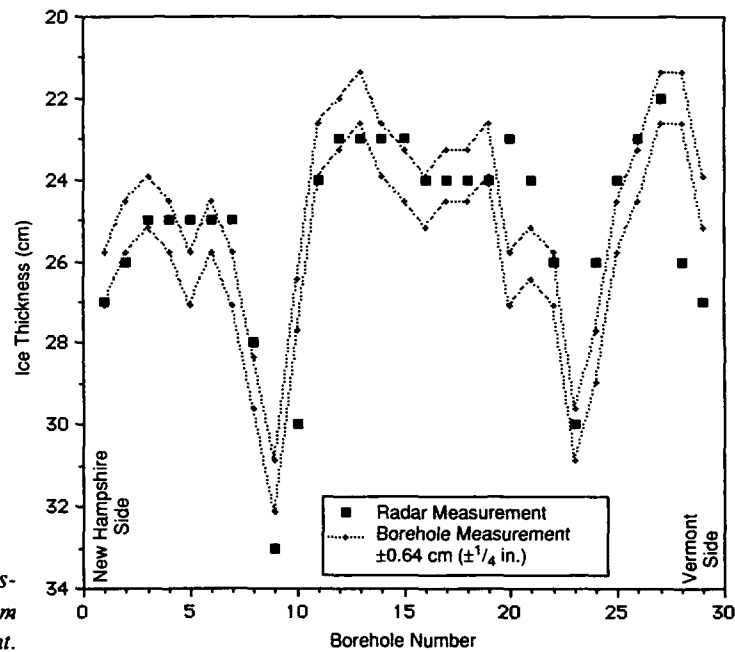


Figure 78. Radar and borehole thickness measurement for tape 11. Dotted line indicates ± 0.64 -cm ruler resolution bounds about borehole measurement.

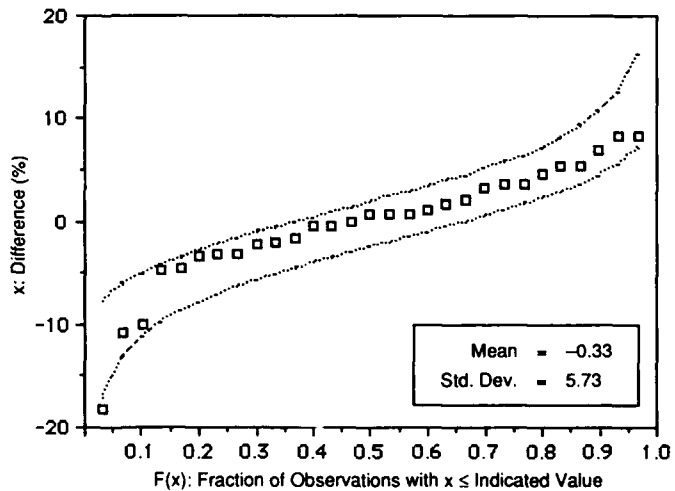


Figure 79. Difference between radar and borehole thickness from tape 11 (95 and 5% confidence bounds shown for normal distribution).

Table 11. Comparison of calculated and measured resolution error.

Survey study	Nominal thickness (cm)	Calculated error (%)	Measured error (%)
C	5	±15.5	≤ ±10
G & H	25	±2.7	≤ ±10

discussed earlier. Error in registration of borehole data with radar thickness may be attributable to nonlinearities in the horizontal displacement on the spectrogram because of varying velocity of the profile vehicle.

Error analysis summary

The radar system resolution error calculations of the *Radar System Resolution Error Analysis* section compare favorably with resolution errors encountered in the radar profiling and borehole thickness measurement data described in the previous section. Table 11 summarizes the calculated and measured error for the nominal ice thicknesses measured.

Radar pulse width analysis

Radar reflection data obtained from a flat metal plate and from natural pond ice were statistically analyzed to look for pulse distortion, which would compromise thickness resolution, and to serve as a baseline for further pulse width and shape analysis. Pulse symmetry can be distorted by the frequency-dependent effects of radar hardware elements, including waveguide, antennas, mixer and analog recorder bandwidth, along with pulse-spreading effects of surface and volume scattering.

Radar reflections from a metal plate

An indication of the limit of realizable thickness resolution can be obtained by measuring the time width of a received radar pulse reflected from a flat metal plate, a situation in which there should be minimal distortion or spreading of the pulse shape results. A 1 × 1-m rectangular metal plate oriented on a center line normal to the antennas at a range of 2 m was employed. For the 9° beamwidth antennas used, the 3-dB footprint diameter is approximately 30 cm.

Pulse width measurements were taken at points 5 and 10 dB below the peak of the reflected pulse. The -5-dB below-peak measurement point was selected because it could be conveniently and repeatedly located, given the nature of the DSP hardware and software, and was within only 1 dB of the below-peak point described in the *Effect of Bandwidth* section (-4 dB) for defining minimum bandwidth resolution. The -10-dB below-peak point was also selected for DSP hardware and software

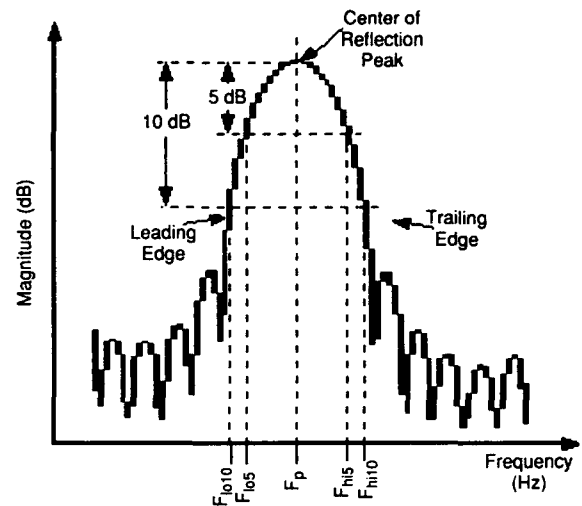


Figure 80. Parameters for analysis of a pulse reflected from a metal plate.

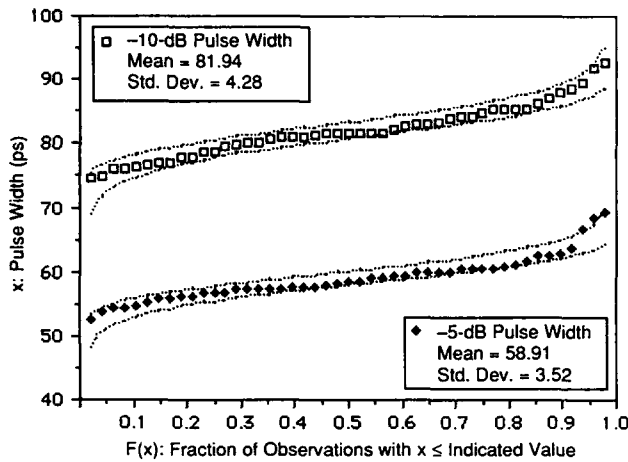
considerations because it was far enough down the skirt of the pulse to give an indication of pulse width spreading, yet substantially above a level that would be influenced by the effects of side lobes or the noise floor. Figure 80 illustrates the parameters used in width and symmetry analysis of a radar pulse reflected from a flat sheet of metal. The parameters are

- F_{lo10} = leading edge -10-dB intercept frequency
- F_{lo5} = leading edge -5-dB intercept frequency
- F_p = pulse peak amplitude intercept frequency
- F_{hi5} = trailing edge -5-dB intercept frequency
- F_{hi10} = trailing edge -10-dB intercept frequency.

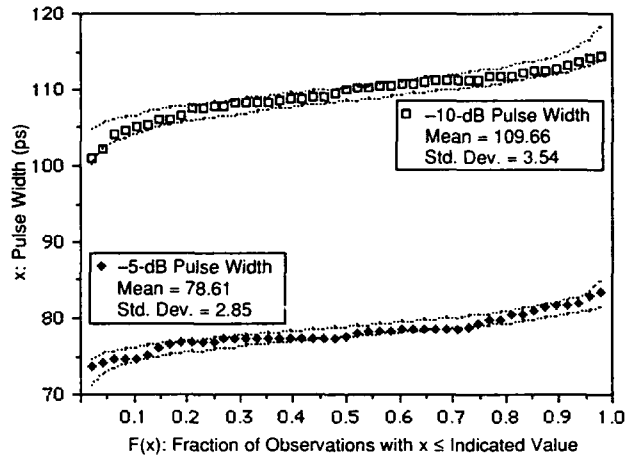
As is normally done in the radar DSP, each scan of the radar reflection data was converted to 1024 digital samples, then zero-padded to 2048 points, windowed appropriately and transformed into a power spectrum. Scans were then individually displayed so that the values of F_{lo10} , F_{lo5} , F_p , F_{hi5} and F_{hi10} could be located on the pulse of interest using a curve-tracking cursor, integral to the DSP hardware and software. Statistical analysis was performed on data extracted from 50 scans.

The frequencies F_{lo10} , F_{lo5} , F_p , F_{hi5} and F_{hi10} are directly related to corresponding one-way travel times from the antennas, T_{lo10} , T_{lo5} , T_p , T_{hi5} and T_{hi10} by eq 29. Differences between these one-way travel times provide pulse width and pulse symmetry information where

$$\begin{aligned}
 T_{hi5} - T_{lo5} &= -5\text{-dB pulse width (ps)} \\
 T_{hi10} - T_{lo10} &= -10\text{-dB pulse width (ps)} \\
 T_{hi5} - T_p &= -5\text{-dB trailing half pulse width (ps)} \\
 T_{hi10} - T_p &= -10\text{-dB trailing half pulse width (ps)} \\
 T_p - T_{lo5} &= -5\text{-dB leading half pulse width (ps)} \\
 T_p - T_{lo10} &= -10\text{-dB leading half pulse width (ps)}.
 \end{aligned}$$



a. Rectangular windowed.



b. Hanning windowed.

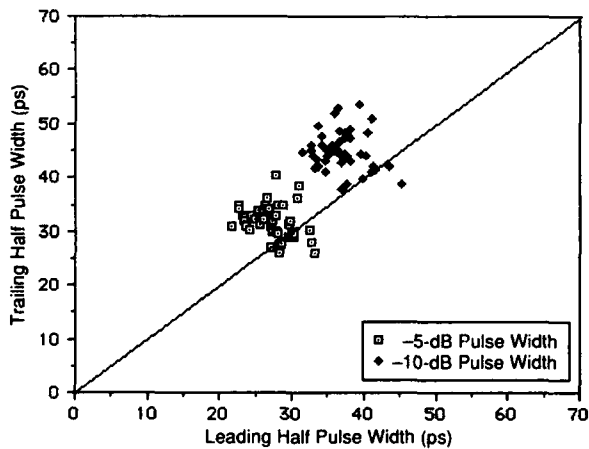
Figure 81. CDF of widths of pulses reflected from a metal plate (95 and 5% confidence bounds shown for normal distribution).

Figure 81 shows Cumulative Distribution Function (CDF) plots illustrating the -5- and -10-dB pulse width data for rectangular and Hanning windowed pulses. Both sets of data appear to conform consistently to a normal distribution, lying within the normal distribution 5 and 95% confidence bounds (dotted lines either side of the data points). The normal (Gaussian) Probability Distribution Function (PDF) $p(x)$ is defined as

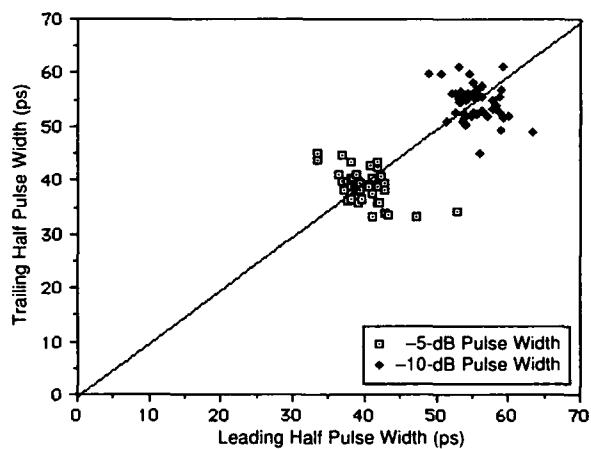
$$p(x) = \frac{1}{\sqrt{2\pi}\sigma_x} \exp\left[-\frac{1}{2}\left(\frac{x - \mu_x}{\sigma_x}\right)^2\right] \quad -\infty < x < \infty \quad (67)$$

where x = real random variable
 μ_x = mean
 σ_x = standard deviation.

Using eq 31 and the mean values for the -5-dB pulse widths of the rectangular and Hanning windowed pulses from Figure 81, we can compute a lower bound on realizable ice thickness resolution of 0.50 cm for rectangular windowing and 0.67 cm for Hanning windowing. The extent of scattering, resulting in a widening of the reflected radar pulse, may have a significant limiting effect on the minimum achievable resolution. Figure 82 illustrates the leading-to-trailing half pulse width asymmetry for rectangular and Hanning windowed pulses. The symmetry of leading and trailing half-pulse widths is described by the diagonal line on the graphs. When rectangularly windowed, the pulse exhibits an asymmetry with a broader trailing half-pulse width; Hanning windowing further broadens the entire pulse and increases the tendency toward symmetry of the leading and trailing pulse halves.

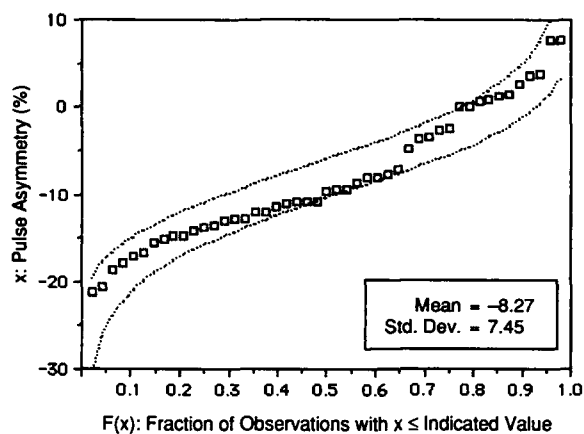


a. Rectangular windowed.

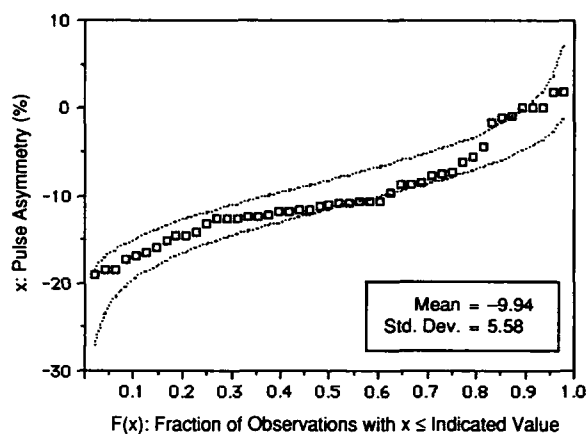


b. Hanning windowed.

Figure 82. Pulse width asymmetry (diagonal line represents locus of perfect symmetry).

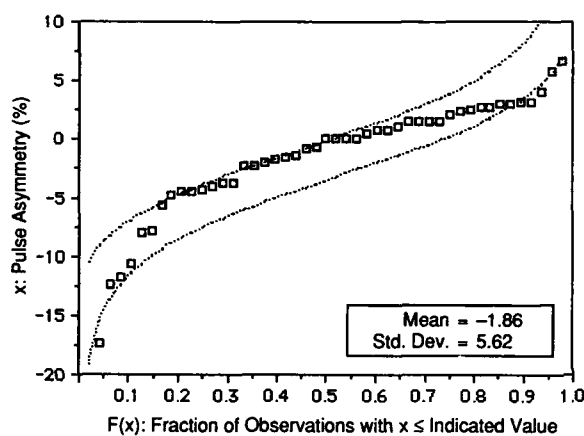


a. -5-dB asymmetry.

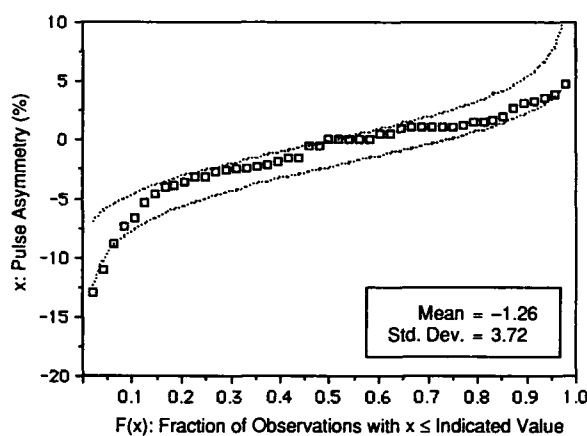


b. -10-dB asymmetry.

Figure 83. CDF of rectangular windowed pulse (%) (95 and 5% confidence bounds shown for normal distribution).



a. -5-dB asymmetry.



b. -10-dB asymmetry.

Figure 84. CDF of Hanning windowed pulse (%) (95 and 5% confidence bounds shown for normal distribution).

The percent of asymmetry A_{sym} is defined for the -5-dB measurement point as

$$A_{sym} (\%) = \frac{(T_{hi5} - T_p) - (T_p - T_{lo5})}{(T_{hi5} - T_{lo5})} (100) \quad (68)$$

and for the -10-dB measurement point as

$$A_{sym} (\%) = \frac{(T_{hi10} - T_p) - (T_p - T_{lo10})}{(T_{hi10} - T_{lo10})} (100) \quad (69)$$

CDFs indicating the statistics of percent asymmetry of the examined radar pulses are illustrated in Figures 83 and 84. The figures show that statistically the rectangular windowed reflections from the metal sheet have an 8-9% half pulse width asymmetry, with the trailing half pulse roll-off less steep. This suggests a low-pass frequency dependence, attributable to either the radar

components, including the antennas and waveguide, or to physical deformations of the thin metal reflector sheet as it lay on the ice surface.

Radar reflections from an ice sheet

The methodology of the previous section was applied to obtain the effects of scattering on pulse width spreading and pulse symmetry for the air/ice and ice/water interface reflections from a sheet of natural pond ice. Figure 85 illustrates the pertinent components of the reflection pulses from both the air/ice and ice/water interfaces used in the analysis. The particular data analyzed (survey study F) were of pond ice nominally 40 cm thick, with minimal surface roughness (see Appendix A for details).

Figure 86 shows CDFs of the air/ice interface reflected pulse widths at the -5- and -10-dB points, while Figure 87 shows CDFs of the ice/water interface reflected pulse widths at the -5- and -10-dB points. Table 12

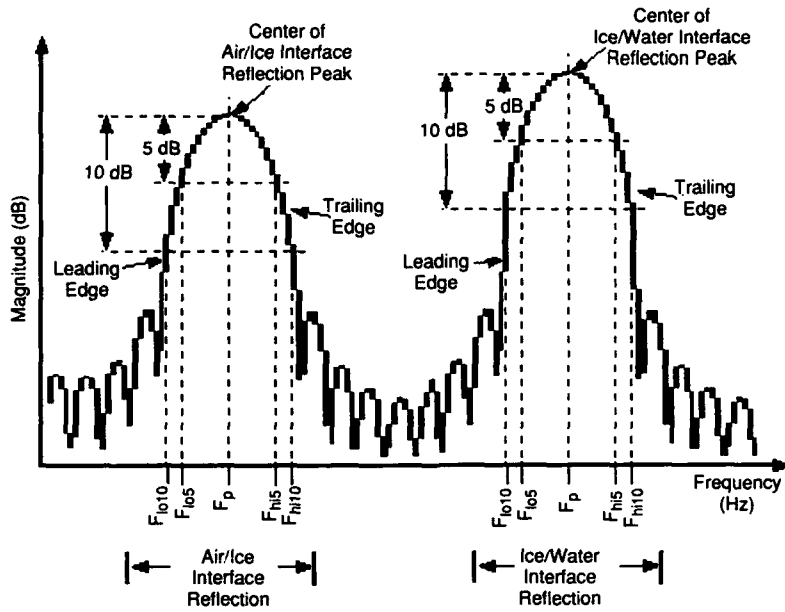
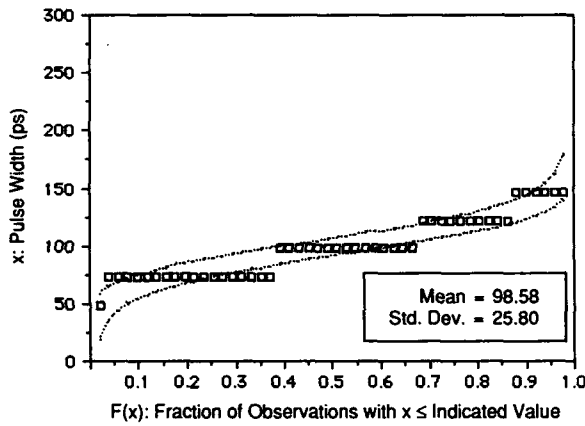
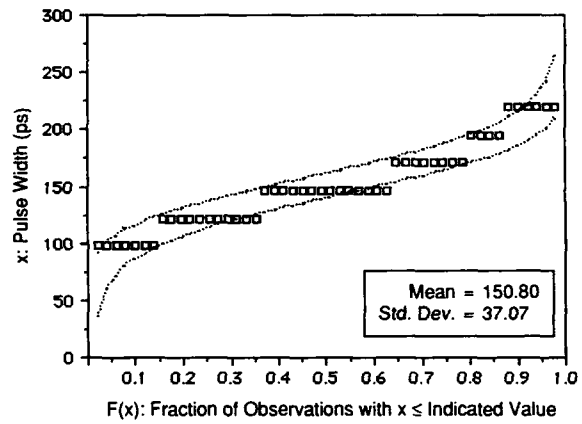


Figure 85. Parameters for analysis of a pulse reflected from an ice sheet.

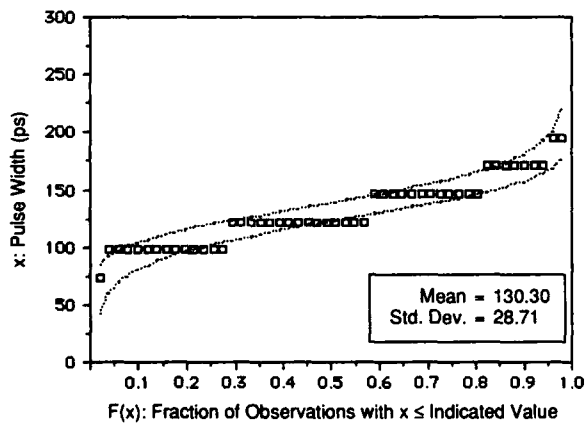


a. At -5-dB point.

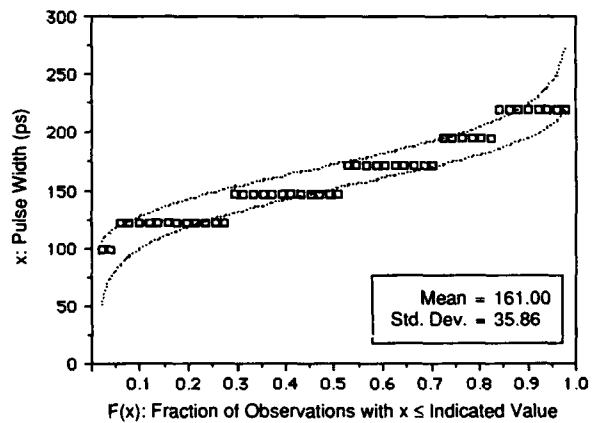


b. At -10-dB point.

Figure 86. CDF of air/ice interface pulse width (95 and 5% confidence bounds shown for normal distribution).



a. At -5-dB point.



b. At -10-dB point.

Figure 87. CDF of ice/water interface pulse width (95 and 5% confidence bounds shown for normal distribution).

Table 12. Comparison of mean pulse widths at -5- and -10-dB measurement points.

Reflecting boundary	Window type	Mean pulse width (ps)	
		-5-dB point	10-dB point
Metal plate	Rectangular	58.91	81.94
Metal plate	Hanning	78.61	109.66
Air/ice interface	Hanning	98.58	150.80
Ice/water interface	Hanning	130.30	161.00

compares the -5- and -10-dB pulse widths of reflections from a metal plate with the air/ice and ice/water interfaces. The pulse widens significantly when it is scattered by surface roughness at the air/ice interface. Additionally, the pulse widens when it is reflected from the ice/water interface because of two scattering events at the air/ice interface (in and out), the effects of volume scattering, and scattering ascribable to roughness at the ice/water interface.

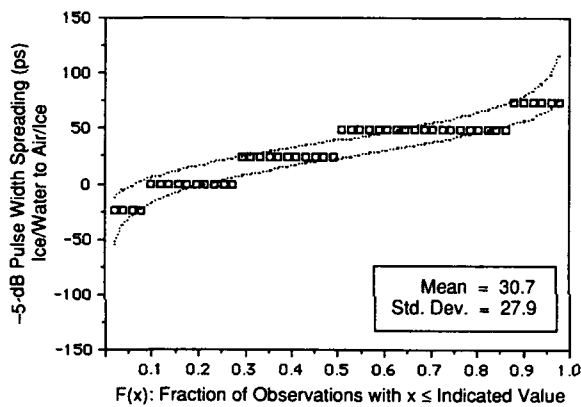
Pulse width spreading can also be characterized in terms of the pulse width difference between the ice/water and air/ice interfaces ΔW (ps) at the -5-dB and -10-dB measurement points by the relation

$$\Delta W = W_{I/W} - W_{A/I} \quad (70)$$

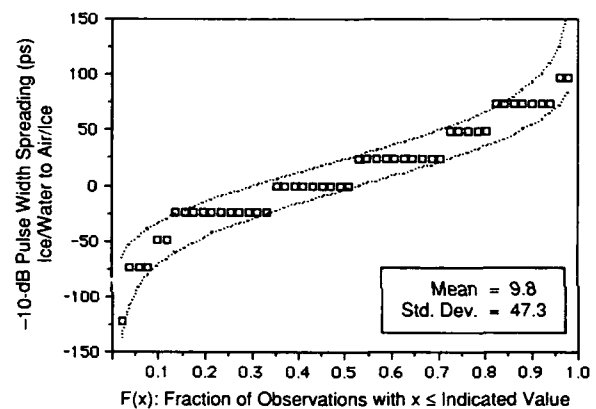
where $W_{I/W}$ is the ice/water reflection pulse width (ps) and $W_{A/I}$ is air/ice reflection pulse width (ps). Figure 88 gives the CDFs of the pulse width differences, relative to the air/ice interface pulse width, measured at the -5- and -10-dB points.

The percentage of pulse width increase exhibited by the pulse reflected from the ice/water interface compared with that from the air/ice interface ΔPW is characterized by

$$\Delta PW (\%) = \left(\frac{\Delta W}{W_{A/I}} \right) (100). \quad (71)$$

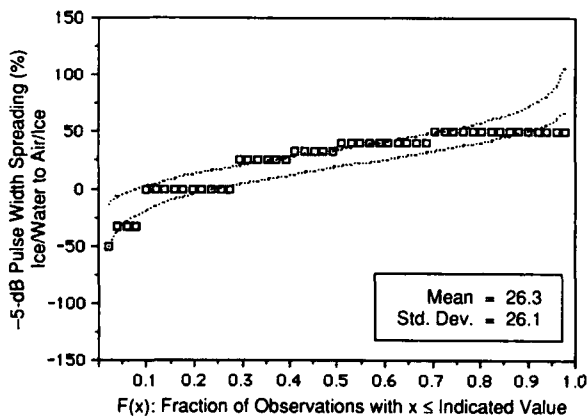


a. At -5-dB point.

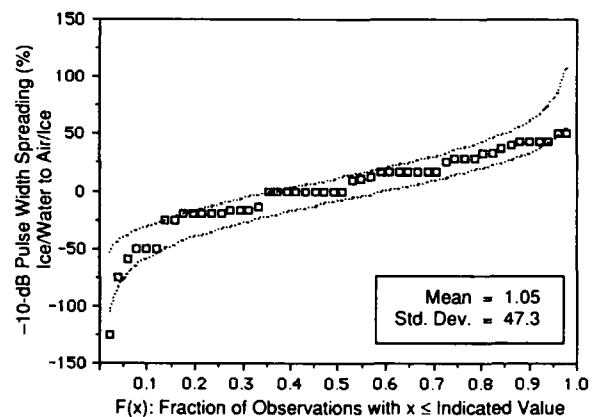


b. At -10-dB point.

Figure 88. CDF of pulse width difference between first and second interface reflected pulses (95 and 5% confidence bounds shown for normal distribution).



a. At -5-dB point.



b. At -10-dB point.

Figure 89. CDF of pulse width spreading (%) between first and second interface reflections (95 and 5% confidence bounds shown for normal distribution).

Figure 89 gives the CDFs of the percentage pulse width differences, relative to the air/ice interface pulse width, measured at the -5 -dB and -10 -dB points. The figures show that at the -5 -dB measurement point the ice/water reflection return is, on average, 30 ps or 26% wider relative to the associated air/ice interface return reflection. It is believed that this is caused by volume scattering in the ice as well as by "surface" scattering at the ice/water boundary.

The pulse asymmetry may lead to a degree of ambiguity or measurement error when measuring ice thickness based on the location of interface boundary reflection pulse peaks. Here, pulse asymmetry is examined to determine the extent of this ambiguity. Pulse width symmetry between the leading and trailing half pulse widths was measured for the air/ice and ice/water re-

flexion pulses at the -5 - and -10 -dB points by methods earlier discussed. Figure 90 illustrates the asymmetry between the leading and trailing -5 - and -10 -dB half-pulse widths for the reflected pulse from the air/ice and ice/water interfaces. CDFs of the difference between the leading and trailing half pulse widths at the -5 -dB measurement point for reflections from both the air/ice and ice/water interfaces are shown in Figure 91. Here, the mean pulse width asymmetry is 3.42 ps for the pulse reflected from the air/ice interface and 11.71 ps for the pulse reflected from the ice/water interface. The worst-case -5 -dB pulse asymmetry spread is approximately ± 50 ps. If ambiguity in pulse peak location is assumed to be half of the mean asymmetry of the ice/water interface, approximately 6 ps, then the associated thickness measurement error in ice would be approximately 0.10

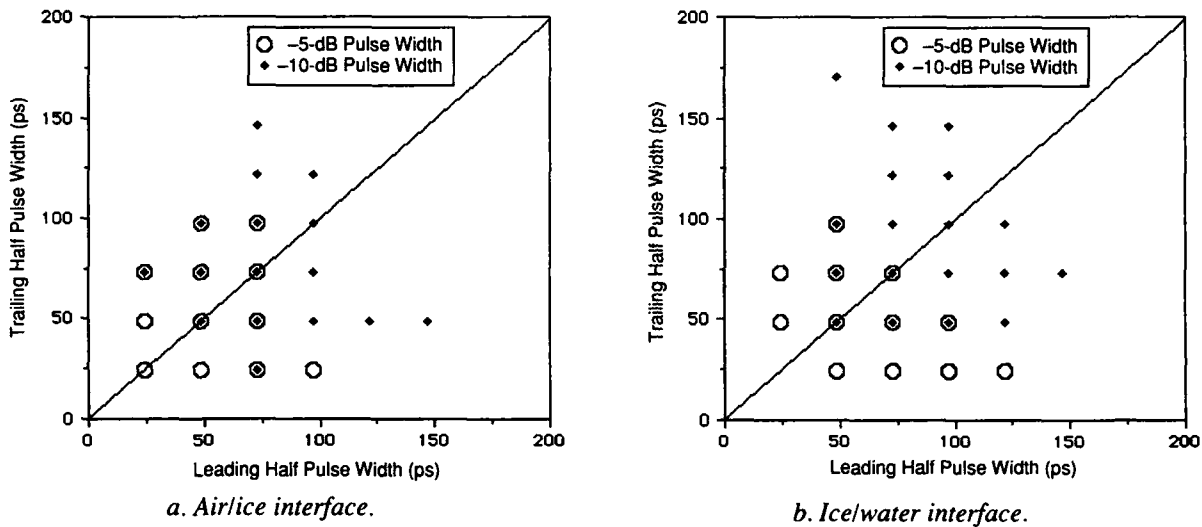


Figure 90. Pulse width asymmetry (diagonal line represents locus of perfect symmetry; sample size = 50).

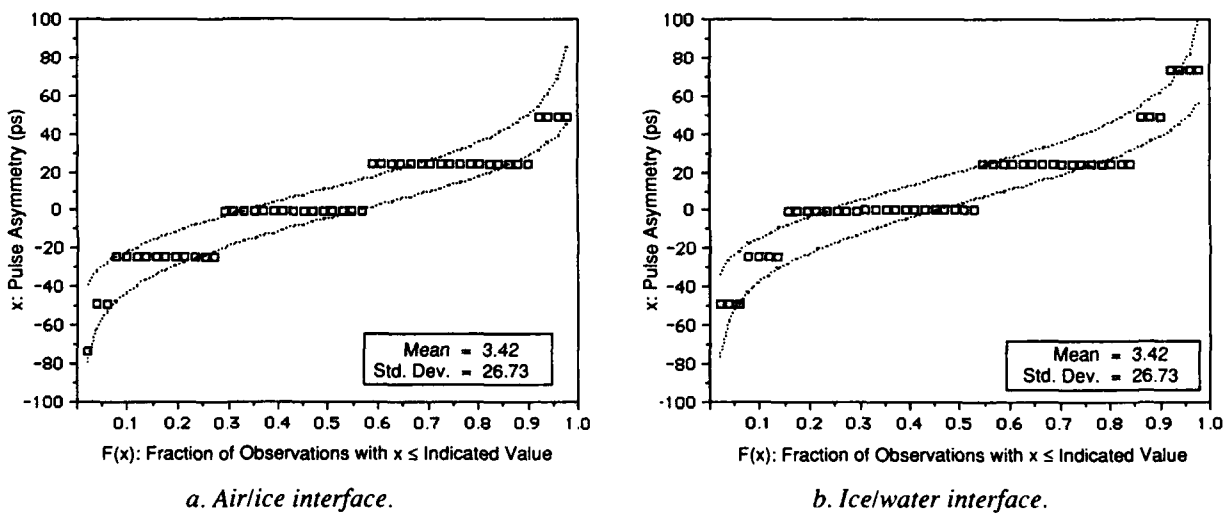
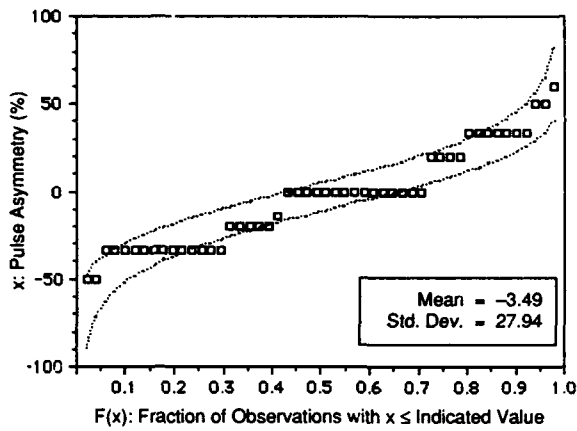
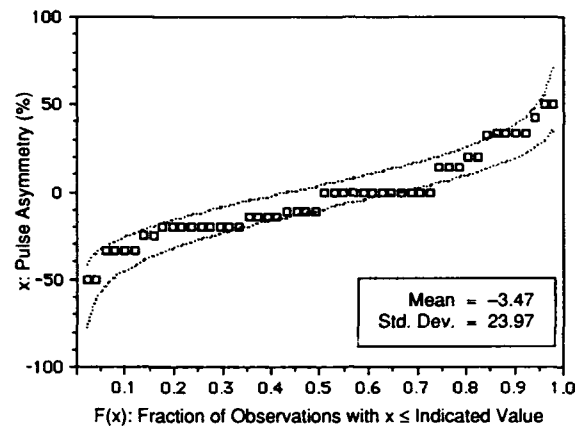


Figure 91. CDF of pulse width asymmetry (ps) at -5 -dB point (95 and 5% confidence bounds shown for normal distribution).

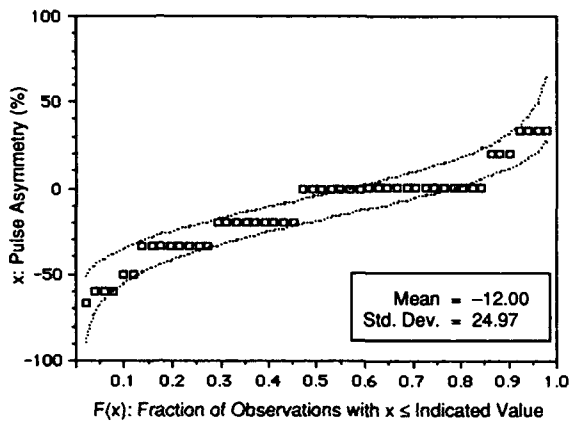


a. At -5-dB point.

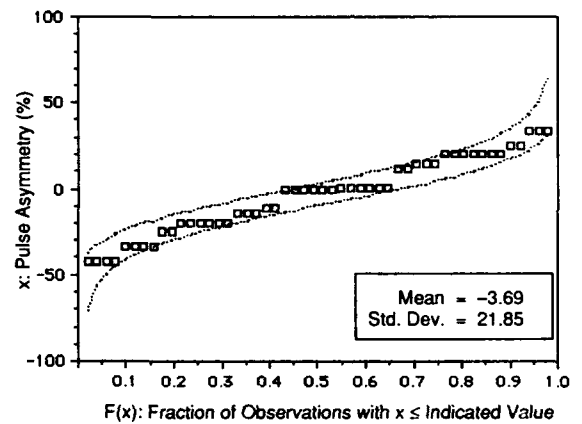


b. At -10-dB point.

Figure 92. CDF of air/ice pulse width asymmetry (%) (95 and 5% confidence bounds shown for normal distribution).



a. At -5-dB point.



b. At -10-dB point.

Figure 93. CDF of ice/water pulse width asymmetry (%) (95 and 5% confidence bounds shown for normal distribution).

cm, significantly below the calculated thickness resolution of the system R_{res} . Even with half of the worst-case spread, 25 ps, the associated thickness measurement error would be 0.42 cm, still less than the minimum resolution.

Percent asymmetry A_{sym} is described for the air/ice interface reflected pulse by the CDFs of Figure 92 and for the ice/water interface reflected pulse by the CDFs of Figure 93. Table 13 compares the mean pulse asymmetry for the metal plate, air/ice and ice/water reflection

Table 13. Comparison of mean pulse asymmetry at -5- and -10-dB measurement points.

Reflecting boundary	Window type	Mean pulse asymmetry (%)	
		-5 dB	-10 dB
Metal plate	Rectangular	-8.27	-9.94
Metal plate	Hanning	-1.86	-1.26
Air/ice	Hanning	-3.49	-3.47
Ice/water	Hanning	-12.00	-3.69

boundary data. A negative percent asymmetry indicates that the trailing half pulse width is wider than the leading half pulse. The asymmetry is less apparent for the Hanning windowed pulses at the -10-dB measurement point because of the widening of the leading and trailing pulse halves relative to their difference in width.

Table 13 shows only a slight difference in the -5-dB-point asymmetry between Hanning windowed pulses reflected from a metal plate or from the air/ice boundary. However, an order of magnitude greater mean asymmetry is apparent when comparison is made to the pulse reflected from the ice/water interface. Given the slight increase in asymmetry because of reflection from the air/ice boundary, it appears that the asymmetry of the pulse reflected from the ice/water boundary is primarily attributable to frequency-dependent volume scattering by entrapped air bubbles or by the effects of "surface" scattering at the ice/water boundary itself. Since the pond was smooth, relative to the Rayleigh smoothness criteria (Eaves and Reedy 1987), it is believed that

volume scattering dominated in this study. Several features in the ice core (Fig. 57) from this study support this conclusion, including a granular, saturated refrozen snow layer and three distinct bands of air bubbles.

Statistical analysis of radar pulse peak magnitude

The peak magnitude of reflected pulses from the air/ice boundary, the ice/water boundary and the difference between the two were examined to see if electromagnetic properties of ice, such as dielectric loss, could be directly determined from the radar data. In all the ice data scans examined, coherent reflections were observed in that the pulse shape was similar to those reflected from a flat metal plate despite the variability (to be discussed) in pulse width and magnitude. Pulses were never stacked (because of altitude fluctuations), so that the coherence seen in the pulse shapes of the spectrogram are essentially that of the windowed data.

Figure 94 indicates the attributes of the Fourier transformed FM-CW radar difference frequency output signal used in the analysis. The peak values of the air/ice interface dB_1 and the ice/water interface dB_2 as well as their associated spectral frequencies, F_{r1} and F_{r2} , were determined for a sequence of radar scans from each data tape. To obtain these data, survey tapes were digitally signal processed by converting each scan into 1024 digital samples. Each sampled scan was zero-padded to 2048 points, Hanning windowed and transformed into a power spectrum. Scans were individually displayed and the values of dB_1 , dB_2 , F_{r1} and F_{r2} were located using a curve-tracking cursor, integral to the DSP hardware and software. Data collected from 100 such scans from within a given profiling survey were then statistically analyzed.

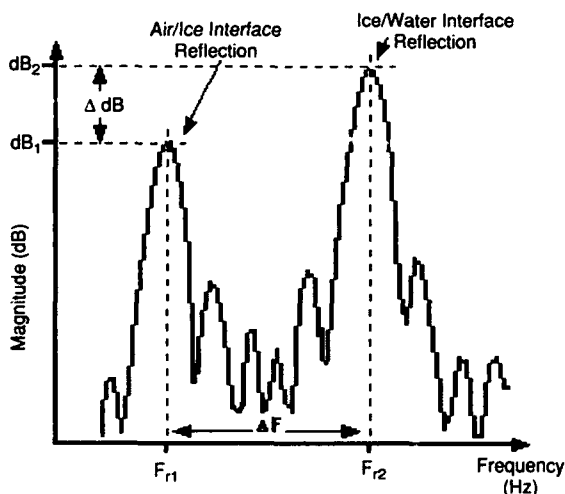
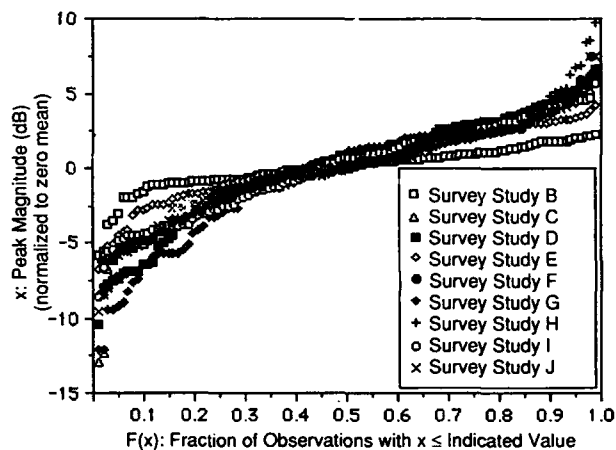


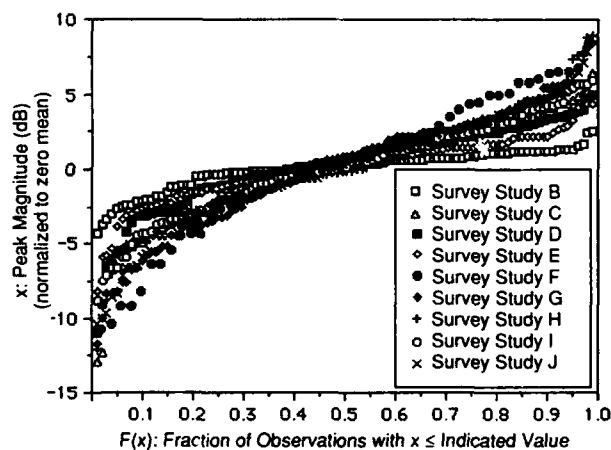
Figure 94. Representation of FM-CW radar waveform components used for statistical analysis.

The values of F_{r1} and F_{r2} are directly related to radar range and ice thickness by eq 29 and 30. Radar range and range-gain normalization were applied to the data so that direct scan-to-scan comparisons could be made and CDFs generated.

Figures 95 and 96 compare CDFs of reflection peak magnitude data from the air/ice and ice/water interfaces and a CDF of the peak magnitude difference between the first and second interface. They were generated as described in the *Cart-mounted Profiling of Overflow Pond* section. They represent data from nine selected ice thickness surveys exhibiting unique ice conditions (e.g., surface roughness, snow cover or thickness) or measurement vehicle configurations (e.g., cart, truck or helicopter), or both. Specific details of each of these surveys are documented in Appendix A. Here, for convenience of comparison and clarity, the data have been normalized to a zero mean and each data set appears reasonably well-bounded by the 5 and 95% confidence



a. Air/ice interface.



b. Ice/water interface.

Figure 95. CDF of peak magnitudes (zero-mean normalized).

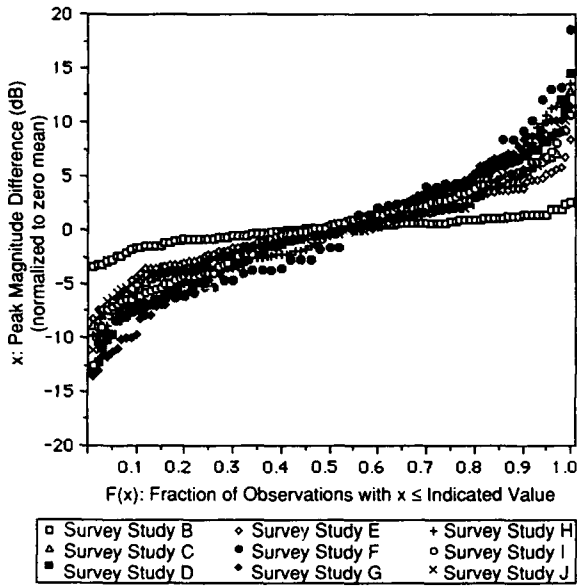


Figure 96. CDF of peak magnitude differences between air/ice and ice/water interface (zero-mean normalized).

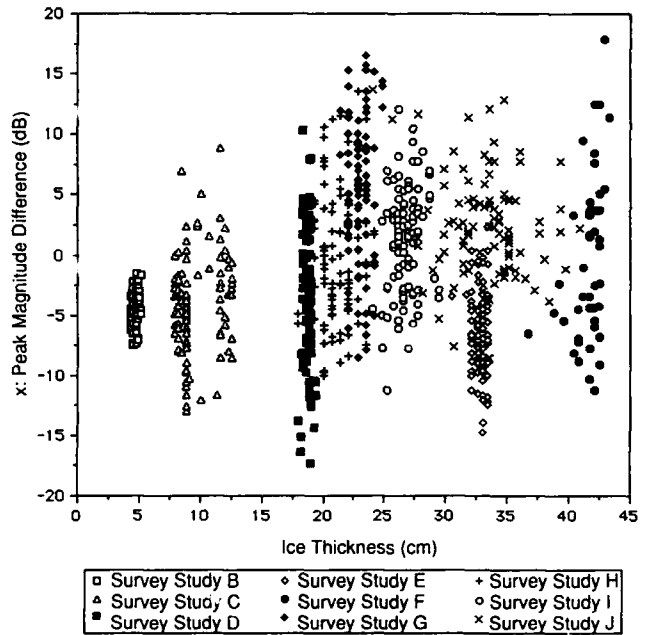


Figure 97. Summary of ice thickness vs peak magnitude difference.

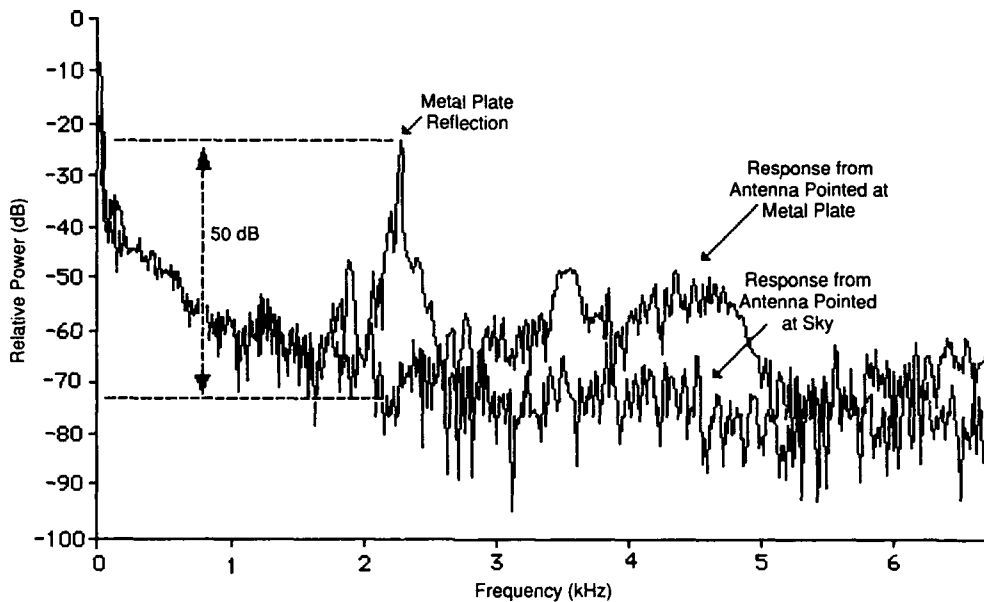


Figure 98. Overlay plot of radar system responses to a metal plate and sky, indicating an approximate 50-dB SNR.

bands of a log-normal distribution (see Appendix A for individual survey details). The peak magnitudes' CDFs of Figure 95 show a variability on the order of 25 dB, while for the CDF displayed in Figure 96 there is a maximum peak variability on the order of 35 dB.

Figure 97 is a compilation of ice thickness vs peak magnitude differences for data from all analyzed surveys. There is approximately a 35-dB range of peak magnitude difference, which does not appear to be a

function of ice thickness nor have a statistically consistent tendency for the first interface pulse magnitude to be larger (or smaller) than the second across the entire range of data. Thus, it appears that ϵ'' cannot be reliably deduced from the data. Surface roughness at both the air/ice and ice/water interfaces has a significant effect on the variability of pulse amplitudes, pulse width and pulse asymmetry. Finally, Table 14 summarizes the statistics data from all surveys analyzed.

Table 14. Summary of pulse peak magnitudes survey data.

Survey study	Tape no.	Platform	Speed (km/hr)	Radar range (m)	Ice type	Ice thickness (cm)	Air temperature (°C)	Ice surface conditions	Sample size	Measurement (dB)	Mean (dB)	Std. dev.
B	2	Stationary	0	2	Pond	5	2	Clear ice, minimal surface roughness	100	Air/ice peak Ice/water peak A/I - I/W	-38.12 -33.99 -4.12	1.46 1.29 1.24
C	6	Cart	3	1	Pond	7-8	-5	Snow cover shoveled clear; minimal surface roughness	100	Air/ice peak Ice/water peak A/I - I/W	-26.33 -26.33 -4.15	3.48 3.48 4.08
D	7	Cart	1	1	Pond	20-25	-10	Smooth ice with <1 cm of snow cover	100	Air/ice peak Ice/water peak A/I - I/W	-36.85 -32.81 -4.17	3.70 2.82 5.44
E	9	Truck	10	1	Pond	30	-7	18 cm dry, low-density snow cover over ice with minimal surface roughness	100	Air/snow peak Snow/ice peak Ice/water peak A/S - S/I S/I - I/W	-36.42 -30.38 -26.46 -3.69 -6.29	2.74 2.32 2.22 3.36 3.30
F	10	Truck	10	2	Pond	35-40	-18	≤1 cm snow cover with roughened texture from refrozen meltwater	50	Air/ice peak Ice/water peak A/I - I/W	-22.30 -21.82 -0.72	3.09 4.82 6.67
G	11a	Cart	3	5-6	River	25-35	-12	Clear ice; minimal surface roughness	100	Air/ice peak Ice/water peak A/I - I/W	-21.73 -27.21 5.13	4.60 4.28 6.05
H	11b	Cart	3	5-6	River	25-35	-12	Surface roughness ≤1 cm from refrozen snowplow ejecta on ice surface	100	Air/ice peak Ice/water peak A/I - I/W	-30.62 -30.53 -0.10	3.54 3.68 5.41
I	13	Helicopter	15	3-5	Pond	30	>5	Smooth ice with patches of <1 cm of wind-packed snow cover	100	Air/ice peak Ice/water peak A/I - I/W	-30.33 -31.72 1.38	3.09 3.31 4.48
J	14	Helicopter	15	3-5	River	30	>5	Smooth ice with patches of ≤1 cm of wind-packed snow cover	100	Air/ice peak Ice/water peak A/I - I/W	-38.93 -41.61 2.64	3.26 4.04 4.18

System noise analysis

The SNR performance of the prototype radar system was determined experimentally and compared with values calculated by the method described in the *Radar Range Equation for Geophysical Application* section. Radar reflection data from a normally positioned metal plate of known dimension and at a known range were compared with radar reflection data obtained by pointing the antennas skyward. The system was configured identically for both measurements. The flat metal sheet target at a known distance provides a relative indication of power returned from a smooth reflecting surface.

Table 15. Comparison of calculated and prototype system SNR.

Range (m)	Calculated SNR	Prototype system SNR
1.5	65.5	50
3.0	59.4	44 *
6.0	53.5	38 *

* Values calculated based on -6-dB SNR change for a doubling of range.

Pointing the antenna toward the sky eliminates the effects of nearby targets on the radar signal. The remaining signal components are from the noise and reflections internal to the receiver itself and serve as an indication of the system noise floor. The radar data were acquired directly by the Macintosh II computer and DSP coprocessor for processing and display, thus avoiding additional incurred noise from an analog or DAT magnetic tape recording and playback process. Comparing the two measurements gives an estimate of the system SNR. Figure 98 indicates about a 50-dB SNR for the prototype radar system when a 45- x 55-cm aluminum plate ($\rho_1 = 1$) was placed 150 cm from the antenna and an output power level of 13 dBm was used. Table 15 compares prototype system experimental results with theoretical SNR using eq 47 and shows that the SNR decreases by 6 dB for each doubling of radar range.

CONCLUSIONS AND RECOMMENDATIONS

Accurate helicopter-borne, high-speed, high-resolution continuous profiling of freshwater ice and snow thickness is possible at MMW wavelengths. The mini-

imum thickness resolution capability with a 13.5-GHz bandwidth radar was significantly below the thinnest measured ice (3 cm). Warming ice, high water content ice and snow, and surface meltwater inhibit profiling capability at millimeter wavelengths. Profiling accuracy, compared to borehole measurements, was approximately $\pm 10\%$. Based on an examination of the width and shape of pulses reflected from metal plates, air/ice and ice/water boundaries, it appears that the pulse spreading is caused primarily by surface scattering. The degree of ice surface roughness, and resulting radar scattering encountered, did not inhibit thickness profiling of cold, natural, freshwater ice and snow over a range of 5 cm to 40 cm. Volume scattering from air bubbles (typically less than 1 mm diameter) trapped within natural freshwater ice did not inhibit profiling capability nor noticeably affect thickness measurement accuracy. However, volume scattering along with "surface" scattering at the ice/water boundary appear to play a significant role in increasing the asymmetry between leading and trailing half pulse widths, which may contribute to thickness measurement errors for very thin (less than 3 cm) ice. Direct determination of the bulk dielectric loss of an ice sheet from the profiling data is not feasible owing to the 30- to 35-dB variation in air/ice and ice/water peak magnitude and peak differential magnitudes encountered in the data.

The primary focus of this research effort has been on cold, dry, freshwater ice and low density snow. The ability to obtain rapidly and interpret reliably MMW radar ice profiling data from a wider variety of snow and ice surface conditions should be pursued. Additional detailed studies of surface and volume scattering at MMW frequencies exploring the effects of dielectric interface boundary and air bubble inclusions in the ice matrix on reflected pulse width and symmetry distortion should be conducted. Incorporation of continuous real-time FM-CW radar profiling of ice and snow and scattering at an additional microwave band or in a simultaneous dual frequency band arrangement would improve profile acquisition and interpretation, especially for thicker ice and severe snow covers. Removing altitude variability effects by implementation of a real-time range normalization algorithm within the DSP software would aid in interpretation of airborne survey data.

LITERATURE CITED

- Annan, A.P. and J.L. Davis** (1977a) Impulse radar applied to ice thickness measurements and freshwater bathymetry. Geological Survey of Canada, Resource Geophysics and Geochemistry Division, Paper 77-1B.
- Annan, A.P. and J.L. Davis** (1977b) Radar range analysis for geological materials. Geological Survey of Canada, Resource Geophysics and Geochemical Division, Paper 77-1B.
- Arcone, S.A.** (1984) Field observations of electromagnetic pulse propagation in dielectric slabs. *Geophysics*, **49**(10): 1763-1773.
- Arcone, S.A.** (1985) Radar profiling of ice thickness. USA Cold Regions Research and Engineering Laboratory, Cold Regions Technical Digest 85-1.
- Arcone, S.A. and A.J. Delaney** (1987) Airborne river-ice thickness profiling with helicopter-borne UHF short-pulse radar. *Journal of Glaciology*, **33**(115): 330-340.
- Arcone, S.A., A.J. Delaney and D.J. Calkins** (1989) Water detection in the coastal plains of the Arctic National Wildlife Refuge using helicopter-borne short pulse radar. USA Cold Regions Research and Engineering Laboratory, CRREL Report 89-7.
- Arcone, S.A., A.J. Delaney and R.E. Perham** (1986) Short-pulse radar investigations of freshwater ice sheets and brash ice. USA Cold Regions Research and Engineering Laboratory, CRREL Report 86-6.
- Auston, D.H. and M.C. Nuss** (1988) Electro-optic generation and detection of femtosecond electrical transients. *IEEE Journal of Quantum Electronics*, **24**(2): 184-197.
- Avtech Corp.** (1989) Nanosecond waveform generators. Ogdensburg, New York.
- Barton, D.K.** (1988) *Modern Radar System Analysis*. Norwood, Massachusetts: Artech House, Inc.
- Blue, M.D.** (1980) Permittivity of ice and water at millimeter wavelengths. *Journal of Geophysical Research*, **85**(c2): 1101-1106.
- Brekhovskikh, L.M.** (1980) *Waves in Layered Media*. New York: Academic Press.
- Brookner, E.** (1988) *Aspects of Modern Radar*. Norwood, Massachusetts: Artech House, Inc.
- Butt, K.A. and B. Gamberg** (1979) Technology of an airborne impulse radar for sounding sea ice. In *Proceedings of the International Workshop on the Remote Estimation of Sea Ice Thickness, St. John's, Newfoundland, Canada*, p. 385-412.
- Chudobiak, W.J., R. Gray and J.S. Wight** (1978) A nanosecond impulse X-band radar. *Proceedings of the IEEE*, **66**(4): 523-524.
- Chudobiak, W.J., R.B. Gray, R.O. Ramseier, V. Mai-kos, M. Vant, J.L. Davis and J. Katsube** (1974) Radar remote sensors for ice thickness and soil moisture measurements. In *Proceedings of Second Canadian Symposium on Remote Sensing, Guelph, Ontario*, p. 417-424.
- Cooper, D.W., R.A. Mueller and R.J. Schertler** (1976a) Measurement of lake ice thickness with a short-pulse radar system. Washington, D.C.: National Aeronautics and Space Administration, Lewis Research Center, NASA TN D-8189.

- Cooper, D.W., R.A. Mueller and R.J. Schertler** (1976b) Remote profiling of lake ice using an S-band short-pulse radar aboard an all-terrain vehicle. *Radio Science*, **11**(4): 375–381.
- Cooper, D.W., J.E. Heighway, D.F. Shook, R.J. Jirberg and R.S. Vickers** (1974) Remote profiling of lake ice thickness using a short pulse radar system aboard a C-47 aircraft. Washington, D.C.: National Aeronautics and Space Administration, NASA TM X-71588.
- Cummings, W.A.** (1952) The dielectric properties of ice and snow at 3.2 centimeters. *Journal of Applied Physics*, **23**(7): 68–773.
- Currie, N.C. and C.E. Brown** (1987) *Principles and Applications of Millimeter-Wave Radar*. Norwood, Massachusetts: Artech House, Inc.
- Daly, S.F. and S.A. Arcone** (1989) Airborne radar survey of a brash ice jam in the St. Clair River. USA Cold Regions Research and Engineering Laboratory, CRREL Report 89-2.
- Eaves, J.L. and E.K. Reedy** (1987) *Principles of Modern Radar*. New York: Van Nostrand Reinhold Co.
- Ellerbruch, D.A. and H.S. Boyne** (1980) Snow stratigraphy and water equivalence measured with an active microwave system. *Journal of Glaciology*, **26**(94): 225–233 1980.
- Frankenstein, G.E.** (1966) Strength of ice sheets. In *Proceedings of Conference on Ice Pressures Against Structures, 10–11 November, Laval University, Quebec, Canada*, p. 79–87.
- Gold, L.W.** (1971) Use of ice covers for transportation. *Canadian Geotechnical Journal*, **170**(8): 170–181.
- Gow, A.J. and D. Langston** (1977) Growth history of lake ice in relation to its stratigraphic, crystalline and mechanical structure. USA Cold Regions Research and Engineering Laboratory, CRREL Report 77-1.
- Gubler, H. and M. Hiller** (1984) The use of microwave FMCW radar in snow and avalanche research. *Cold Regions Science and Technology*, **9**: 109–119.
- Gubler, H., M. Hiller and R.A. Schmidt** (1985) Technical note: FMCW-radar for snow cover investigations. Institut Federal Pour l'Etude de la Neige et des Avalanches—Weissfluhjoch-Davos, Interner Bericht Nr. 627.
- Hallikainen, M.T., F.T. Ulaby and M. Abdelrazik** (1986) Dielectric properties of snow in the 3- to 37-GHz range. *IEEE Transactions on Antennas and Propagation*, **AP-34**(11): 1329–1340.
- Hallikainen, M.T., F.T. Ulaby and R. van Deventer** (1967) Extinction coefficient of dry snow at microwave and millimeterwave frequencies. In *Proceedings of IGARSS '87 Symposium, Ann Arbor, Michigan*, p. 859–864.
- Hayt, W.H.** (1967) *Engineering Electromagnetics*. New York: McGraw-Hill.
- Hickman, G.D. and J.A. Edmonds** (1983) A review of technology for sensing ice characteristics. A technical report for the ONR. Arlington, Virginia: Applied Science Technology, Inc., Report No. AST-R-200183.
- Jakkula, P., P. Ylinen and M. Tiuri** (1980) Measurement of ice and frost thickness with an FM-CW radar. In *Proceedings of 10th European Microwave Conference, Warsaw, Poland, 8–12 September*, p. 584–587.
- Jezeq, K.C., S.S. Arcone, S. Daly and R. H. Wills** (1988) Impulse radar studies of interface roughness. In *Proceedings of 3rd International Workshop on Ground Penetrating Radar, Ottawa, Canada*. Department of Mines, Energy and Resources.
- Kay, S.M.** (1988) *Modern Spectral Estimation*. Englewood Cliffs, New Jersey: Prentice Hall.
- King, R.J.** (1978) *Microwave Homodyne Systems*. Stevenage, England: Southgate House.
- Landau, L.D. and E.M. Lifshitz** (1960) *Electrodynamics of Continuous Media. 8: Course of Theoretical Physics*. Pergamon Press (translated from Russian by J.B. Sykes and J.S. Bell).
- Matzler, C. and U. Wegmuller** (1987) Dielectric properties of fresh-water ice at microwave frequencies. *Journal of Physics D: Applied Physics*, **20**: 1623–1630 1987.
- Morey, R.M.** (1974) Continuous subsurface profiling by impulse radar. In *Proceedings of Engineering Foundation Conference on Subsurface Exploration for Underground Excavation and Heavy Construction, Heniker, New Hampshire, 11–16 August*. New York: American society of Civil Engineers, p. 213–232.
- Nelson, S.O., D.P. Lindroth and R.L. Blake** (1989) Dielectric properties of selected minerals at 1 to 22 GHz. *Geophysics*, **10**(54): 1344–1349.
- Nevel, D.E. and A. Assur** (1968) Crowds on ice. USA Cold Regions Research and Engineering Laboratory, Technical Report 204.
- Oppenheim, A.V. and R. W. Schafer** (1975) *Digital Signal Processing*. Englewood Cliffs, New Jersey: Prentice Hall.
- Paulter, N.G.** (1988) High-speed optoelectronic pulse generation and sampling systems. *IEEE Transactions on Instrumentation and Measurement*, **37**(3): 449–453.
- Paulter, N.G., D.N. Sinha, A.J. Gibbs and W.R. Eisenstadt** (1988) Optoelectronic measurement of picosecond electrical pulse propagation in coplanar waveguide transmission lines. *IEEE Transactions on Microwave Theory and Techniques*, **37**(10): 1612–1619.
- Paulus, P., L. Stoll and D. Jager** (1987) Optoelectronic pulse compression of microwave signals. *IEEE Transactions on Microwave Theory and Techniques*, **MTT-35**(11): 1014–1018.
- Ray, P.S.** (1972) Broadband complex refractive indices of ice and water. *Applied Optics*, **11**(8): 1836–1843.

- Ridenour, L.N.** (1947) *Radar System Engineering*. New York: McGraw Hill.
- Riek, L.** (1988) A signal processing algorithm for the extraction of thin freshwater-ice thickness from short pulse radar data. Masters Thesis, Thayer School of Engineering, Dartmouth College, Hanover, New Hampshire (unpublished).
- Riek, L., R.K. Crane and K. O'Neill** (1990) A signal-processing algorithm for the extraction of thin freshwater-ice thickness from short pulse radar data. *IEEE Transactions on Geoscience and Remote Sensing*, **28**(1): 137–143.
- Rossiter, J.R., K.A. Butt, J.B. Gamberg and T.F. Ridings** (1980) Airborne impulse radar sounding of sea ice. In *Proceedings of Sixth Canadian Symposium on Remote Sensing, Halifax, Nova Scotia*, p. 187–194.
- Seshardi, S.R.** (1971) *Fundamentals of Transmission Lines and Electromagnetic Fields*. Reading, Massachusetts: Addison-Wesley Publishing Co.
- Stanley, W.D., G.R. Dougherty and R. Dougherty** (1984) *Digital Signal Processing*. Reston, Virginia: Reston Publishing Co.
- Stevens, H.W. and W.J. Tizzard** (1969) Traffic tests on Portage Lake ice. USA Cold Regions Research and Engineering Laboratory, Technical Report 99.
- Ulaby, F.T. and M.W. Whitt** (1988) Millimeter-wave polarimetric measurements of artificial and natural targets. *IEEE Transactions on Geoscience and Remote Sensing*, **26**(5): 562–573.
- Ulaby, F.T., R.K. Moore and A.K. Fung** (1981) *Microwave Remote Sensing—Active and Passive*, vol. 1–3. Reading, Massachusetts: Addison-Wesley Publishing Co.
- USA Cold Regions Research and Engineering Laboratory** (1986) *Field Guide: Fresh Water Ice Crossings*. USA Corps of Engineers.
- Valdmanis, J.A. and G. Mourou** (1986) Subpicosecond electro-optic sampling: Principles and applications. *IEEE Journal of Quantum Electronics*, **QE-22** (1): 69–78.
- Van Etten, P.** (1979) Impulse radars. In *Proceedings of the International Workshop on the Remote Estimation of Sea Ice Thickness, St. John's, Newfoundland, Canada*, p. 421–436.
- Venier, G.O. and F.R. Cross** (1975) An airborne linear-sweep FM radar system for measuring ice thickness. Ottawa: Communications Research Centre, Department of Communications—Canada, CRC Report 1269.
- Venier, G.O. F.R. Cross and R.O. Ramseier** (1975) Experiments with a mobile X-band FM radar in measuring the thickness of fresh-water ice. Ottawa: Department of Communications—Canada, Communications Research Centre, CRC Technical Note 673.
- Vickers, R.S.** (1975) Microwave properties of ice from the Great Lakes. Menlo Park, California: Stanford Research Institute, Contract NAS 3–19092, SRI Project 3571.
- Vickers, R.S. and G.C. Rose** (1972) High resolution measurements of snowpack stratigraphy using a short pulse radar. In *Proceedings of International Symposium on Remote Sensing of the Environment*. Ann Arbor: Environmental Institute of Michigan, p. 261–277.
- Vickers, R.W., J. Heighway and R. Gedney** (1974) Airborne profiling of ice thickness using a short pulse radar. Washington, D.C.: National Aeronautics and Space Administration, NASA, TM X–71481.
- Wehner, D.R.** (1987) *High Resolution Radar*. Norwood, Massachusetts: Artech House, Inc.
- Wills, R.** (1987) A digital phase coded ground-probing radar. Ph.D. Thesis, Thayer School of Engineering, Dartmouth College, Hanover, New Hampshire (unpublished).
- Wittmann, R.C. and R.E. Stoltenberg** (1981) Advanced FM/CW microwave techniques for remote sensing applications. Boulder, Colorado: Electromagnetic Fields Division, National Bureau of Standards, SR-732-20-81.
- Yamaguchi, Y., Y. Maruyama, A. Kawakami, M. Senogoku and T. Abe** (1991) Detection of objects buried in wet snowpack by a FM-CW radar. *IEEE Transactions on Geoscience and Remote Sensing*, **29**(2): 201–208.

APPENDIX A: SURVEY DETAILS

Skating arena profile with cart-mounted radar (survey study A)

Test location: Thompson Arena, Dartmouth College, Hanover, New Hampshire
 Test date: 2 November 1990
 Survey tape number: Not Applicable
 Radar range: 1.2 m
 Measurement speed: ≈ 3 km/hr
 Sweep rate: 0.25 s/sweep
 Power level: 10 dBm
 Bandwidth: 13.5 GHz (26.5 to 40 GHz)
 Ambient temperature: $\leq 0^\circ\text{C}$
 Ice temperature: $\leq 0^\circ\text{C}$
 Ice surface condition: Smooth with no discernible roughness

Stationary profiling of thin pond ice (survey study B)

Test parameters

Test location: Overflow pond at CRREL
 Test date: 26 December 1990
 Survey tape number: 2
 Radar range: 2 m
 Measurement speed: Stationary and swept arcs at < 1 m/s
 Sweep rate: 0.05 s/sweep
 Power level: 10 dBm
 Bandwidth: 13.5 GHz (26.5 to 40 GHz)
 Ambient temperature: -5°C
 Ice temperature: $\leq 0^\circ\text{C}$
 Ice surface condition: No snow cover, minimal surface roughness

Statistical analysis of data (Fig. A1–A5)

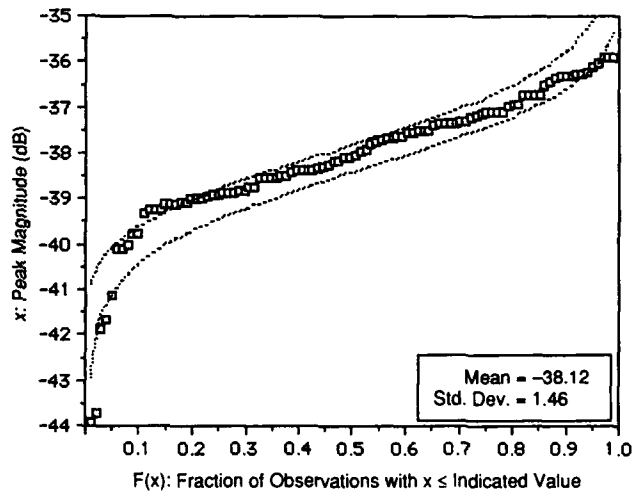
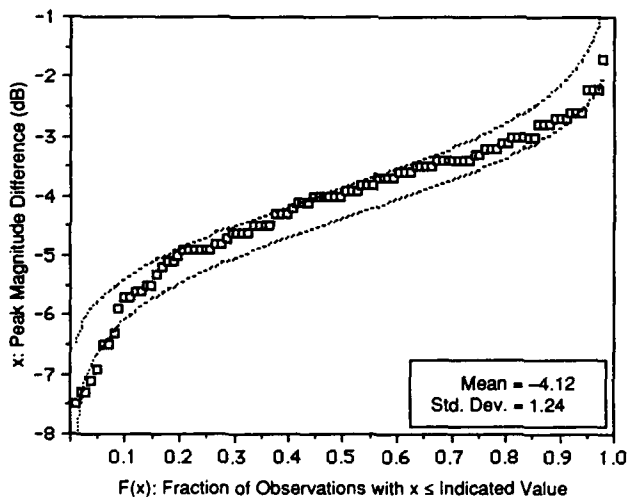


Figure A1. Peak magnitude difference between air/ice and ice/water interface CDF (95 and 5% confidence bounds shown for log-normal distribution).

Figure A2. Air/ice interface peak magnitude CDF (95 and 5% confidence bounds shown for log-normal distribution).

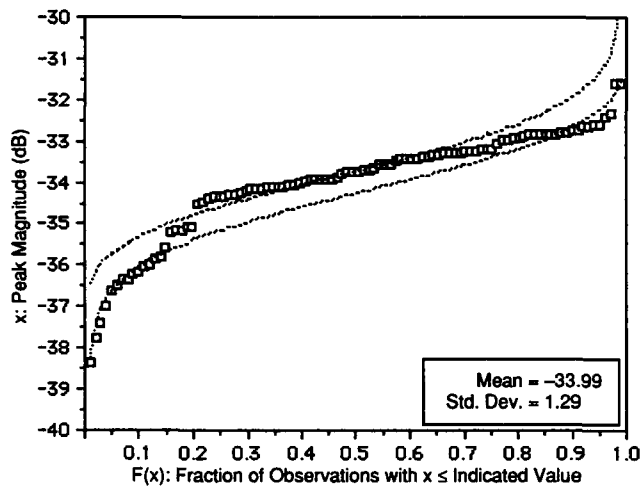


Figure A3. Ice/water interface peak magnitude CDF (95 and 5% confidence bounds shown for log-normal distribution).

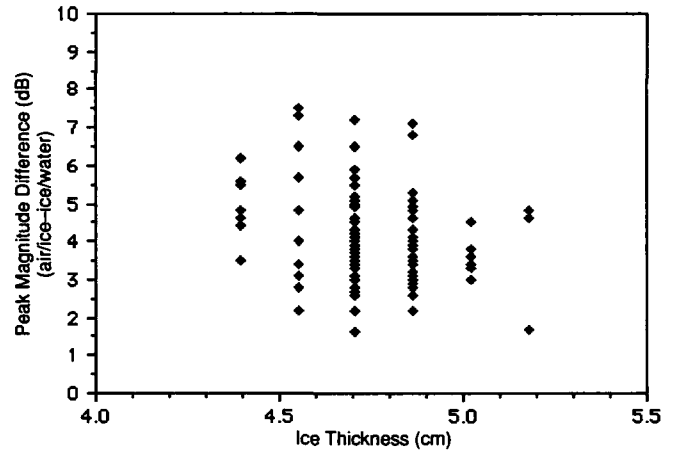


Figure A4. Peak magnitude difference between air/ice and ice/water interfaces vs ice thickness.

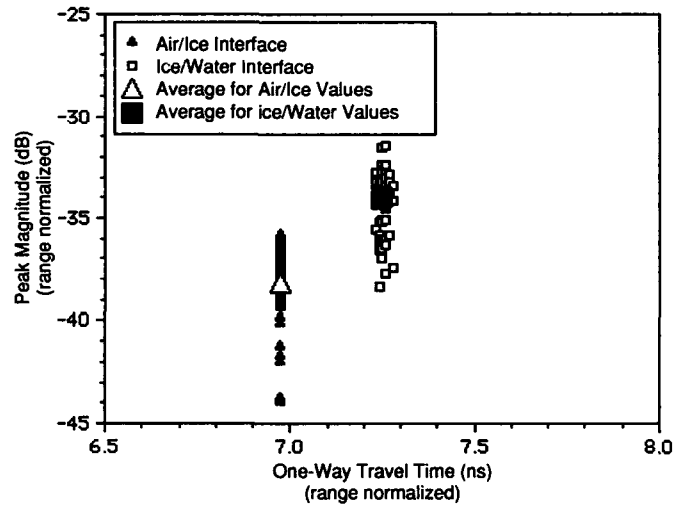


Figure A5. Peak magnitude vs one-way travel time range normalized to air/ice interface.

Cart-mounted profiling of overflow pond (survey study C)

Test parameters

Test location:	Overflow Pond at CRREL, Hanover, New Hampshire
Test date:	28 December 1990
Survey tape number:	6
Radar range:	≈ 1 m
Measurement speed:	≈ 3 km/hr
Sweep rate:	0.05 s/sweep
Power level:	10 dBm
Bandwidth:	13.5 GHz (26.5 to 40 GHz)
Ambient temperature:	-5°C
Ice temperature:	≤ 0°C
Ice surface condition:	Snow cover shoveled off of profile path, minimal surface roughness

Statistical analysis of data (Fig. A6-A10)

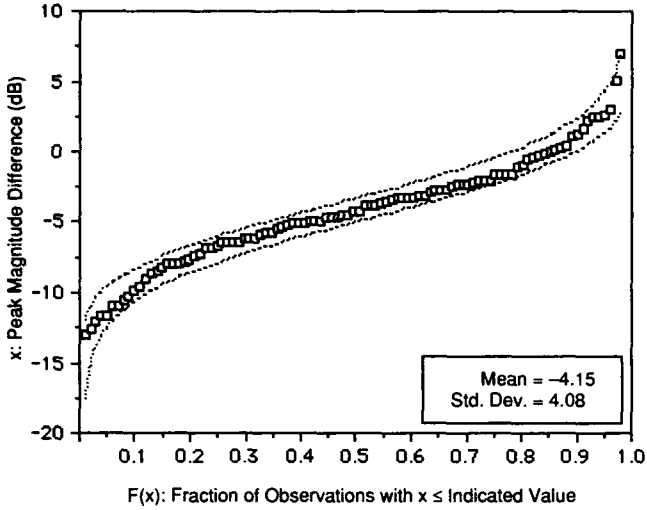


Figure A6. Peak magnitude difference between air/ice and ice/water interface CDF (95 and 5% confidence bounds shown for log-normal distribution).

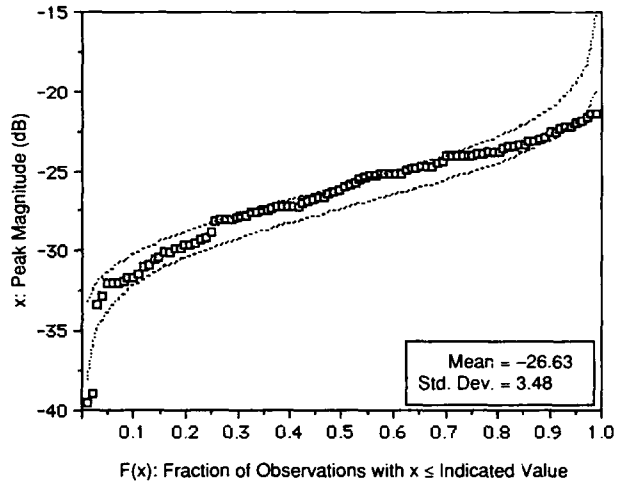


Figure A7. Air/ice interface peak magnitude CDF (95 and 5% confidence bounds shown for log-normal distribution).

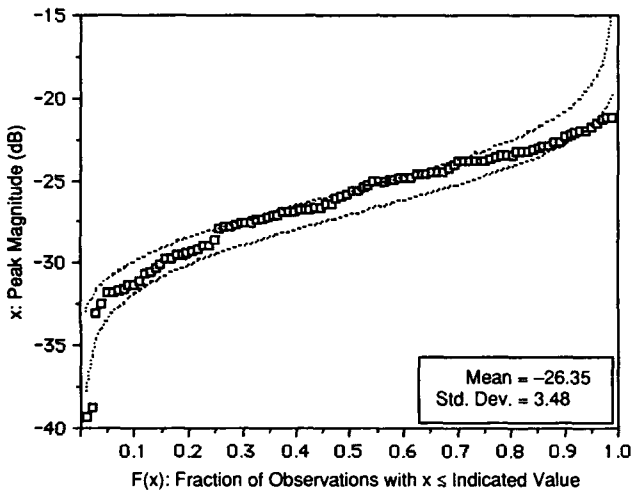


Figure A8. Ice/water interface peak magnitude CDF (95 and 5% confidence bounds shown for log-normal distribution).

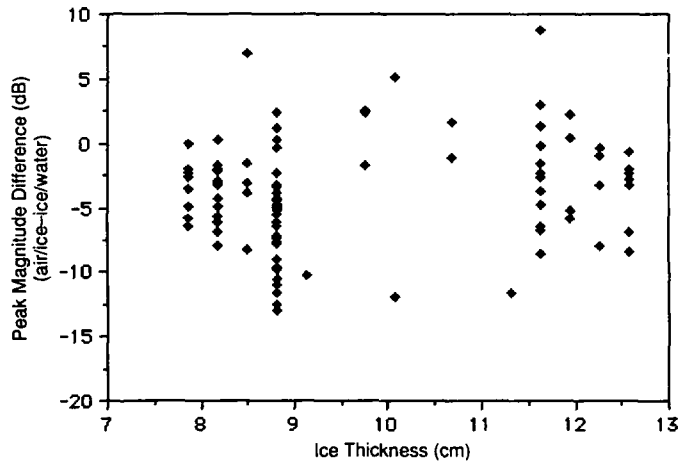


Figure A9. Peak magnitude difference between air/ice and ice/water interfaces vs ice thickness.

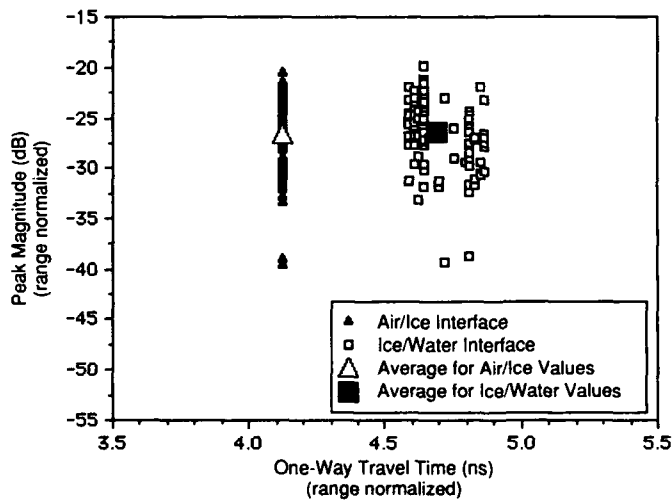


Figure A10. Peak magnitude vs one-way travel time range normalized to air/ice interface.

Cart-mounted profiling of ice on Post Pond (survey study D)

Test parameters

Test location: Post Pond, Lyme, New Hampshire
 Test date: 8 January 1991
 Survey tape number: 7
 Radar range: 1 m
 Measurement speed: ≈ 3 km/hr
 Sweep rate: 0.05 m
 Power level: 10 dBm
 Bandwidth: 13.5 GHz (26.5 to 40 GHz)
 Ambient temperature: -10°C
 Ice temperature: $\leq 0^{\circ}\text{C}$
 Ice surface condition: < 1 cm snow cover

Statistical analysis of data (Fig. A11–A15)

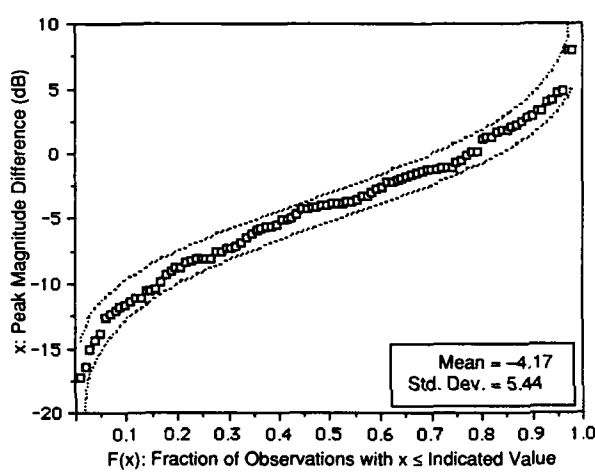


Figure A11. Peak magnitude difference between air/ice and ice/water interface CDF (95 and 5% confidence bounds shown for log-normal distribution).

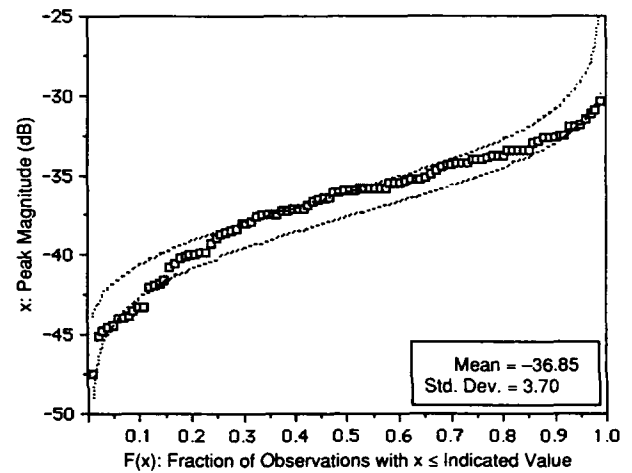


Figure A12. Air/ice interface peak magnitude CDF (95 and 5% confidence bounds shown for log-normal distribution).

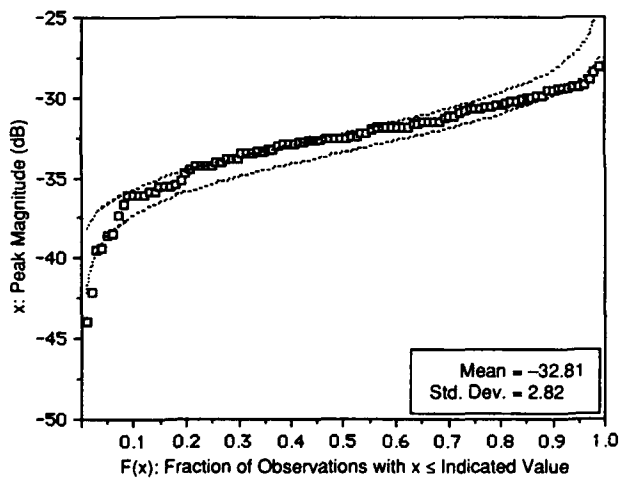


Figure A13. Ice/water interface peak magnitude CDF (95 and 5% confidence bounds shown for log-normal distribution).

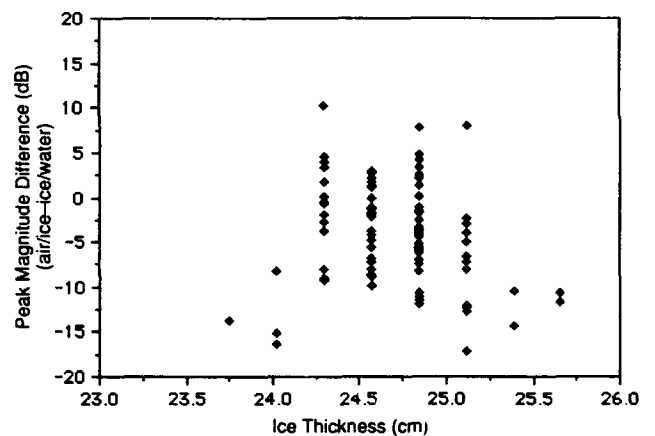


Figure A14. Peak magnitude difference between air/ice and ice/water interfaces vs ice thickness.

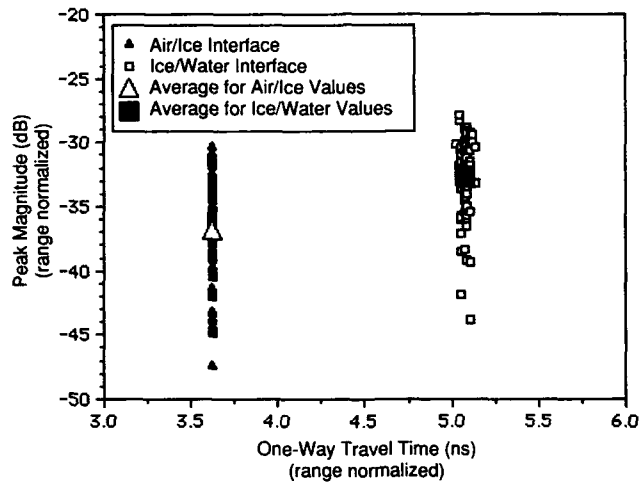


Figure A15. Peak magnitude vs one-way travel time range normalized to air/ice interface.

Truck-mounted profiling of snow-covered pond ice (survey study E)

Test parameters

- Test location: Post Pond, Lyme, New Hampshire
- Test date: 15 January 1991
- Survey tape number: 9
- Radar range: 1 m
- Measurement speed: 5 to 40 km/hr
- Sweep rate: 0.063 s/sweep
- Power level: 10 dBm
- Bandwidth: 13.5 GHz (26.5 to 40 GHz)
- Ambient temperature: -7°C
- Ice temperature: $\leq 0^{\circ}\text{C}$
- Ice surface condition: ≈ 18 cm snow cover over ≈ 30 cm ice with minimal surface roughness

Statistical analysis of data (Fig. A16–A22)

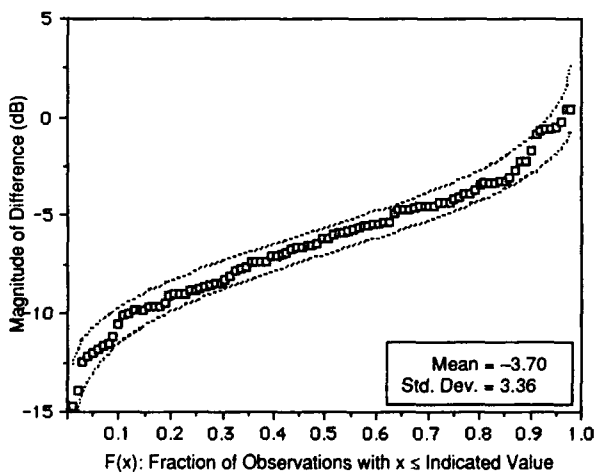


Figure A16. Peak magnitude difference between air/snow and snow/ice interface CDF (95 and 5% confidence bounds shown for log-normal distribution).

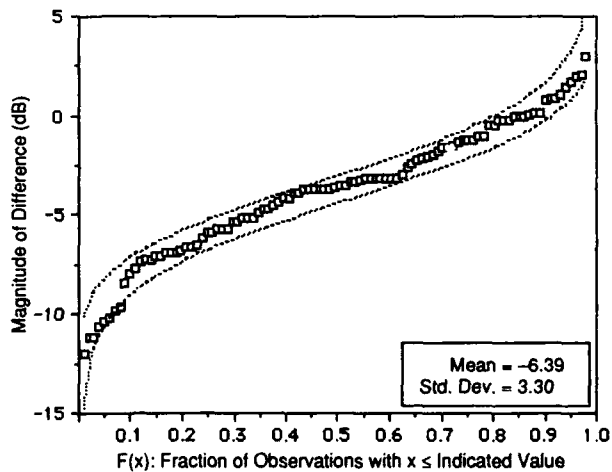


Figure A17. Peak magnitude difference between snow/ice and ice/water interface CDF (95 and 5% confidence bounds shown for log-normal distribution).

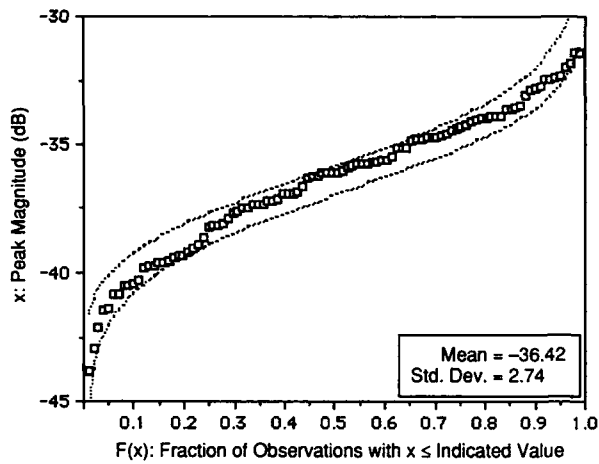


Figure A18. Air/snow interface peak magnitude CDF (95 and 5% confidence bounds shown for log-normal distribution).

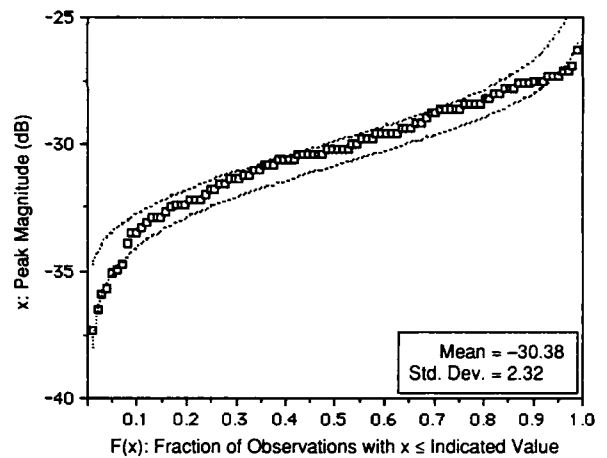


Figure A19. Snow/ice interface peak magnitude CDF (95 and 5% confidence bounds shown for log-normal distribution).

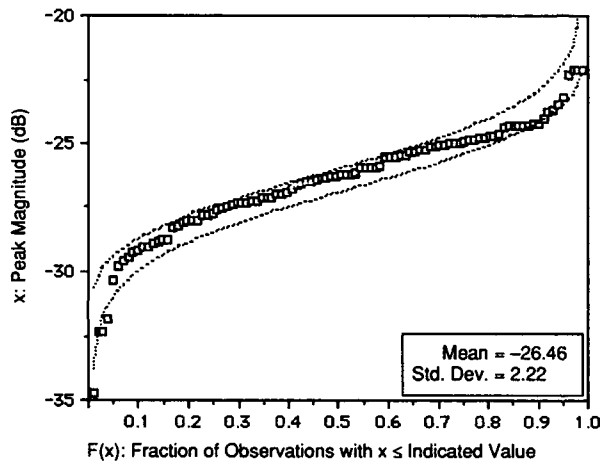


Figure A20. Ice/water interface peak magnitude CDF (95 and 5% confidence bounds shown for log-normal distribution).

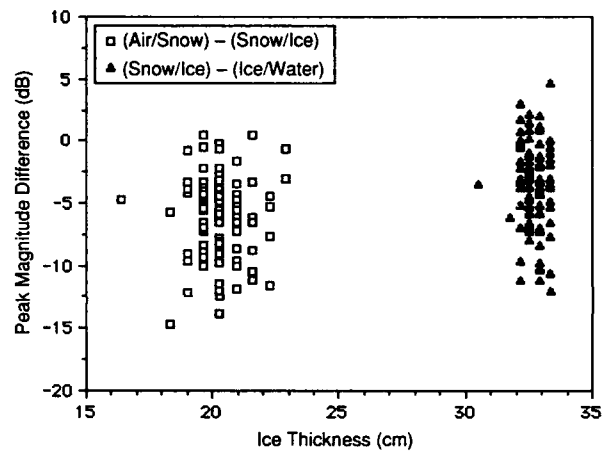


Figure A21. Peak magnitude difference between air/snow-snow/ice and snow/ice-ice/water interfaces vs ice thickness.

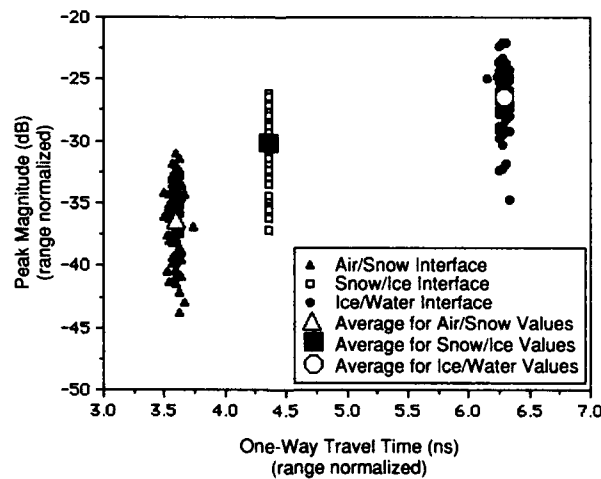


Figure A22. Peak magnitude vs one-way travel time range normalized to snow/ice interface.

Truck-mounted profiling of snow free pond ice (survey study F)

Test parameters

Test location: Post Pond, Lyme, New Hampshire
 Test date: 23 January 1991
 Survey tape number: 10
 Radar range: 2 m
 Measurement speed: 5 to 40 km/hr
 Sweep rate: 0.066 s/sweep
 Power level: 10 dBm
 Bandwidth: 13.5 GHz (26.5 to 40 GHz)
 Ambient temperature: -18°C
 Ice temperature: $\leq 0^{\circ}\text{C}$
 Ice surface condition: refrozen ice with varying snow cover ≤ 1 cm

Statistical analysis of data (Fig. A23–A31)

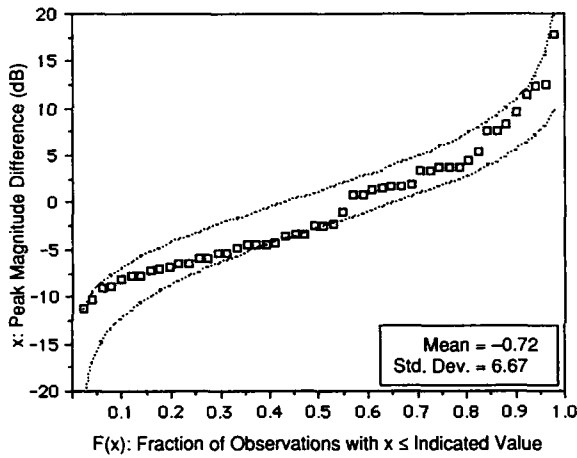


Figure A23. Peak magnitude difference between air/ice and ice/water interface CDF (95 and 5% confidence bounds shown for log-normal distribution).

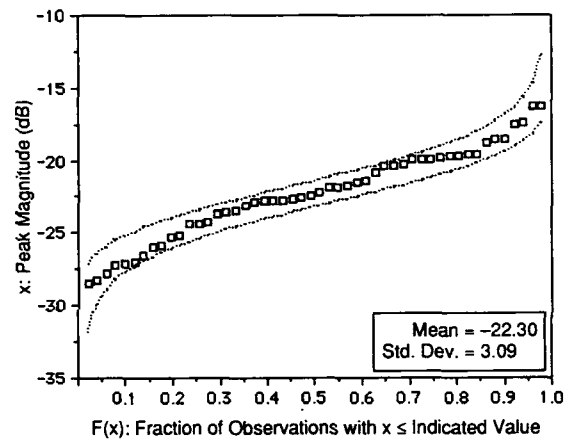


Figure A24. Air/ice interface peak magnitude CDF (95 and 5% confidence bounds shown for log-normal distribution).

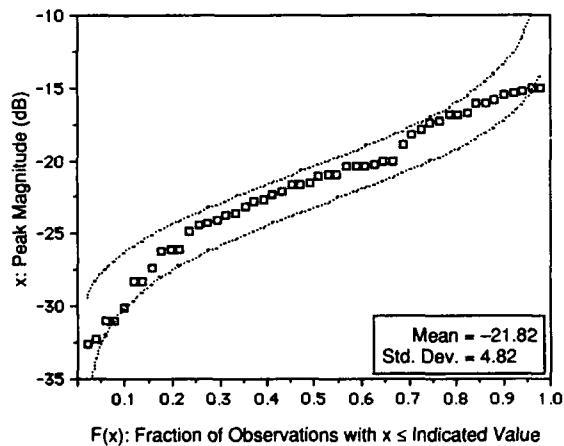


Figure A25. Ice/water interface peak magnitude CDF (95 and 5% confidence bounds shown for log-normal distribution).

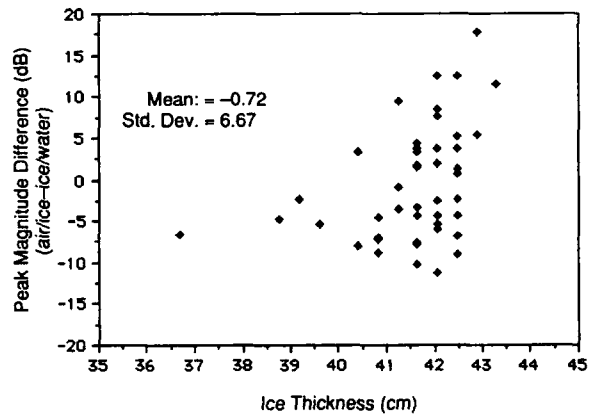


Figure A26. Peak magnitude difference between air/ice and ice/water interfaces vs ice thickness.

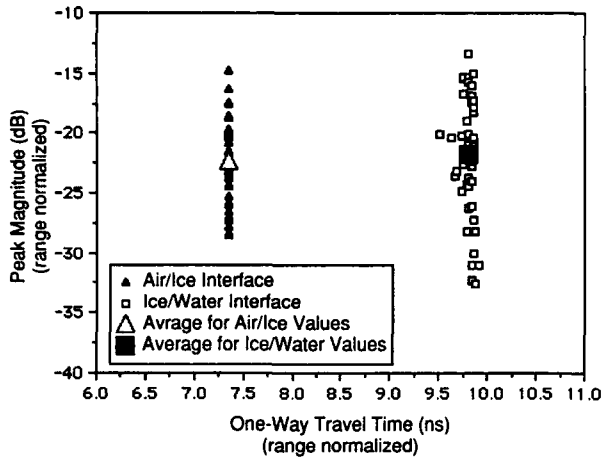


Figure A27. Peak magnitude vs one-way travel time range normalized to air/ice interface .

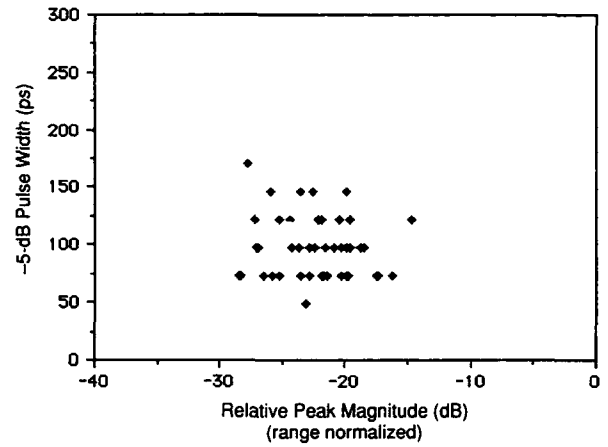


Figure A28. 5-dB pulse width vs peak magnitude for the air/ice interface.

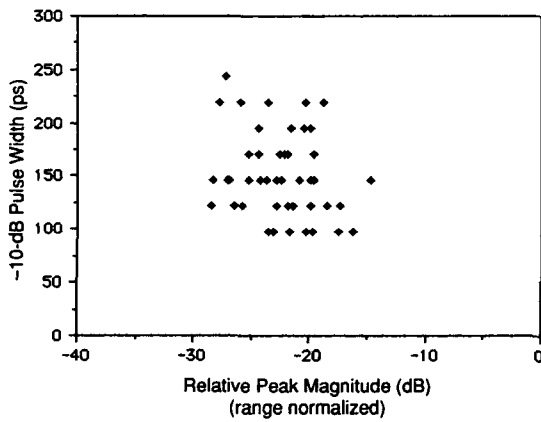


Figure A29. 10-dB pulse width vs peak magnitude for the air/ice interface.

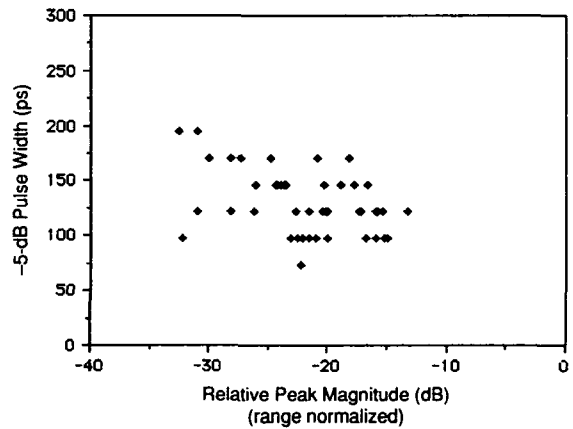


Figure A30. 5-dB pulse width vs peak magnitude for the ice/water interface.

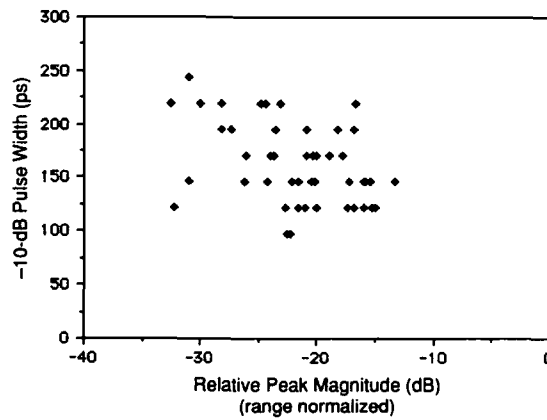


Figure A31. 10-dB pulse width vs peak magnitude for the ice/water interface.

Cart-Mounted profiling of Connecticut River ice (survey studies G and H)

Test parameters

Test location: Connecticut River at Ledyard Bridge, Hanover, New Hampshire
 Test date: 25 January 1991
 Survey tape number: 11a and 11b
 Radar range: 5 to 7 m
 Measurement speed: ≈ 3 km/hr
 Sweep rate: 0.133 s/sweep
 Power level: 15 dBm
 Bandwidth: 13.5 GHz (26.5 to 40 GHz)
 Ambient temperature: -12°C
 Ice temperature: $\leq 0^{\circ}\text{C}$
 Ice surface condition: < 1 cm snow cover, ≤ 1 cm roughness at center-span region of bridge

Statistical analysis of data (Fig. A32-A41)

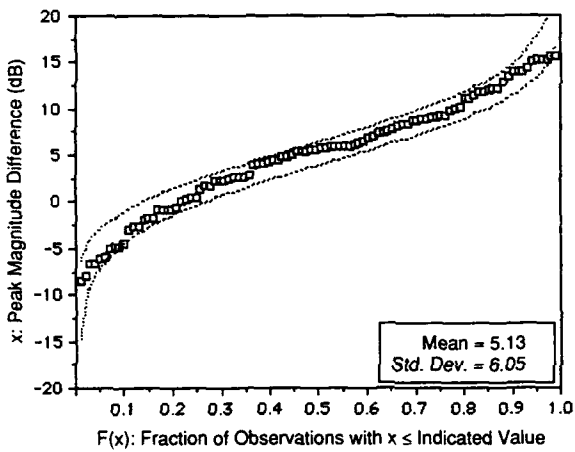


Figure A32. Peak magnitude difference between air/ice and ice/water interface CDF from survey study G (95 and 5% confidence bounds shown for log-normal distribution).

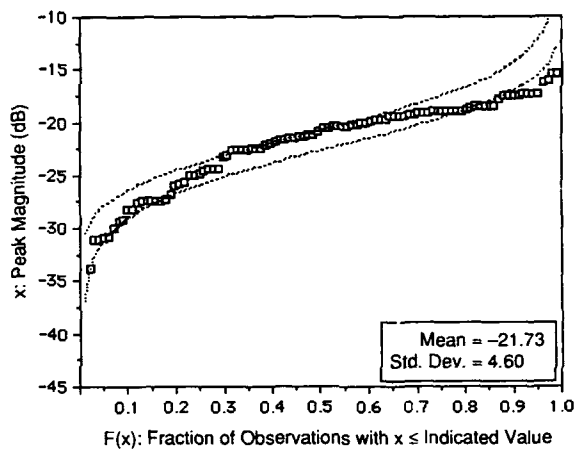


Figure A33. Air/ice interface peak magnitude CDF from survey study G (95 and 5% confidence bounds shown for log-normal distribution).

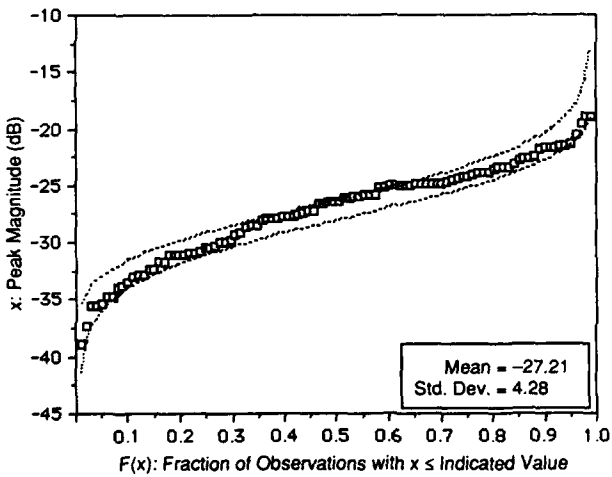


Figure A34. Ice/water interface peak magnitude CDF from survey study G (95 and 5% confidence bounds shown for log-normal distribution).

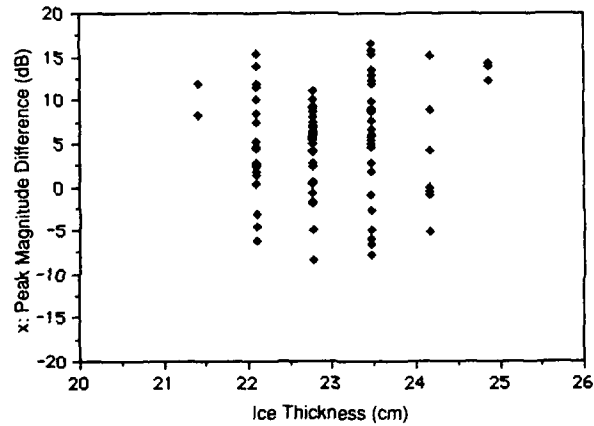


Figure A35. Peak magnitude difference between air/ice and ice/water interfaces vs ice thickness from survey study G.

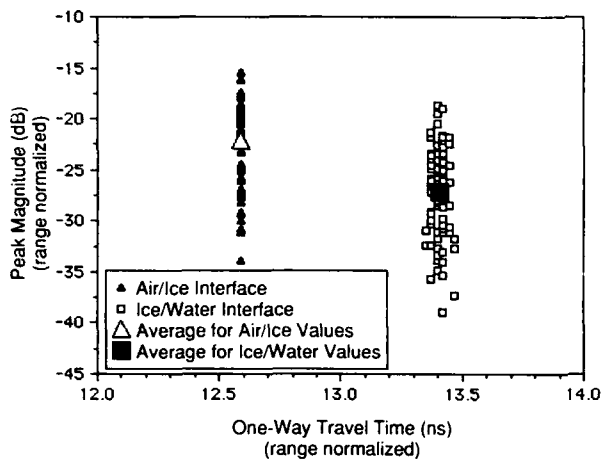


Figure A36. Peak magnitude vs one-way travel time from survey study G range normalized to air/ice interface.

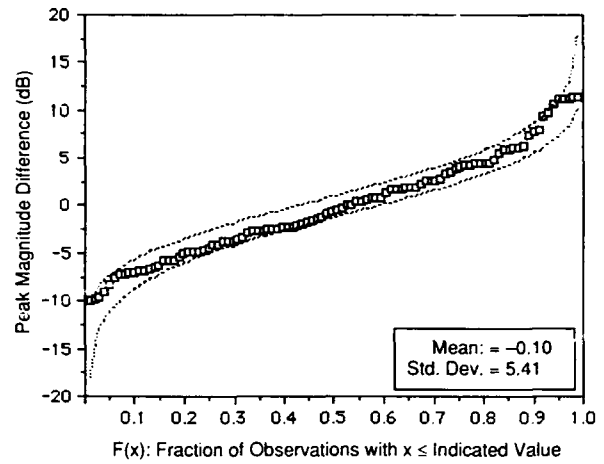


Figure A37. Peak magnitude difference between air/ice and ice/water interface CDF from survey study H (95 and 5% confidence bounds shown for log-normal distribution).

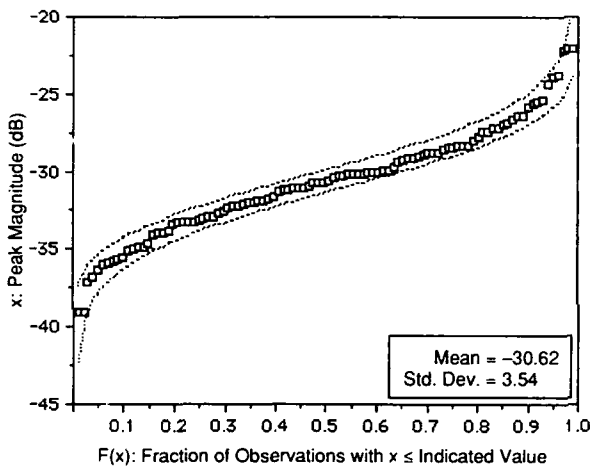


Figure A38. Air/ice interface peak magnitude CDF from survey study H (95 and 5% confidence bounds shown for log-normal distribution).

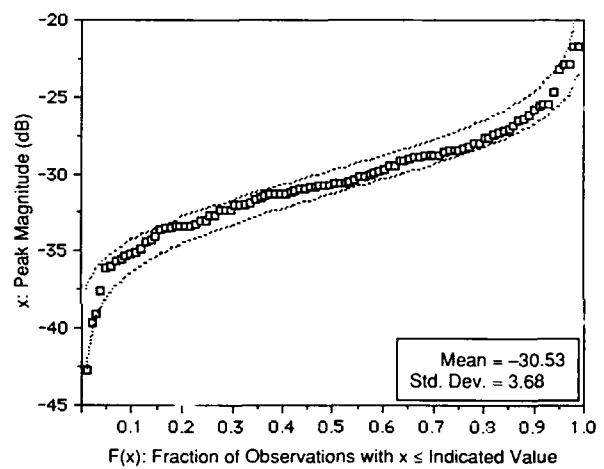


Figure A39. Ice/water interface peak magnitude CDF from survey study H (95 and 5% confidence bounds shown for log-normal distribution).

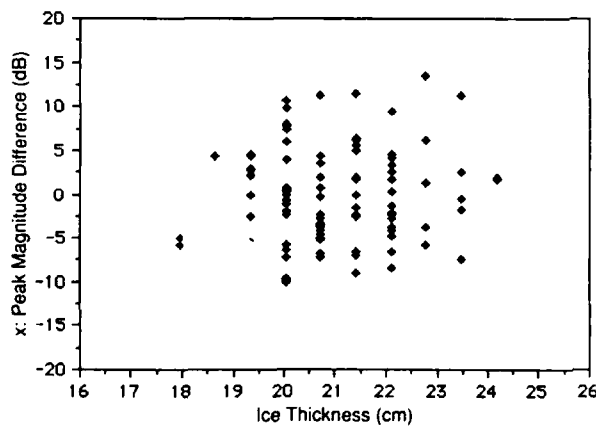


Figure A40. Peak magnitude difference between air/ice and ice/water interfaces vs ice thickness from survey study H.

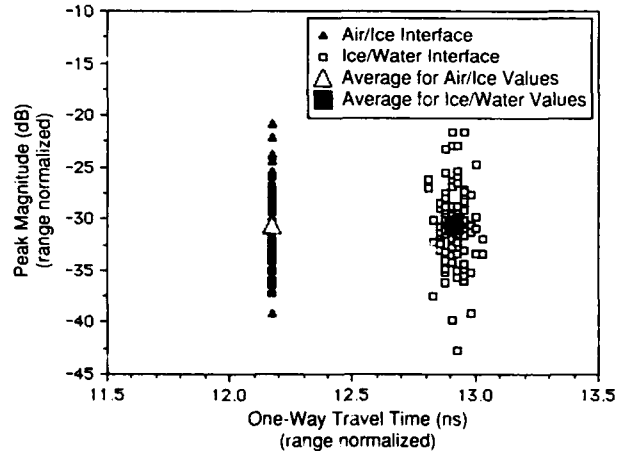


Figure A41. Peak magnitude vs one-way travel time from survey study H range normalized to air/ice interface.

Airborne profiling of lake ice (survey study I)

Test parameters

Test location: Turtle Pond, near Concord, New Hampshire
 Test date: 26 February 1991
 Survey tape number: 13
 Radar range: 2 to 7 m
 Measurement speed: 5 to 40 km/hr
 Sweep rate: 0.133 s/sweep
 Power level: 13 to 15 dBm
 Bandwidth: 13.5 GHz (26.5 to 40 GHz)
 Ambient temperature: $< 5^{\circ}\text{C}$
 Ice temperature: $\approx 0^{\circ}\text{C}$
 Ice surface condition: ≤ 1 cm snowcover, minimal surface roughness

Statistical analysis of data (Fig. A42-A46)

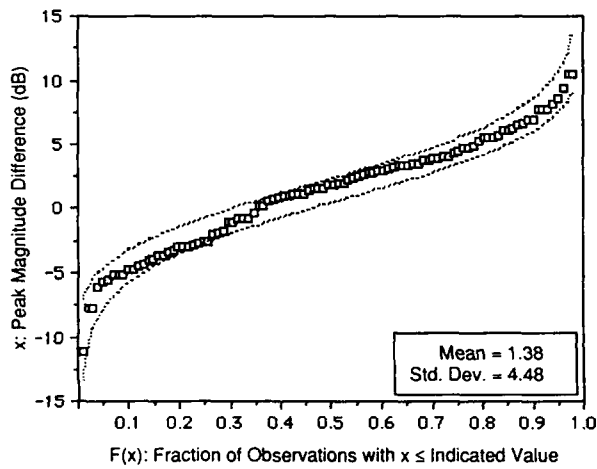


Figure A42. Peak magnitude difference between air/ice and ice/water interface CDF (95 and 5% confidence bounds shown for log-normal distribution).

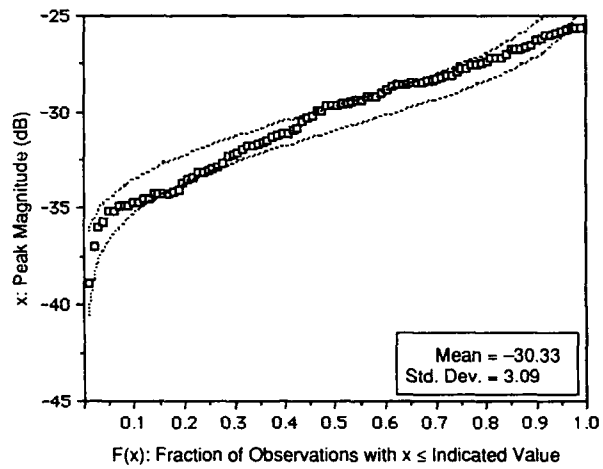


Figure A43. Air/ice interface peak magnitude CDF (95 and 5% confidence bounds shown for log-normal distribution).

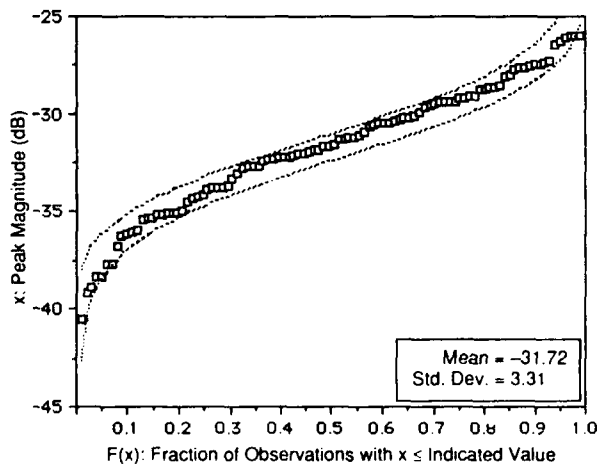


Figure A44. Ice/water interface peak magnitude CDF (95 and 5% confidence bounds shown for log-normal distribution).

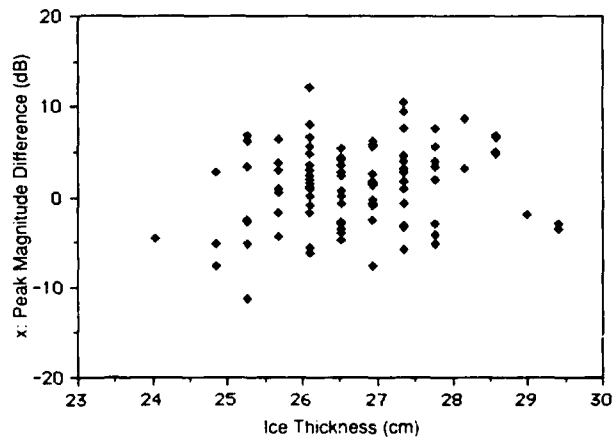


Figure A45. Peak magnitude difference between air/ice and ice/water interfaces vs ice thickness.

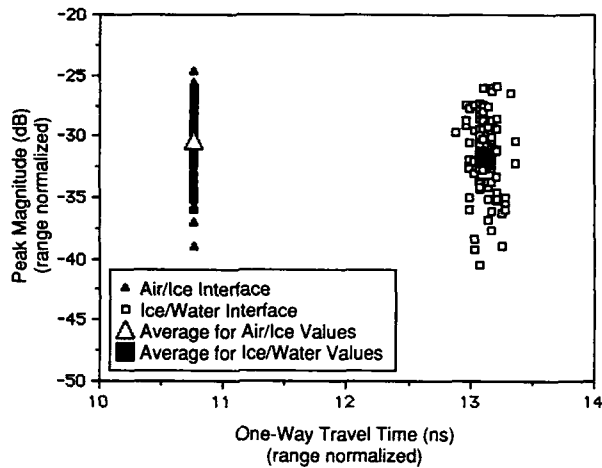


Figure A46. Peak magnitude vs one-way travel time range normalized to air/ice interface.

Airborne profiling of river ice (survey study J)

Test parameters

Test location: Pemigewasset River, near Franklin, New Hampshire
 Test date: 26 February 1991
 Survey tape number: 14
 Radar range: 2 to 7 m
 Measurement speed: 5 to 40 km/hr
 Sweep rate: 0.133 s/sweep
 Power level: 13 to 15 dBm
 Bandwidth: 13.5 GHz (26.5 to 40 GHz)
 Ambient temperature: < 5°C
 Ice temperature: ≈ 0°C
 Ice surface condition: < 1 cm snow cover, patches of meltwater minimal surface roughness

Statistical analysis of data (Fig. A47–A52)

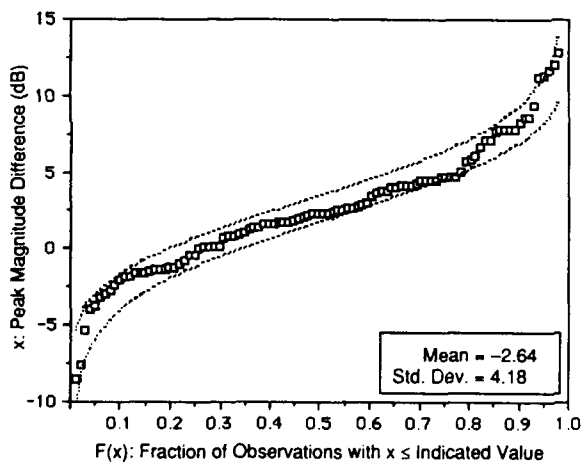


Figure A47. Peak magnitude difference between air/ice and ice/water interface CDF (95 and 5% confidence bounds shown for log-normal distribution).

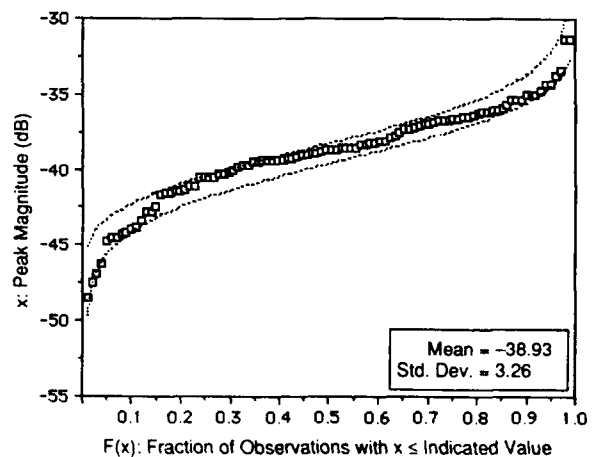


Figure A48. Air/ice interface peak magnitude CDF (95 and 5% confidence bounds shown for log-normal distribution).

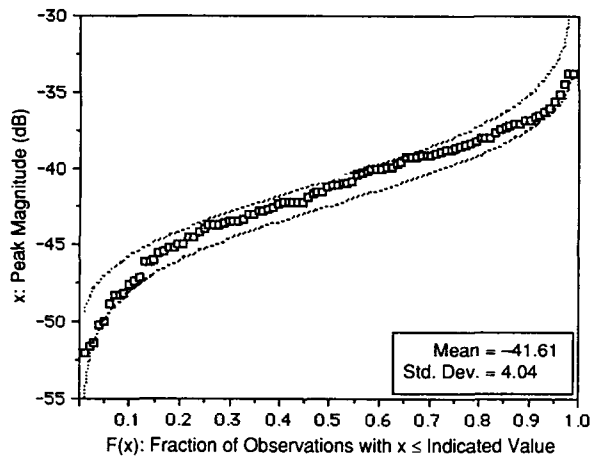


Figure A49. Ice/water interface peak magnitude CDF (95 and 5% confidence bounds shown for log-normal distribution).

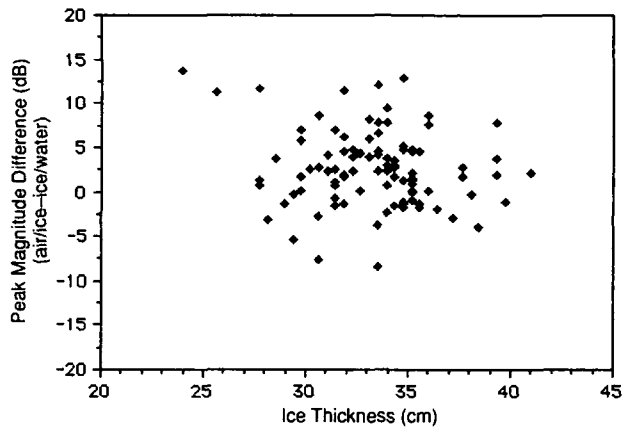


Figure A50. Peak magnitude difference between air/ice and ice/water interfaces vs ice thickness.

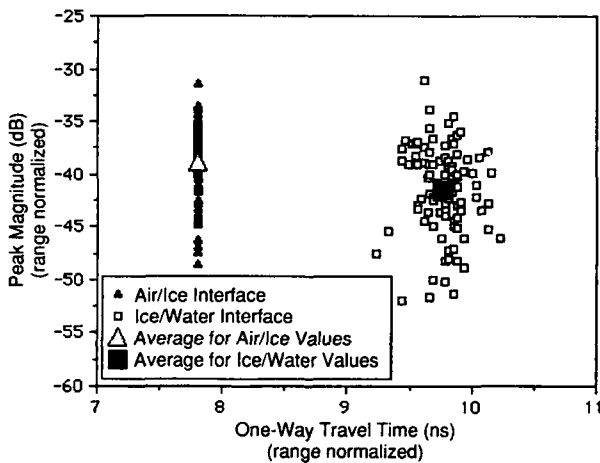


Figure A51. Peak magnitude vs one-way travel time range normalized to air/ice interface

FM-CW radar system implementation

An Army Research Office (ARO) grant enabled the implementation of a practical, field-hardened MMW FM-CW radar profiling system, incorporating the specifications and performance criteria formulated during the development of the prototype system. The radar data acquisition and DSP computer system (Fig. A52) is fully housed in a 55- × 60- × 75-cm water-resistant and shockproof case weighing less than 25 kg and powered by a 24-V, 25-A-hr battery providing greater than 2 hours of remote field or airborne operation. The system can alternatively be operated from the aircraft dc power supply.

The homodyne front end of the radar is housed in a separate waterproof aluminum enclosure containing the waveguide directional couplers and other waveguide components—HP R422C diode detector, AvanteK, Inc., AVD-24140, 13 dBm, 26.5- to 40-GHz YTO, and Analog Modules, Inc., Model 351 low-noise voltage amplifier. Mica waveguide windows between the antenna waveguide flanges and the through-bulkhead flanges on the front-end enclosure provide a waveguide port environmental seal. The front-end assembly can be mounted on a helicopter landing skid for airborne profiling. Two coaxial signal cables (for the YIG sweep ramp and radar signal out) interconnect the front end and the computer system. Operating power (± 15 Vdc) is provided via a third cable from a dc-dc converter connected to the 24-Vdc battery.

All data acquisition, monitoring, display, digital storage and radar control are performed by seven off-the-shelf dedicated-function computer cards installed in the Industrial Computer Source, Inc., 15-slot 33-MHz

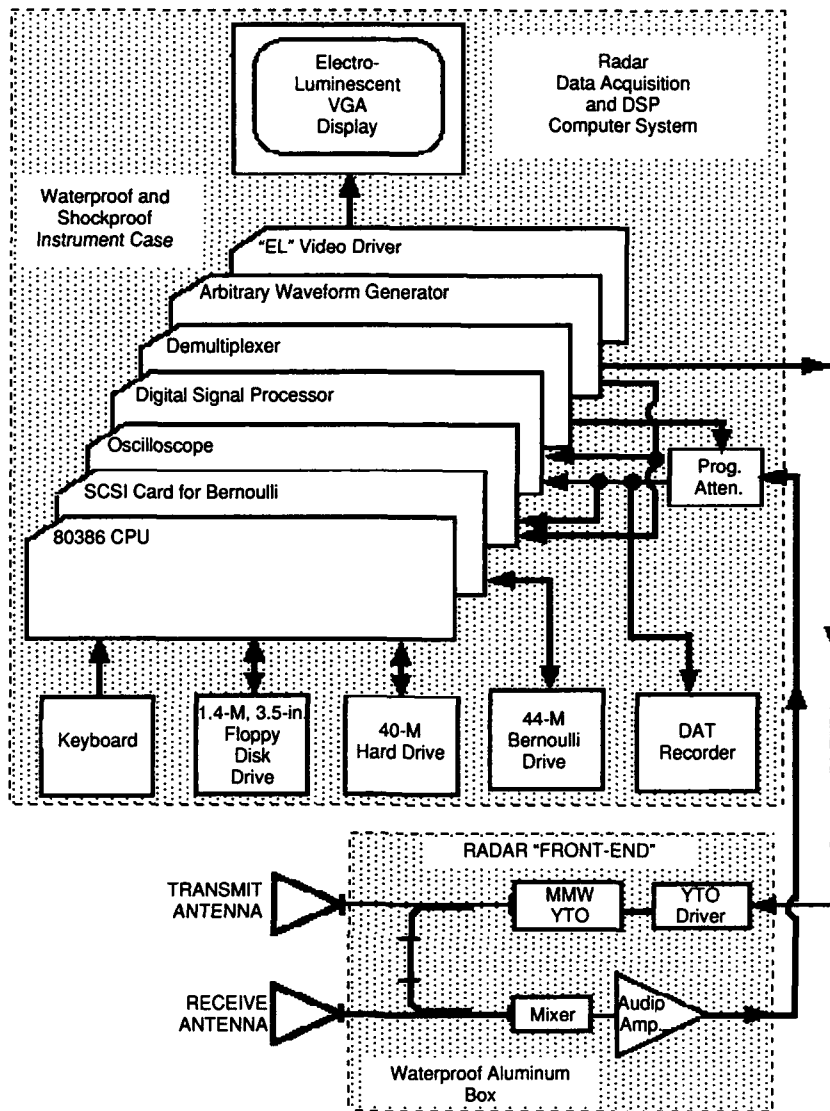


Figure A52. FM-CW radar system implementation.

80386 DOS-based computer. Also included are an 80387 math coprocessor, a conventional 40-megabyte hard-drive and 4 megabytes of RAM. The remaining slots are available for system expansion. All system control functions are done directly via computer keyboard input.

The SCSI card and interconnected Iomega, Inc., Bernoulli removable platter 44-megabyte drive are for in-flight, non-volatile storage of digital data, since the drive and media are less susceptible to failure in high vibration or high *g*-force environments. In practice, once "booted" via the conventional internal 40 megabyte hard drive, this drive is shut down with heads parked. Any subsequent acquired digital data are stored on the Bernoulli drive.

The Metrabyte, Inc., 20-MHz, 12-bit, dual-channel digital oscilloscope card (PCIP-SCOPE) permits real-time monitoring of various system signals on the computer display without affecting other in-progress data acquisition or processing functions. The oscilloscope display is in a "pop-up" window format that can be viewed or hidden by a "CONTROL + character" keystroke.

The Spectrum, Inc., DSP card performs dual-channel, 16-bit data acquisition to a maximum rate of 200 kHz and digital signal processing functions using the Hyperception, Inc., Hypersignal Workstation DSP software as a driver.

The Metrabyte, Inc., scanner (demultiplexer) board (PCIP-SCAN) is configured to provide keyboard control

of the 0- to 100-dB JFW, Inc., programmable attenuator located between the front-end audio amplifier output and the DSP board data acquisition input. Access to the control and status display of the demultiplexer is functionally consistent with the "pop-up" display for the oscilloscope.

The Metrabyte, Inc., dual channel arbitrary waveform generator (PCIP-AWFG) is programmed to provide the linear ramp 0- to 10-V sweep signal to frequency modulate the MMW YIG oscillator and a TTL-level synchronization and trigger signal signal. Access to the control and status display for the arbitrary waveform generator is functionally consistent with the "pop-up" display for the oscilloscope and the demultiplexer.

The "EL" video driver card provides an interface between the computer system and a VGA-compatible electro-luminescent orange-on-black video display. This is a lightweight, low-power, high-contrast, vibration-immune display well suited for a field operations environment.

Additionally, raw data can be acquired by a TEAC, Inc., RD-104 four-channel DAT recorder for later playback and post-processing.

REPORT DOCUMENTATION PAGE

Form Approved
OMB No. 0704-0188

Public reporting burden for this collection of information is estimated to average 1 hour per response, including the time for reviewing instructions, searching existing data sources, gathering and maintaining the data needed, and completing and reviewing the collection of information. Send comments regarding this burden estimate or any other aspect of this collection of information, including suggestion for reducing this burden, to Washington Headquarters Services, Directorate for Information Operations and Reports, 1215 Jefferson Davis Highway, Suite 1204, Arlington, VA 22202-4302, and to the Office of Management and Budget, Paperwork Reduction Project (0704-0188), Washington, DC 20503.

1. AGENCY USE ONLY (Leave blank)		2. REPORT DATE November 1992		3. REPORT TYPE AND DATES COVERED	
4. TITLE AND SUBTITLE An Airborne Millimeter-Wave FM-CW Radar for Thickness Profiling of Freshwater Ice				5. FUNDING NUMBERS DAAL 03-91-G-0192	
6. AUTHORS Norbert E. Yankielun					
7. PERFORMING ORGANIZATION NAME(S) AND ADDRESS(ES) Thayer School of Engineering Dartmouth College Hanover, New Hampshire 03755				8. PERFORMING ORGANIZATION REPORT NUMBER	
9. SPONSORING/MONITORING AGENCY NAME(S) AND ADDRESS(ES) U.S. Army Cold Regions Research and Engineering Laboratory 72 Lyme Road Hanover, New Hampshire 03755-1290				10. SPONSORING/MONITORING AGENCY REPORT NUMBER CRREL Report 92-20	
11. SUPPLEMENTARY NOTES The Army Research Office, P.O. Box 12211, Research Triangle Park, North Carolina 27709-2211, funded the construction of a practical, field-hardened MMW FM-CW radar profiling system.					
12a. DISTRIBUTION/AVAILABILITY STATEMENT Approved for public release; distribution is unlimited. Available from NTIS, Springfield, Virginia 22161.				12b. DISTRIBUTION CODE UL	
13. ABSTRACT (Maximum 200 words) The ability to profile rapidly and accurately the structure of freshwater ice down to a thickness of a few centimeters over large surfaces of frozen ponds, lakes and rivers has wide military, industrial, commercial and recreational application, including safety and trafficability surveys. A prototype broadband millimeter wave (26.5 to 40 GHz) Frequency Modulated-Continuous Wave (FM-CW) radar, employing real-time data acquisition and Digital Signal Processing (DSP) techniques, has been developed for continuously recording the thickness profile of freshwater ice. Thickness resolution is better than 3 cm \pm 10%, which improves on short-pulse and FM-CW radars operating at frequencies less than 10 GHz. These other radars have a best reported thickness resolution of approximately 10 cm with a \pm 10% accuracy; this is insufficient because a freshwater ice sheet as thin as 5 cm, floating on water, can be safely traversed by an individual of average weight. System specifications include a 15-dBm output RF (Radio Frequency) power level, a 0.066-second sweep rate and less than a 50-dB Signal-to-Noise Ratio (SNR). This radar was tested on the ground and from a helicopter at heights of up to 7 m above ice surfaces at speeds up to 40 km/hr. Pond and river ice sheets between 3 and 35 cm thick, with and without fresh snow cover, and with minimal surface roughness have been profiled. Results have shown direct correlation between radar and borehole thickness measurements. Losses from volume scattering by imbedded air bubbles did not significantly affect the system's capability to discern the air/ice and ice/water scattering boundaries.					
14. SUBJECT TERMS Field tests Ice				15. NUMBER OF PAGES 88	
Ice safety Ice thickness profiling				16. PRICE CODE	
Millimeter wave radar					
17. SECURITY CLASSIFICATION OF REPORT UNCLASSIFIED		18. SECURITY CLASSIFICATION OF THIS PAGE UNCLASSIFIED		19. SECURITY CLASSIFICATION OF ABSTRACT UNCLASSIFIED	
				20. LIMITATION OF ABSTRACT UL	